SPECTROSCOPIC STUDY OF OPTICAL CONFINEMENT AND TRANSPORT
EFFECTS IN COUPLED MICROSPHERES AND PILLAR CAVITIES

by

Seungmoo Yang

A dissertation submitted to the faculty of
The University of North Carolina at Charlotte
In partial fulfillment of the requirements
for the degree of Doctor of Philosophy in
Optical Science and Engineering

Charlotte

2009

Approved by:

_____
Dr. Vasily N. Astratov

_____
Dr. Nathaniel M. Fried

_____
Dr. Mingxin Xu

_____
Dr. Ana Jofre

_____
Dr. Donald Jacobs

ABSTRACT

SEUNGMOO YANG. Spectroscopic study of optical confinement and transport effects in coupled microspheres and pillar cavities. (Under the direction of Dr. VASILY N. ASTRATOV)

In this thesis we investigated the spatial and spectral mode profiles, and the optical transport properties of single and multiple coupled cavities. We performed numerical modeling of whispering gallery modes (WGMs) in such cavities in order to explain recent experiments on semiconductor micropillars. High quality (Q up to 20 000) WGMs with small mode volumes V ~0.3 μm^3 in 4-5 μm micropillars were reproduced. The WGM spectra were found to be in a good agreement with the experimental data.

The coupling between size-matched spheres from 2.9 to 6.0 μm in diameter was characterized using spectroscopy. We observed peculiar kites in the spectral images of such coherently coupled bispheres. The origin of these kites was explained due to the coupling of multiple pairs of azimuthal modes. We quantified the coupling constant for WGMs located in the equatorial plane of spheres parallel to the substrate which plays the most important role in the transport of WGMs in such structures.

It was shown that in long (>10 spheres) chains of size-disordered polystyrene microspheres the transmission properties are dominated by photonic nanojet-induced modes (NIMs) leading to periodic focusing of light along the chain. In the transmission spectra of such chains we observed Fabry-Pérot fringes with propagation losses of only 0.08 dB per sphere at the maxima of the transmission peaks. The fringes of NIMs are found to be in a good agreement with the results of numerical modeling. These modes can be used in various biomedical applications requiring tight focusing of the beams.

ACKNOWLEDGMENTS

First of all I would like to thank my advisor Professor Dr. Vasily N. Astratov, for his advice and support during my dissertation at University of North Carolina at Charlotte. He taught me many valuable lessons on how to perform research in the field of spectroscopic experiments. He helped me to identify and interpret complex results. I would like to thank him for his efforts to focus and envision the research domain. It has been a good time for me to experience his research areas during my study at UNC Charlotte. I would like to thank him for his help in preparing for my presentations. His suggestions and comments during the course of my graduate education at UNC-Charlotte have made it possible for me to achieve this higher education. I have enjoyed the discussions that we have had during my study at UNC-Charlotte.

I came to UNC-Charlotte after several years spent as a graduate student at the University of Minnesota, University of Alabama at Huntsville, and Brigham Young University. While I was struggling with my PhD study at Brigham Young University, Dr. Vasily N. Astratov helped me come to UNC-Charlotte. I was attracted by active research and teaching optical programs established at the Department of Physics and Optical Sciences, the whole environment of this dynamic campus, and the beautiful city of Charlotte. I would like to thank him for his help and giving me a chance of studying his research area.

I am grateful to my thesis committee members, Professors Nathaniel Fried, Ana Jofre, Mingxin Xu, Donald Jacobs for their time and advice. I would like to thank our department chairmen Professor Dr. Faramarz Farahi for comments and discussions. Especially I really appreciate his financial support for two semesters as a TA at UNC

v

Charlotte, which has been a very precious extra experience during my study. I would like to thank the Optoelectronics Center and its Director, Professor Dr. Michael A. Fiddy, for many helpful materials for optics in his class.

I would like to thank Dr. Andrey Kapitonov and Dr. Shashanka Ashili for their help and expert suggestions in overcoming experimental hurdles, which have been essential to this work. I also thank Dr. Kiran Hiremath for many discussions in our meetings.

In addition, I am extremely appreciative of a financial support for my Graduate Assistantship position obtained from Army Research Office (W911NF-05-1-0529) and National Science Foundation (ECCS-0824067).

My experience as a graduate student at UNC Charlotte was well rounded. I would like to thank the staffs of Physics department and Optics center, Dr. Lou Deguzman, Dr. Robert Hudgins, Dr. Oleg Smolski, Bruce W. Dudley, Alec Martin, and Scott Williams for helping me in learning and using the equipment in the clean room. I would like to thank system administrator Evan Rowell for helping me with the PC's in the lap. I also thank Elizabeth Butler for helping me to sort out all the administrative issues during my study at UNC-Charlotte. I would like to thank teaching resource coordinator, Alexis Seven, for helping me in performing TA responsibilities.

Special thanks go to microscopy sales representative Lauren Robertson for helping me with learning and updating the Olympus microscope, which has been one of the main pieces of equipment for my experiments at UNC Charlotte.

I would like to thank many graduate students in UNCC whom I have talked with. They have been my best friends during my PhD study at UNCC.

Finally, I would like to thank my loving wife, Yunjung Kang, and my two sons, Sonmo and Gyoungmo. I could not have finished my studies without her help and support in many ways. I also would like to thank my parents and parents-in-law who have supported me for long time with their spoken and silent prayers.

TABLE OF CONTENTS

LIST OF TABLES

LIST OF FIGURES

LIST OF ABBREVIATIONS

2D	two dimension(al)
3D	three dimension(al)
AB	antibonding
AOE	advanced oxide etch
B	bonding
CCD	charge-coupled device
CQED	cavity quantum electrodynamics
CROW	coupled resonator optical waveguide
CW	continuous wave
EBL	electron-beam lithography
ECR	electron cyclotron resonance
EM	electromagnetic
FDTD	finite difference time domain
FL	florescent
FSR	free spectral range
FWHM	full width at half maximum
IPA	isopropyl alcohol
LED	light emitting diode
MRC	microsphere resonator circuit
NIM	nanojet-induced mode
NMS	normal mode splitting
PL	photoluminescence

PMMA   poly(methyl methacrylate)

QD   quantum dot

SEM   scanning electron microscopy

TE   transverse electric

TIR   total internal reflection

TM   transverse magnetic

WGM   whispering gallery mode

WGR   whispering gallery resonator

CHAPTER 1: INTRODUCTION

1.1 Outline and overview of thesis

This thesis is devoted to experimental studies and numerical modeling of optical properties of microcavities such as dielectric microspheres and semiconductor micropillars. The research in this thesis falls into two directions.

The first direction is devoted to *resonant* properties of the microcavities. In general, confinement of light in cavities takes place in a variety of structures such as photonic crystals with local defects [1-8], planar semiconductor microcavities [9, 10], micropillars [11-22], microdisks [23-31], rings [32-39], toroids [40-42], and microspheres [43-67]. Since the first microsphere laser [68] was developed much work on WGMs in individual spheres has been done by many groups [43-67]. The confinement of light occurs due to various effects including Bragg reflection [1-22] and total internal reflection (TIR) [23-68].

In this thesis we will focus mainly on microspheres and microdisks where the light waves can be trapped due to total internal reflection, leading to the formation of so-called whispering gallery modes (WGMs). These resonant optical modes in these microcavities show very interesting properties due to high quality factor and small mode volume V. WGMs in microspheres can have Q-factors in excess of 10^9 [45-49]. Such Q-factors are available in relatively large spheres with submicron dimensions where the modal volumes are around 5×10^3 μm^3 [49-51]. A combination of large Q and small

modal volumes increases light-matter interaction in such cavities. For example nanoparticles deposited at the surfaces of such cavities or embedded inside the cavities can be sensitively detected due to their interaction with WGMs [69]. Such structures can also be used in cavity quantum electrodynamics (CQED) experiments [4-6, 11, 13, 31, 42, 62]. An example of such experiments is generation of single photons which can be strongly coupled to photonic modes in such structures [70-72]. This is one of the developing sources of single photons [70-72] which can be applied in quantum computing applications.

Although the properties of single cavities are well studied, systems of coupled cavities constitute a more complicated and somewhat less studied area. Theoretically, the coupling phenomena can be explained by the tight binding approximation [73] for photonic "atoms" similar to the solid state theory where tight binding model is widely used to describe band structure effects for electrons [74,75]. However this theory applies only to perfectly identical cavities.

The *resonant* properties based on WGM coupling phenomena have attracted a significant interest of groups in Japan [61, 73, 76-79], Germany [56-59, 80-83] and Ireland [84-86]. These groups started using techniques of selection of spheres with almost identical positions of WGMs. Through these techniques normal mode splitting (NMS) effects in bispherical systems [76-78, 80-84] and in chains [78, 85, 86] were observed. One of the interesting recent results in this area was connected with observation of coupling between azimuthal modes in bispheres assembled in microwells [80]. Generally, these groups have been concentrating their studies on the spectral manifestations of strong coupling effects in such structures. The optical transport effects such as spectral

transmission properties and efficiencies of coupling have received less attention in these studies.

Developing such transport studies requires special techniques of measurements such as using local sources of light. Such techniques were developed in the previous studies [87, 89, 90] of Prof. Astratov's group. When I joined Prof. Astratov's group in August 2006, it was one of the leading groups in studies of optical coupling and transport phenomena in mesoscopic systems of coupled microspheres. Several important results were obtained in this group prior to beginning of my thesis work. These include observation of optical transport in disordered chains of microspheres [87], modeling of coupling efficiencies and spectral effects in size-mismatched bispheres [88], observation of percolation of WGMs in 3D systems of coupled cavities [90], and observation of nanojet-induced modes (NIMs) in chains of cavities [89].

Some aspects of these phenomena still required more detailed studies. These include a necessity to characterize the coupling constant between the spheres for spheres with different sizes, to better understand the spectral and spatial properties of coupled modes in bispheres, and more sophisticated circuits assembled on the substrate. Thus, one of the objectives of this thesis work is to use techniques of local sources of light in combination with spectroscopy and microscopy in order to further advance the fundamental understanding of coupling of WGMs in circuits of microspheres.

The second direction of the thesis is connected with studies of *nonresonant* mechanisms of propagation of light in chains of spheres. This direction of research is related to novel phenomena of formation of so-called "photonic nanojets" [93-97] produced by single spheres in response to illumination by incident plane waves. The

results [90] show that in chains of microspheres the nanojets are periodically reproduced along the chain giving rise to a new type of modes called in this paper "nanojet-induced modes" (NIMs) These modes have very interesting properties, the main one is an ability to form progressively smaller spot sizes along the chain [90]. However some of the properties of these modes, such as their propagation losses and their spatial distributions, were not studied in sufficient detail in the previous work.

The start of this thesis work was actually initiated by studies of properties of WGMs not in microspheres, but in semiconductor micropillars. The spectral response of the WGMs from the semiconductor micropillars was observed by Professor Vasily Astratov and his Sheffield's colleagues during his sabbatical stay at the University of Sheffield in April-July 2006. The structure of semiconductor micropillars is formed by two Bragg mirrors with a cavity in between [11, 15, 98, 99]. A layer of light-emitting quantum dots (QDs) is grown in the middle of the cavity to study light-matter coupling. Conventionally, studies on emission properties of semiconductor micropillars have been performed from the top of the pillars [12-14, 16-22]. Professor Astratov suggested using a different experimental configuration with excitation and collection of the micropillars' emission at normal to their sidewall surface.

In this geometry narrow peaks with almost equal separations were observed in the emission spectra that revealed [11] the presence of WGMs in such cavities. This observation was surprising since the mechanism of confinement of WGMs is nontrivial. Previously WGMs have been observed in microdisks [23-31] where the vertical confinement is provided due to very high refractive index contrast between the semiconductor and air. In micropillars, in contrast, the vertical confinement between the

central cavity and Bragg mirrors is much weaker. In addition the mirrors are formed by layers with alternating index of refraction. It is difficult to expect WGMs in such structures due to their possible leakage from the central cavity into the adjacent mirrors. More detailed theory based on modeling of the electromagnetic (EM) processes in such structures was necessary in order to explain the properties of WGMs. Thus, the numerical modeling of WGMs in semiconductor micropillars became another objective of this thesis work.

This thesis consists of four Chapters. In Chapter 1 we give an introduction to resonant and nonresonant modes in such structures. Chapter 2 is devoted to modeling of WGMs in semiconductor micropillars. We developed 3D finite-difference time-domain (FDTD) modeling of WGM in micropillars [11] based on the effective medium approximation for the Bragg mirrors. We achieved very good agreement of calculated WGM peak positions [11] with experimental spectra obtained at Sheffield for micropillars with different sizes and different shape.

In Chapter 3 we present the results of detailed studies of the optical coupling effects in supermonodispersive bispheres. We developed techniques of size sorting of microspheres [100] with an unprecedented accuracy of ~0.03 %. In a special configuration of the experimental setup we observed unusual and characteristic kites [100] in spectral images of such bispheres. Using various experimental geometries we quantified the dependence of the coupling constant on the sphere size for maximally coupled fundamental modes.

In Chapter 4 we present the results of studies of NIMs in very long (up to 100 cavities) and straight chains of spheres. We experimentally observed extremely small

losses smaller than 0.08 dB/sphere in such chains [92]. The numerical modeling of NIMs spatial distribution performed in this work revealed that these modes have a spatial period equal to the size of two cavities in the case of polystyrene microspheres.

1.2 Resonant modes in circular cavities

1.2.1 Whispering gallery modes in cylinders

In this section we present basic information about WGMs in single cylindrical cavities [101, 102]. When the light enters the cylindrical structure, it is trapped inside due to total internal reflection (TIR). This confinement of the EM field inside a cylindrical cavity attracts much attention in many applications. Using simple geometrical optics, a cylinder of radius a with refractive index n, and a ray of light propagating inside, hitting the surface with angle of incidence θ_{in}, are shown in Figure 1(a). If $\theta_{in} > \theta_c = \arcsin(1/n)$ where θ_c is the critical angle and n the refractive index, then TIR occurs.

This simple geometric picture immediately leads to the concept of resonances along the circumference. For a large cylinder ($a \gg \lambda$), the trapped ray propagates close to the surface, and traverses a distance $\approx 2\pi a$ in one round trip. If one round trip exactly equals l wavelengths in the medium, then one expects a standing wave to occur as shown in Figure 1(b). This condition translates into

$$2\pi a \approx l(\lambda/n). \tag{1.1}$$

It is conventional to define for this system a dimensionless size parameter

$$x = 2\pi a / \lambda \tag{1.2}$$

in terms of which the resonance condition is

$$x = l/n \tag{1.3}$$

where l is angular momentum that represents the number of wavelengths along the circumference.
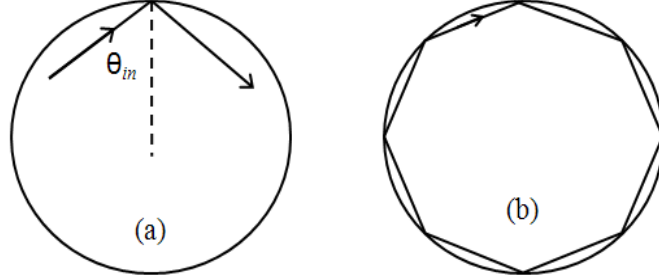
FIGURE 1.1: Cross sectional view of a cylinder.
(a) Totally reflected ray at glancing angle. (b) A resonance formed when optical path length equals the integer number of wavelengths [103].

In order to obtain the mode profile of a cylindrical cavity, more rigorous wave optics analysis should be employed. A plane monochromatic EM wave incident into a dielectric cylinder (with dielectric constant ε) will circulate inside the cylinder due to internal reflections when the resonant condition is reached. The total EM field satisfying Maxwell's equations together with the boundary conditions can be derived from the B_z component written as [96],

$$B_z = e^{-i\omega t} \begin{cases} \sum\limits_{n=-\infty}^{\infty} a_n J_n(n_e kr)e^{in\phi}, & r < a, \\ \exp(ikx) + \sum\limits_{n=-\infty}^{\infty} b_n H_n(kr)e^{in\phi}, & r > a, \end{cases} \qquad (1.4)$$

where a is the cylinder radius and $\{r,\phi\}$ are cylindrical coordinates, with

$$a_n = \frac{i^n}{W_n} n_e \left[J_n'(ka)H_n(ka) - J_n(ka)H_n'(ka) \right] \qquad (1.5)$$

and

$$a_n = \frac{i^n}{W_n} n_e \left[n_e J_n(n_e ka) J_n'(ka) - J_n'(n_e ka) J_n(ka) \right], \qquad (1.6)$$

where $W_n = J_n'(n_e ka) H_n(ka) - n_e J_n(n_e ka) H_n'(ka)$, while J_n and H_n denote Bessel and

Hankel functions, respectively, and $n_e = \sqrt{\varepsilon}$. Finally, the components of the electric field

are

$$\{E_x, E_y, E_z\} = \frac{i}{\varepsilon k} \left\{ \frac{\partial}{\partial y} B_z, -\frac{\partial}{\partial x} B_z, 0 \right\}. \qquad (1.7)$$

Field patterns represented by $|B_z(x,y)|$ in Eq. (1.4) are shown in Figure 1.2. A

nonresonant field with focusing properties of the dielectric cylinder with radius of $a = $

2.17 in wavelength unit is illustrated in Figure 1.2(a). The field pattern of the radiation

that circulates inside the cylinder is shown in Figure 1.2(b) when the resonant condition

is satisfied with a = 2.16226047 in wavelength units. This resonance enhances the

external field in the vicinity of the cylinder. This field pattern corresponds to the angular

index m=22 for WGM resonances [102].

The photoluminescence (PL) spectra of the WGMs in a cylindrical structure [104]

are shown in Figure 1.3. In this experiment small, highly luminescent aluminosilicate

microtubes of ~7 – 8 μm diameters were fabricated. Light propagating inside the

microtube can be spatially constrained to travel along the rim of its cross-section, thus

becoming trapped in a WGM. Such microcylinders support optical WGM at a Q-factor of

3200 [104]. The emission spectra show strong polarization properties as shown in Figure

1.3. The sharp peaks dominating the spectrum for a polarizer orientation parallel to the

microtube axis correspond to linear polarized light with the electric vector oscillating

parallel to the axis of the cylinder [104].
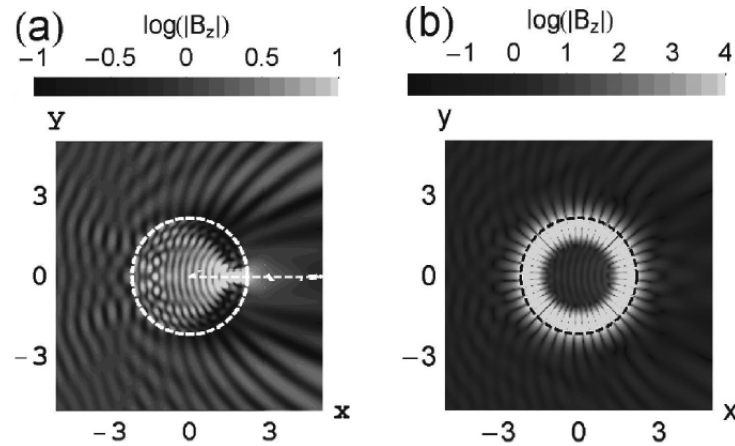
FIGURE 1.2: Field patterns represented by $\left| B_z(x,y) \right|$.

(a) In non-resonant, (b) in resonant scattering conditions. A dielectric cylinder has the dielectric constant $\varepsilon = 4$, while its radius, in units of the wavelength λ, is in (a) a = 2.17 and in (b) a = 2.16226047 corresponding to the angular index of 22 WGM resonance [102].
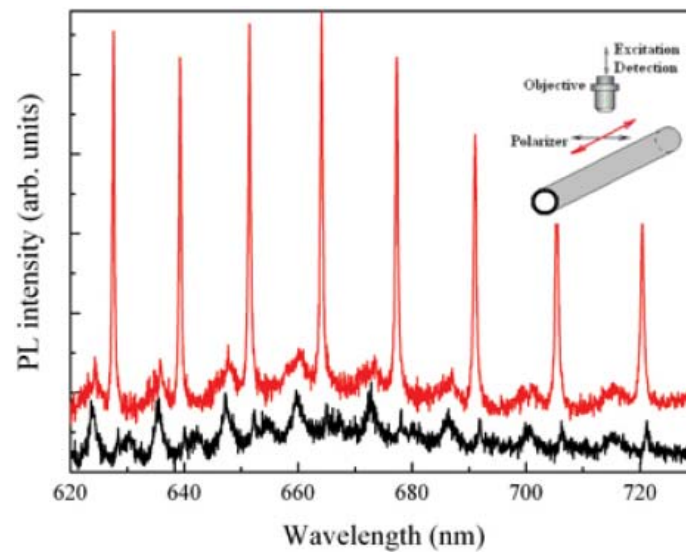
FIGURE 1.3: Room-temperature PL spectra of a single free-standing microtube. The spectra were recorded with polarizer orientation parallel to the microtube axis (red trace) and with polarizer rotated by 90° (black trace) [104].

This cylindrical cavity can be compared to the microdisk structure which can be seen as part of a cylindrical cavity. In the cylindrical cavity the mode propagates along the cylinder axis, i.e. z axis, whereas the modes in a microdisk are confined in the z

direction and propagate around the disk [105]. Due to the boundary conditions imposed by the top and bottom boundaries of the disk, the wave vector in z direction, k_z, is determined solely by the disk thickness which is different from a cylindrical cavity [105]. This will be discussed in the next chapter.

1.2.2 Whispering gallery modes in microspheres

In spherical cavities [43-67], there are three mode numbers (l, m, n) with polarization (TE_l^n or TM_l^n) to describe the characteristics of the WGMs due to the rotational symmetry. Calculated EM field intensity distribution ($|E|^2$) [105] on a sphere surface for a microsphere with $R = 1.4$ μm and n = 1.57 is shown in Figure 1.4. The radial number n indicates the number of peaks in the radial direction of the sphere whereas the angular number l represents the number of modal wavelengths that fits into the circumference of the equatorial plane of the sphere. Figure 1.4 shows three examples with the same l =16 and n =1 for different m numbers. The azimuthal mode number m defines the number of maxima along the equator as shown in Figure 1.4(c) where $m = 16$. The fundamental modes are defined in the equatorial plane of spheres corresponding to a condition $|m|=l$. In free standing spheres the azimuthal modes are degenerate by the symmetry of the problem. This degeneracy however can be removed by the presence of the substrate or any other local factor.

Theoretical studies can use the 3D rotational symmetry in a single sphere when they are in free space. However, in most real applications the substrate plays a very important role in defining the optical modes due to the interaction of the evanescent field tail outside the sphere with the substrate. Due to the substrate, the optical symmetry axis can be defined along the axis perpendicular to the substrate. Accordingly, all the optical

resonant modes of a single sphere on a substrate can be defined along the plane that is

parallel to the substrate [56] as shown in Figure 1.4(c).
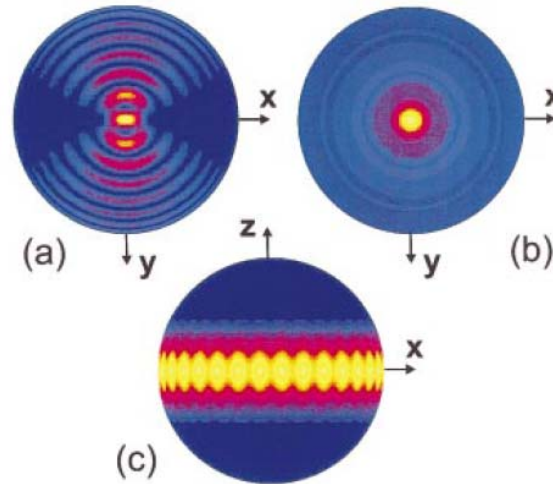
FIGURE 1.4: Calculated EM field intensity distribution ($|E|^2$) on a sphere surface.
The microsphere has $R = 1.4$ μm and n = 1.57. (a) TE_{16}^1 mode with $m = \pm 1$ ($\lambda =$ 688.5 nm), dipole oscillates in x direction, (b) TE_{16}^1 mode $m = 0$ ($\lambda = 666.9$ nm), dipole oscillates in z direction. Comparison of the corresponding picture of a WGM TE_{16}^1 with $m = 16$ is shown in (c) [105].

In addition, the substrate also interacts with the azimuthal modes due to their

spread on the equator for small m numbers. Different azimuthal mode patterns observed

from a sphere of size 286 μm (thick curves) depending on different azimuthal mode

numbers [60] are shown in Figure 1.5. The azimuthal mode numbers vary from $m = l$

(fundamental mode, single lobe) to $m = l$-7 (lower azimuthal mode, eight lobes). The

inset shows the sphere formed at the end of a fiber with a tapered fiber probing the

angular patterns with respect to the equatorial plane. The fiber that supports the sphere

has very similar effect as a substrate in this case.

The largest intensities are observed for the peaks that are furthest from the

equatorial plane at 90°. For instance, the angular mode pattern with azimuthal mode

number $m = l\text{-}7$ shown on the bottom of Figure 1.5 has two the largest intensity peaks located about 86 and 94 degrees. The separation of these two largest peaks from the center (90 degrees) is about 4 degrees. Therefore, smaller azimuthal modes ($m \ll l$) will interact more strongly with the substrate, lifting the degeneracy of the azimuthal modes and broadening the experimentally observed WGM peaks [56].
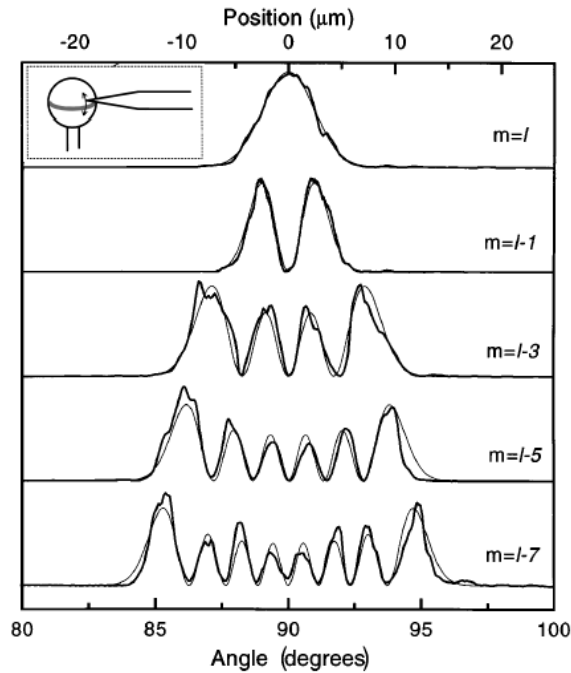
FIGURE 1.5: Experimental and theoretical angular patterns in a microsphere. Patterns are from different resonant TE modes in a fused-silica microsphere of size 286 μm (thick curves) and their fitted patterns from theory (thin curves) [60]. The inset shows the sphere with a probe along the equatorial plane.

The wave optics description of the WGMs in a sphere is summarized below based on review papers [52, 106, 107]. A dielectric sphere with dielectric constant distribution $\varepsilon(r)$ that depends on the radius r only is considered. The electric field in the sphere obeys the Maxwell equation

$$\nabla \times (\nabla \times E) + \frac{\varepsilon(r)}{c^2} \frac{\partial^2 E}{\partial t^2} = 0 \qquad (1.8)$$

where c is the speed of light in the vacuum. The electric field can be presented as

$$E = \int_0^\infty e(r)\exp(-i\omega t)d\omega ,\qquad (1.9)$$

we can rewrite the Eq. (1.8) as

$$\nabla\times(\nabla\times e)+k^2\varepsilon(r)e = 0 \qquad (1.10)$$

where $k = \omega/c$ is the wave vector. Eq. (1.10) may be solved in terms of TE and TM modes. Keeping in mind that $\nabla\cdot(\varepsilon e) = 0$ we write

$$e = \sum_{l,m}\frac{1}{r}\left[\Psi Y_{l,m}+\frac{1}{\varepsilon(r)}\nabla\times(\Phi Y_{l,m})\right]\qquad (1.11)$$

where radial functions Ψ and Φ stand for the TE and TM modes, respectively, and $Y_{l,m}$ are vector spherical functions with angular number l and azimuthal number m. Radial field distribution for TE modes, for instance, of a dielectric sphere cavity can be described by

$$\frac{\partial^2\Psi}{\partial r^2}+\left[k^2\varepsilon(r)-\frac{l(l+1)}{r^2}\right]\Psi = 0 \qquad (1.12)$$

where l is angular momentum number ($l = 0, 1, 2, 3\cdots$ for a sphere). Electric field distribution has a dependence of $\Psi(r)/r$ for a sphere. Eq. (1.12) has an exact solution for a homogeneous dielectric spherical cavity with $\varepsilon(r) = \varepsilon_0 = const$. This solution reads

$$\Psi(r) = J_{l+1/2}(kr) \qquad (1.13)$$

where $J_{l+1/2}(kr)$ is the Bessel function of the first kind.

The mode spectrum is determined by the boundary conditions $\Psi(r)\to 0$ for $r\to\infty$ and 0. For the case of high TE mode order ($l \gg 1$)

$$k_{l,q} \cong \frac{1}{a\sqrt{\varepsilon_0}}\left[l + \alpha_q \left(\frac{l}{2}\right)^{1/3} - \sqrt{\frac{\varepsilon_0}{\varepsilon_0 - 1}} + \frac{3\alpha_q^2}{20}\left(\frac{2}{l}\right)^{1/3} + O\left(l^{-2/3}\right) \right] \qquad (1.14)$$

where a_q is the qth root of the Airy function, a is the radius of the resonator, A$i(-z)$, which is equal to 2.338, 4.088, and 5.521 for q=1, 2, 3, respectively. The expression for TM WGM spectrum can be obtained analogously [52]

$$k_{l,q} \cong \frac{1}{a\sqrt{\varepsilon_0}}\left[l + \alpha_q \left(\frac{l}{2}\right)^{1/3} - \frac{1}{\sqrt{\varepsilon_0(\varepsilon_0 - 1)}} + \frac{3\alpha_q^2}{20}\left(\frac{2}{l}\right)^{1/3} + O\left(l^{-2/3}\right) \right] \qquad (1.15)$$

One of the basic properties of a whispering gallery resonator (WGR) is the relatively small volume occupied by the electromagnetic field of the mode in comparison to the total volume of the cavity. This effect takes place because WGMs tend to propagate close to the surface of the cavity, so that the electromagnetic intensity in middle of the cavity is small in most cases. The mode volume of the WGMs is especially important for nonlinear applications of the resonators. WGRs can have mode volumes orders of magnitude less than in Gaussian-mode resonators. The mode volume for a spherical WGR can be estimated as [57]

$$V = 3.4\pi^{3/2}\left(\frac{\lambda}{2\pi n}\right)^3 l^{11/6}\sqrt{l - m + 1} \qquad (1.16)$$

where λ is the wavelength of the pumping light.

Another important parameter is the Q-factor. The Q-factor is related to the lifetime of light energy in the resonator mode (τ) as Q = $\omega\tau$, where ω is the frequency of the mode. Generally Q is defined to be [67]

$$Q = 2\pi \frac{Energy\ stored}{Energy\ loss\ per\ cycle} \qquad (1.17)$$

The quality factor is severely affected by the deformities in the shape and roughness of the microsphere. The modes experience variable refractive index contrast at different points along the circumference and can be estimated as [103]

$$\frac{1}{Q} = \frac{1}{Q_{rad}} + \frac{1}{Q_{scat}} + \frac{1}{Q_{cont}} + \frac{1}{Q_{mat}} \tag{1.18}$$

where Q_{rad} is intrinsic radiative loss, Q_{scat} is scattering losses on residual surface inhomogeneities, Q_{cont} is losses induced by surface contaminants, and Q_{mat} is material losses. An additional and most important factor influencing Q-factors in practical structures assembled on substrate is represented by the mode leakage in the substrate which will be discussed in more detail in Chapter 3.

1.3 Nonresonant modes in microspheres

1.3.1 Sphere as a thick lens

A dielectric sphere can be treated as a thick lens whose front (R_1) and back (R_2) radii of curvature are equal to half of its thickness (d_l). This introduction starts from the analysis of the focusing properties of the thick lens. When the thickness of the lens along its optical axis is not negligible, the refractions at the front and back surfaces have to be considered separately. In the limit of geometrical optics both refractions seem always considered separately.

The geometry of a thick lens with various quantities is shown in Figure 1.6. In this geometry, the effective focal length, f, is given by [108]

$$\frac{1}{f} = (n_l - 1)\left[\frac{1}{R_1} - \frac{1}{R_2} + \frac{(n_l - 1)d_l}{n_l R_1 R_2} \right] \tag{1.19}$$

where n_l, the refractive index of the lens. The back focal length, f_b, can be calculated

from $f_b = f - |h_2|$. The value of h_2 is given by

$$|h_2| = \frac{f(n_l - 1)d_l}{R_1 n_l}.$$
(1.20)

Using Eq. (1.19) and (1.20), the back focal length is

$$f_b = \frac{n_l R_1 R_2 - d_l R_2 (n_l - 1)}{(n_l - 1)[n_l (R_2 - R_1) + d_l (n_l - 1)]}.$$
(1.21)

It is noted that when the numerator of Eq. (1.21) is zero, the focal point, F_i, locates at the

vertex of the back surface, V_2 (for $n_l > 1$). Therefore, the focal point is exactly at the back

surface of the lens when

$$R_1 = d_l \left(\frac{n_l - 1}{n_l} \right).$$
(1.22)

For example, if $n_l = 2.0$, then R_l should be half of d_l, which is exactly the size of a sphere.
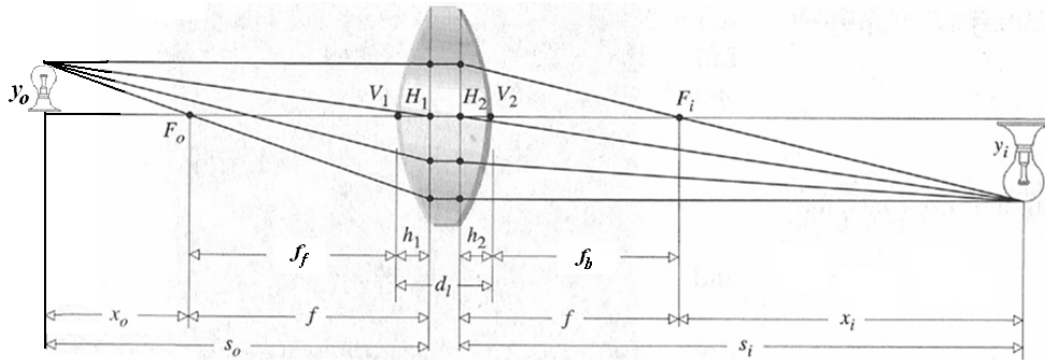
FIGURE 1.6: Thick lens geometry [108].

The sphere is a special case of the thick lens where the thickness of the lens is

twice of the radius. Using this condition for a sphere, Eq. (1.21) can be rewritten as

$$f_b = \frac{R(2 - n_l)}{2(n_l - 1)^2},$$
(1.23)

where R is equal to R_1 and R_2. Eq. (1.23) indicates that when $n_1 > 2$, then $f_b < 0$, which

means the focal point is located inside the sphere. For $n_1 < 2$, the focal point is outside the

sphere. This simple geometrical optics analysis provides a rough estimation of how a

sphere works as a thick lens in making a focal point in the back surface.
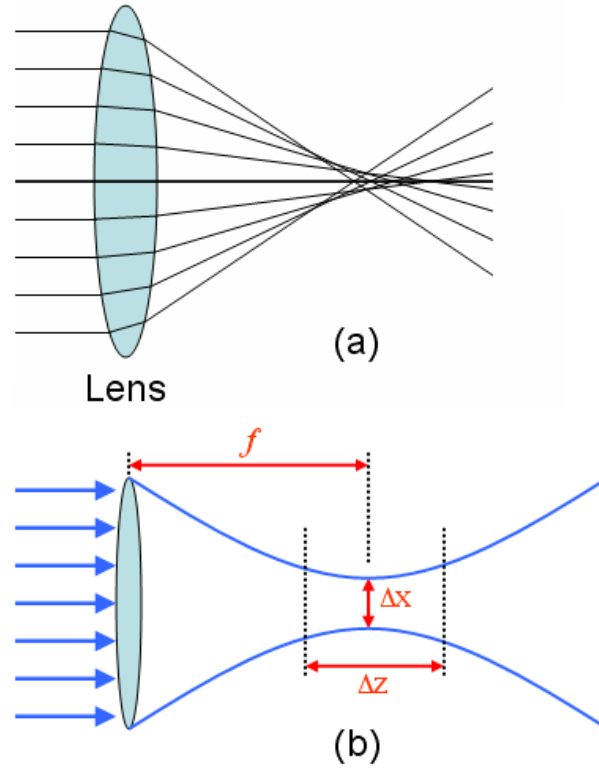
FIGURE 1.7: Schematic diagram of lens focusing.
(a) Geometrical optics focus of a lens. (b) Wave optics focusing of a lens. Δx: focal spot size. Δy: depth of focus [109].

A schematic diagram of the geometrical optics focus of a lens is shown in Figure

1.7(a). Using the wave optics, the diffraction-limited focal spot size (Δx) and depth of

focus (Δz) of a lens are defined as [109]

$$\Delta x = 2.44 \lambda \frac{f}{D} , \qquad (1.24)$$

and

$$\Delta z = 2.44\lambda \left(\frac{f}{D} \right)^2 \qquad\qquad (1.25)$$

where f, and D are the focal length, lens diameter. These quantities are illustrated in Figure 1.7(b) with 2D cross-section of irradiance distribution from a lens.

1.3.2 Photonic nanojets in a microsphere

The photonic nanojet is a narrow, high-intensity beam that propagates into the background medium from the shadow-side surface of a plane-wave illuminated lossless dielectric microsphere [93]. When the size of a sphere is small enough and comparable to the wavelength of light, the focusing beam at the back surface of the sphere has shown very interesting properties [110]: (1) Such focusing is a nonresonant phenomenon, i.e., it can appear for a wide range of sphere size if the refractive index contrast relative to the background medium is less than about 2:1. (2) The intensity of light in the middle of the focused spot exceeds that for the illuminating wave by a factor of 1000. (3) The focused spot has the full-width-half-maximum (FWHM) beamwidth between one-third and one-half wavelength in the background medium and is only weakly dependent upon the size of the dielectric sphere. A transverse beamwidth as small as 0.3λ has been reported [97]. (4) The beam keeps a subwavelength FWHM over a propagation distance grater than 2.5 λ [94, 124]. These specific features – subwavelength FWHM and micron propagation distance – are unreachable with a classical Gaussian laser beam focused by a high numerical aperature objective [124]. As has been pointed out by Flecher et al. [152], when the diameter of the dielectric sphere is reduced to be on the order of the wavelength, the distribution of light intensity close to the surface of the sphere cannot be analyzed by the diffraction theory [94].

The calculated external light intensity distribution resulting from illuminating dielectric spheres with n = 1.59 with an x-polarized, z-propagating plane wave with unit intensity and wavelength λ = 400 nm is shown in Figure 1.8. For a dielectric sphere with D = 1 μm (Figure 1.8(a)), a subdiffractional light jet protrudes from the shadow side of the dielectric particle. The FWHM of the jet is 130 nm which is much smaller than the incident wavelength λ = 400 nm. The spheres with D = 2 and 3.8μm produce the nanojet with FWHM of 150 and 190 nm, respectively (Figure 1.8(b) and (c)). As the diameter
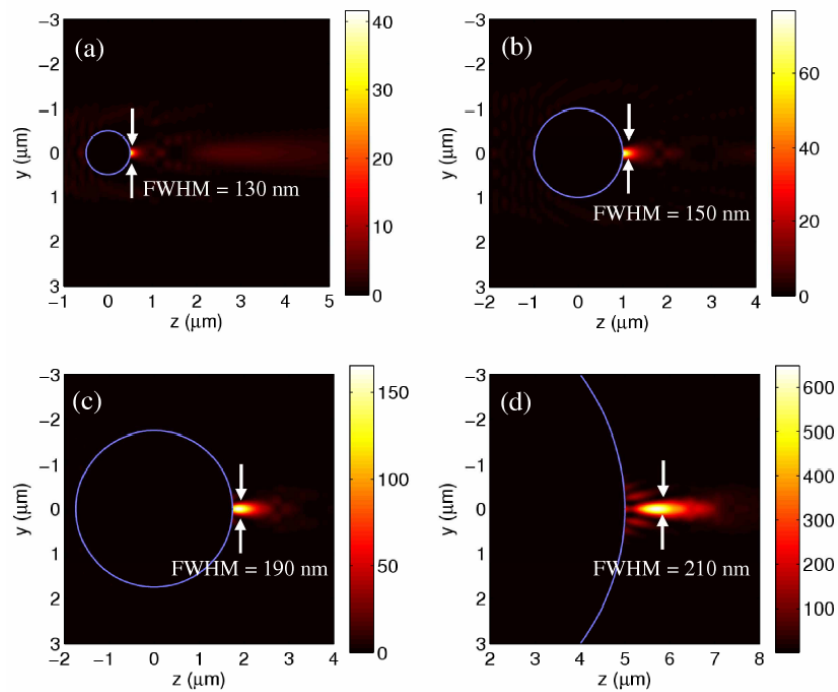
FIGURE 1.8: Photonic nanojets.
They are generated by illuminating dielectric spheres (n = 1.95) with a λ = 400 nm, x-polarized, z-propagating incident plane wave in vacuum [94]. The near-field intensity distributions are calculated with Eq. (2). (a) Sphere diameter D = 1 μm. (b) D = 2 μm. (c) D = 3.5 μm. (d) D = 8 μm.

increases, the light jet starts to emerge and move away from the dielectric sphere (Figure 1.8(d)). The maximum intensity and FWHM of the light jet also increase as the size of

the dielectric sphere increases. For a microsphere with diameter D = 3.5μm (Figure 1.8(c)), a tight focus of light (photonic nanojet) is created with high peak intensity ($I_{max} \approx$ 160I_0), subdiffractional waist (FWHM = 190 nm), and propagating in micron scale. It is interesting to note that the photonic nanojets have strong radiative mode properties as well as the evanescent fields outside the sphere surface.

Since the photonic nanojet by a dielectric microsphere started attracting attention in 2004, many applications have been suggested [94, 110] using this nonresonant optical properties of microspheres. These interesting properties have been used in several application areas such as nanoparticle detection [94], detection of subwavelength pits in the optical data-storage disks [115, and low loss optical transport in a size detuned microsphere chain [90].

The first example of detecting nanoparticles was the theoretical calculation result which was based on the enhanced backscattering intensity by dielectric particles of sizes between 1 and 100 nm [94]. The strong perturbation in the back scattering signal introduced by a small particle was used [94] to detect a nanoparticle as it moved through the photonic nanojet as shown in Figure 1.9(a). A dielectric microsphere (n = 1.59, r = 1.75μm) was illuminated by a collimated beam (λ = 400 nm). A gold nanoparticle (n = 1.47 $-j$1.95, d = 20 nm) moved through the photonic nanojet that is located close to the back surface of the microsphere. Figure 1.9(b) shows the normalized backscattering intensity of this two-sphere system [94] as the position of the nanoparticle is varied with respect to the microsphere position. It is clearly seen that an increase of about 40% in the normalized backscattering is introduced by the strong perturbation due to the nanoparticle. Using this method, the sizes of the small particles can be characterized by examining the

variation of the backscattering intensity. In this example, the backscattering of a photonic nanojet has been demonstrated to provide the resolution of 1 nm precision of a single nanoparticle [94].
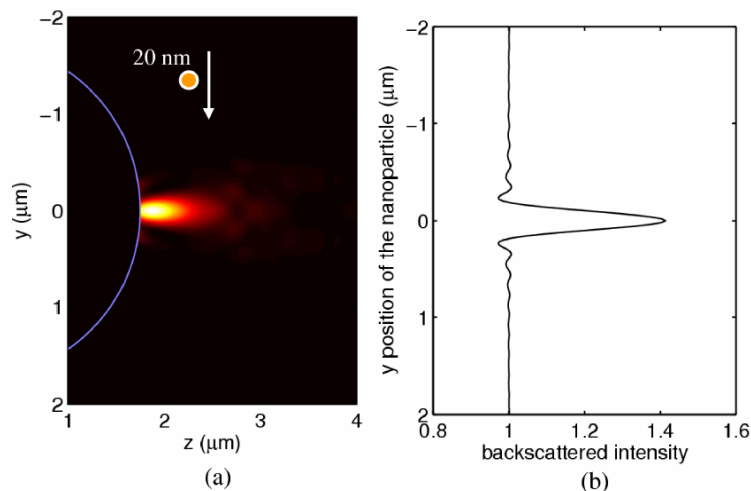
FIGURE 1.9: Backscattering of a nanoparticle moving through a photonic nanojet.
(a) A 20 nm nanoparticle and the photonic nanojet. (b) Normalized backscattering intensity as a function of the position of the nanoparticle. An increase of 40 % backscattering intensity is observed [94].

Another interesting application of the photonic nanojet is the detection of subwavelength pits [110, 111] in the optical data-storage disks as illustrated in Figure 1.10. In this case a microwave wavelength jet was used instead of optical wavelength for the experiment and the simulation. This microwave wavelength experiment can easily be scaled down to optical wavelength range. Figure 1.10(a) and (b) shows the microwave intensity distributions of the backscattering of the microwave jet by the Duroid-coated aluminum plate for the no-pit and pit cases from the FDTD computations, respectively. The fit case shown in Figure 1.10(b) shows a strong microwave intensity that is localized in front of the pit and the magnitude of the intensity is about 225 times bigger than the incident microwave intensity. This backscattered wave from the pit decreases faster as it

propagates backward from the pit compared to the decrease in the no-pit case. This difference in the intensity decay is illustrated in a graph along line AB as shown in Figure 1.10(c). In this experiment a much smaller area of pit compared to the current BluRay^{TM} device was detected experimentally due to the interaction with the small and intense microwave jet.
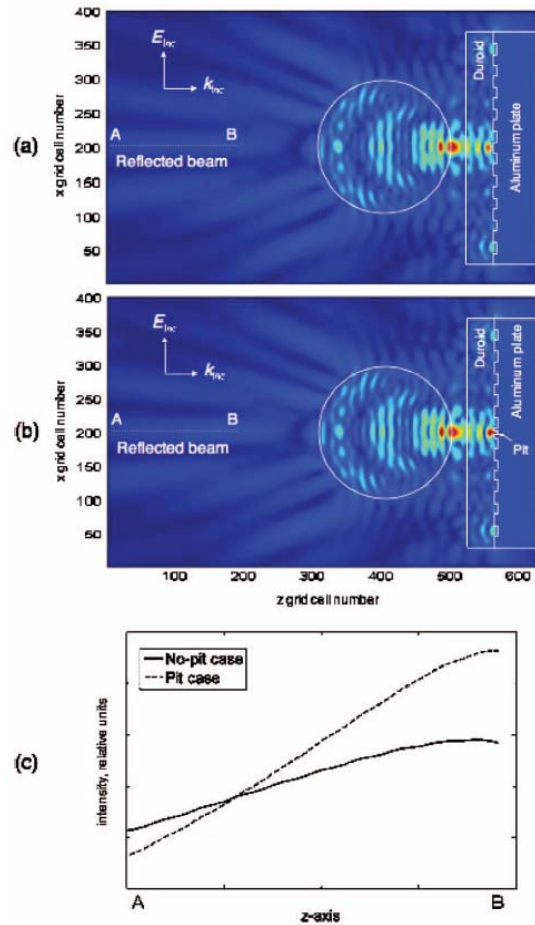
FIGURE 1.10: photonic nanojets for the detection of pits of data-storage disks. FDTD-calculated microwave intensity distributions are shown. (a) Interaction of the photonic nanojet for no-pit case. (b) The photonic nanojet interacting with the pit in the aluminum plate. (c) The backscattered intensity decreases faster with propagation distance from B to A for the pit case than no-pit case [110].

1.3.3 Nanojet induced modes in a microsphere chain

The optical transport of coherent microsphere chains have been studied [93] recently for two different transport mechanisms: (i) tight-binding between WGMs, and (ii) coupling by periodical focusing effects. In a chain with identical spheres the WGMs can couple very efficiently. This highly efficient optical coupling can be achieved in the identical spheres by evanescent fields that overlap with the modes of neighboring spheres. Figure 1.11 (a) shows the electric field intensity distribution of a chain of five touching microspheres with a refractive index of 1.8 and a diameter of 3 μm. Plane waves were launched along the axis of the chain from left to right in Figure 1.11. Light of wavelength $\lambda = 430.889$ nm which is a WGM resonance propagates from left to right via evanescent coupling [93]. They show the intensity profiles of highly efficient coupling of WGMs inside each sphere. Peak intensity of each sphere with respect to the distance between their centers is shown Figure 1.11(b). The maximum peak intensity in this case is shown to be close to 6000 and input and output intensities close to 2000.

However, light with wavelength $\lambda = 429.069$ nm propagates along the nanojet-including microspheres with index of 1.59 as shown in Figure 1.12(a) [93]. In this case, the constituent spheres are nonevanescently coupled due to the radiative nature of photonic nanojets [93]. Figure 1.12(a) shows the intensity distribution of each constituent sphere of the chain consisting of microspheres that have a refractive index of 1.59 and induce photonic nanojets. It is seen that a WGM resonance ($\lambda = 429.069$ nm) is weakly excited in each sphere by the evanescent-field component of the nanojet, and its propagation through the sphere chain is achieved via evanescent coupling [93]. However,

due to the radiative nature of the nanojet, optical coupling between neighboring spheres is

not
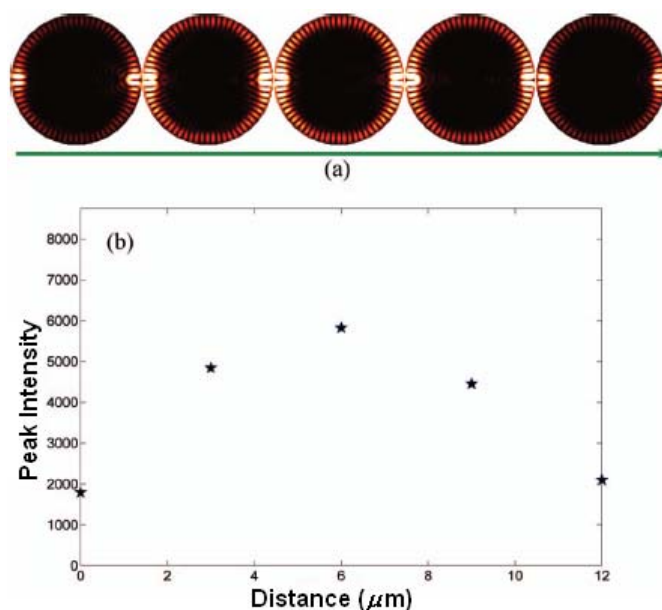
FIGURE 1.11: FDTD calculation for a chain of five microspheres at near-resonance.
(a) Electric field intensity distribution of a chain of five touching microspheres
that have a refractive index of 1.8 and a diameter of 3 μm. Light of wavelength λ
= 430.889 nm propagates from left to right. (b) Peak intensity of each constituent
sphere as a function of the distance between their centers [93].

efficient. Figure 1.12(b) shows peak intensity of each constituent sphere as a function of

the distance between their centers. The maximum peak intensity of this case is just above

600 which is approximately one order of magnitude smaller than the maximum peak

intensity of the resonant case. Also the output intensity of about 200 is smaller than the

input intensity of 550. The incident light can propagate efficiently only as far as the third

sphere, and the intensities within the fourth and fifth spheres go down dramatically [93].

In contrast to chains made from identical spheres, size-detuned (~3 % size

dispersion) microsphere chains were studied in dye-doped polystyrene microspheres with

sizes in the 2-10 μm range [90]. Since most commercial microspheres have a standard

size variations ~1-3%, it is not easy to select identical spheres to make resonant microsphere chains. This non-resonant optical transport has been observed for the first time in recent study [90] by using the scattering measurements.
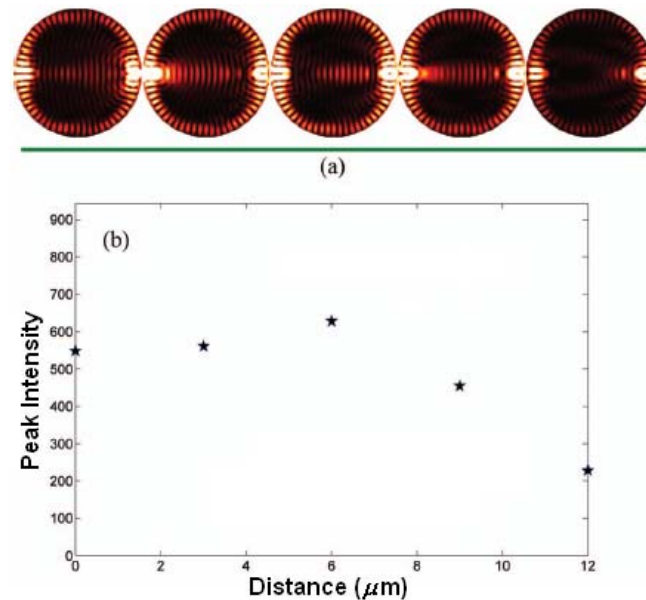
FIGURE 1.12: FDTD calculation for a chain of five microspheres at off-resonance.
(a) Electric field intensity distribution of a chain of five touching microspheres that have a refractive index of 1.59 and a diameter of 3 μm. Light of wavelength λ = 429.069 nm propagates from left to right. (b) Peak intensity of each constituent sphere as a function of the distance between their centers [93].

In this work the scattering of light from the axis of the chain has been captured by the imaging system to directly visualize the nanojets emerging in the vicinity of the touching points between the spheres [90]. By directly observing a series of photonic jets at the shadow side of multiple spheres, a characteristic feature of NIMs, the fluorescence from the source is gradually converted into NIMs away from such source [90]. By performing measurements at long distances from the source, propagation losses of less than 0.5 dB per sphere for NIMs were demonstrated [90].

The propagation of NIMs in size-detuned chain is illustrated in Figure 1.13. Three (leftward) dye-doped microspheres are locally excited and the NIMs propagate along the chain of dye-doped microspheres as shown in Figure 1.13(a). Fluorescent light propagation is shown in Figure 1.13(b) with color bars. It is clearly seen that the input beam is converging into small spot at the end sphere due to the NIMs propagation. A particularly interesting result consists in observation of a decrease of the cross-sectional FWHM of bright spots along the chain as shown in Figure 1.13(c). It is suggested that this reduction in spots sizes is a result of filtering of NIMs occurring in the course of light propagation along the chain. This mode conversion process is very useful in making a small spot size beam from a large size input beam.
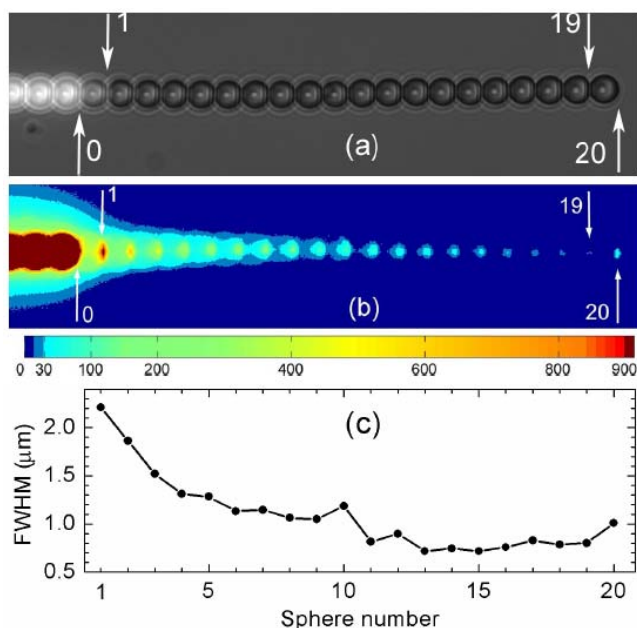
FIGURE 1.13: NIMs in a chain of 2.9 μm spheres [90].
      (a) Image obtained with the background white light illumination. Three spheres (left) are pumped. (b) Same chain imaged without background illumination due to propagation and scattering of light originating from the FL source. (c) Cross-sectional FWHM of bright spots measured in unexcited spheres perpendicular to the chain.

1.4 Conclusions

In this chapter the optical properties of microspheres and their chains are considered for two cases: the resonant WGMs and their coupling effects and the nonresonant optical effects connected with periodic focusing of light in chains of microspheres. Whispering gallery modes are the guided modes inside the microsphere by the total internal reflection along the index difference between the microsphere and its surrounding media. Due to the high Q-factors, WGMs have been used for long time in optical communication applications [112-114] and sensing applications [115-118]. Another interesting application is the possibility of using WGMs in quantum cavity electrodynamics [4-6, 11, 13, 31, 42, 62] due to their high Q-factors and small mode volume. During last few decades the properties of WGMs in individual spheres have been well studied [43-67]. Q-factors above 10^9 are reported for sufficiently large spheres with submillimeter sizes [45-49].

Since the late 1990s new ideas have emerged in this area due to a possibility of integration multiple spheres in more complicated structures. These ideas have been stimulated by the proposals of coupled microrings [119, 120] and CROWs [121]. These ideas stimulated an interest in coupled bispheres [76-77, 80-84] and chains of cavities [78, 84, 86]. Important keystone results in this area include an observation of a strong coupling between WGMs in specially selected nearly identical spheres [76], an observation of optical transport effects in disordered chains of spheres [87] and modeling of WGM coupling efficiencies in size-mismatched spheres [88], an observation of coupling between a series of azimuthal modes in bispheres in microwells [80, 82], and an

observation of percolation of WGMs in 3D crystal-like structures formed by microspheres [90].

These studies also revealed some challenges of the technology of microsphere resonator circuits (MRCs). First, it was shown [87] that the size variations of spheres reduce the efficiency of WGM-based coupling. Supermonodispersive selection [100] of microspheres with $\delta \ll \kappa$, where δ is the deviation of the spheres' sizes and κ is the WGM coupling constant, is required. Second, the coupling constant varies for spheres with different sizes. Although it has been measured in some cases [76], the systematic studies of the coupling constant have not been performed in a broad range of spheres' sizes. Finally, the substrate is known to be an important factor [56, 100] when determining Q-factors of WGMs in individual spheres, but its role was not well studied in more complicated structures assembled on a substrate.

Similar studies and ideas have been developed in the area of semiconductor micropillars [11-22], microcylinders [122, 123] and microrings [32-39] which can be fabricated by conventional semiconductor technology.

The start for the research performed in this thesis was initiated by recent experimental results obtained in semiconductor micropillars during a sabbatical stay of Prof. Astratov at the University of Sheffield, UK, in April-July 2006. This subject is considered in Chapter 2 of this thesis where a separate introduction into cavity effects in micropillars can be found in Section 2.1. The main task of these studies was in developing numerical modeling techniques in order to fit the experimental spectra obtained from such micropillars. These spectra contained narrow peaks indicating presence of WGMs in such semiconductor micropillars.

Regarding resonant structures formed by the microspheres the objective of this thesis work was to develop techniques of selection of supermonodispersive spheres as well as techniques of tuning WGM resonances in order to use such spheres for studying fundamental coupling phenomena. More specific goals include understanding of the role of substrate in the formation of coupled photonic molecular states with specific geometrical configurations. It also includes measurements of the coupling constant through extensive studies of strong coupling between almost identical spheres with a wide range of average sizes. These results are presented in Chapter 3.

Finally, developing concept of photonic nanojets [93-97] and experimental observation of NIMs achieved by the group of Prof. Astratov [90] stimulated a significant interest in this subject worldwide [124-126].

This interest was mainly motivated by the subwavelength sizes of nanojets which opens a prospect for various applications of such structures. Many questions however remained unanswered regarding these novel modes. These questions include the level of fundamental losses for NIMs and the spatial distributions of these modes in long chains. The objective of this thesis work in this area was connected with obtaining more complete experimental information on these subjects through synthesis and spectroscopic study of light transport in extremely long chains of cavities. Another objective was connected with developing numerical modeling of NIMs in order to define the periodicity and other spatial characteristics of these modes. The results of studies of NIMs are summarized in Chapter 4 of this thesis work.

A few applications of using the spherical structures in real commercial products are the glass microspheres used for road marking paint (Langfang Wanda Glass

Microsphere Co.,Ltd, China) and the microring resonator all-optical switches in communications. The glass microspheres deposited in the road mark paint can make the car-light at night to reflect parallel to the ground and make the driver distinguish the direction better improving the safety. Companies such as Intel (Santa Clara, CA, USA) are investigating the microring resonators for silicon modulators and silicon lasers in order to integrate both optics and electronics on a single chip. The microring resonators provide a building block for fast, integrated, all-optical switches with lower cost and improve performance by reducing the number of optical-electronic conversions during a communication.

CHAPTER 2: SEMICONDUCTOR MICROPILLAR RESONATORS

2.1 Introduction

The semiconductor micropillar resonator is one of the optical microcavities with 3D confinement for photons. It has been studied due to interest in controlling light-matter coupling [14, 17-19, 42, 127] as well as due to potential applications [128, 129] of these structures as sources of single photons for quantum information processing. This structure obtained by etching of a planar semiconductor material has been known to support the discrete three-dimensionally (3D) confined modes, i.e., photonic dot states [12, 14, 15] along the axis of the pillar. When an internal light emitter is inserted into the structure, the efficient coupling into the photonic dot states can be achieved [12, 14, 15]. In addition, in the semiconductor laser application the vertical cavity surface emitting lasers [130, 131] can also be implemented with this structure.

It should be noted that due to its cylindrical symmetry the structure of semiconductor micropillars has a similarity with semiconductor laser microdisks [23, 24]. It is well-known [23] that microdisks support lasing WGMs. Despite similarity of the structures of semiconductor laser microdisks [23, 24] and micropillars [12, 14, 15] these structures have very different strength of the confinement of optical modes in vertical direction. In the case of microdisks it is defined by the refractive index contrast between a semiconductor (typically >3) and air, whereas in the case of micropillars it is defined by the index contrast between the central cavity (~3.5) and surrounding Bragg mirrors which

have somewhat complicated index distribution typically within 2.5-3.2 range. It is obvious that the refractive index contrast is much smaller in the case of micropillars, which was a primary reason why the existence of WGMs has never been considered in these structures. This will be discussed in the following sections.

Some recent spectroscopic studies performed by Prof. Vasily Astratov and his collaborators at the University of Sheffield, UK, indicated that WGMs do exist in semiconductor micropillars despite the weak optical confinement in the vertical direction. This experimental observation required more theoretical insight into the mechanisms of formation of these modes in micropillars, and that was the primary objective of the work presented in this chapter.

In this chapter we will first consider the basic cavity quantum electrodynamic (CQED) experiments and different types of cavities. Then we will consider the experimental results indicating the presence of WGMs in micropillars. After that we will turn to the techniques and results of numerical modeling of WGMs in micropillars developed in this thesis work.

2.1.1 Cavity quantum electrodynamics (CQED) experiment

2.1.1.1 Background theory

In this section, a brief summary for the strong coupling between the cavity mode and individual quantum dot (QD) is introduced based mainly on the work by Reithmaier [17]. When the optical microcavity that has high Q-factor has a single atom inside, the weak coupling and the strong coupling states can be accomplished depending on the strength of their interaction.

The two coupled states are identified depending on the coupling strength between the material oscillator and the optical cavity mode. In the weak coupling regime, the spontaneous emission rate from an atom can be enhanced or reduced [17]. This spontaneous emission rate is modified experimentally [17] by temperature tuning with respect to the discrete optical cavity modes. However, the most striking change of emission properties can take place when the strong coupling conditions are satisfied. In this regime the irreversible spontaneous emission of the atom can be changed to a reversible exchange of energy between the atomic oscillator and the optical cavity mode. Due to this strong interaction, photons emitted by the atom located inside the optical cavity mode can be reabsorbed and reemitted, which gives rise to so called Rabi oscillations [4]. However, in order to observe this phenomenon experimentally from the interaction between the atomic emission and optical cavity mode, the individual linewidth of the two resonant states has to be smaller than the splitting between these states occurring due to their coupling.

Such experiments have been performed [26] using semiconductor technology, i.e., the discrete states of the semiconductor QDs. This semiconductor realization of the strong coupling can provide the fundamental building block for solid state quantum computers (qubits) and the optical cavity mode can manipulate the interaction between the qubits.

Light can oscillate inside an optical microcavity and resonate at the resonant energy (E_{cav}) as shown in Figure 2.1(a). The exciton can be excited with the energy (E_{ex}) close to the resonance of the microcavity as shown in Figure 2.1(b). When the exciton interacts with the light inside the microcavity, the strongly coupled states of light and

matter can be produced as shown in Figure 2.1(c). If the exciton-photon interaction becomes larger than the combined atomic dipole decay rate and the cavity mode decay rate, then strong coupling occurs [17]. Then the irreversible spontaneous emission process of the emitter is changed into the reversible energy exchange. This energy exchange between the exciton and the photon can take place in the form of Rabi oscillations for timescales shorter than the inverse cavity mode decay rate [17]. In spectroscopic experiments this energy exchange results in anti-crossings between the atom-like emitter and cavity-mode dispersion relations. It is characterized by the vacuum Rabi splitting or normal mode splitting NMS [17].
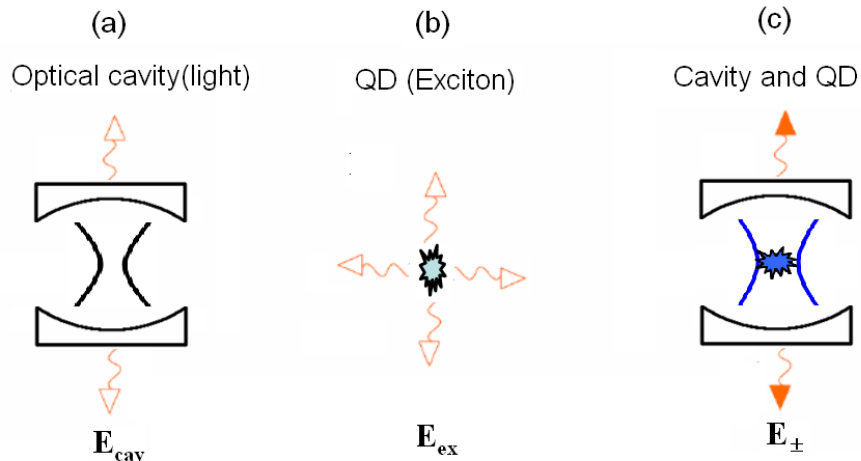
FIGURE 2.1: Light-matter interaction.
(a) Light in a microcavity, (b) Exciton from matter, and (c) Exciton-polaritons from the light-matter interaction.

In solid state implementation by QD semiconductor cavity, the strong and weak interaction can occur between the QD exciton (X) and discretized cavity (C) modes at a resonance ($E_X = E_C = E_0$). In a picture of coupled oscillators the energies of the interacting modes at resonance are [17]

$$E_{\pm} = E_0 - i(\gamma_C + \gamma_X)/4 \pm \left[g^2 - (\gamma_C - \gamma_X)^2/16\right]^{1/2} \qquad (2.1)$$

where $\gamma_{C,X}$ is the full width at half maximum (FWHM) of the cavity and exciton modes, respectively, and g is the exciton-photon coupling parameter. In order to achieve the strong coupling, the last term in Eq. (2.1) should be real, in other words, g^2 must be bigger than $(\gamma_C - \gamma_X)^2/16$, that is, ($g^2 > (\gamma_C - \gamma_X)^2/16$). When this condition is satisfied, the separation between the two resonant energies $E_{\pm}$ is called the vacuum Rabi splitting or NMS. In contrast, if $g^2 \leq (\gamma_C - \gamma_X)^2/16$ the real parts of the energies $E_{\pm}$ are degenerate then there is no noticeable splitting. This regime is called the weak coupling which can be explained by an enhancement of the spontaneous emission on resonance by the Purcell effect [17].

The exciton-photon coupling parameter g is related to the oscillator strength f and the mode volume V by [13]

$$g = (\pi e^2 f)^{1/2}/(4\pi\varepsilon_r\varepsilon_0 m_0 V)^{1/2} \qquad (2.2)$$

where ε_r and ε_0 are the dielectric constants of cavity material and vacuum, respectively, and m_0 is the free electron mass. Eq. (2.2) shows that the exciton-photon coupling parameter g is related to the QD exciton oscillator strength f and the mode volume of the cavity V as $(f/V)^{1/2}$ [17].

In Eq. (2.1) the FWHM of the cavity mode γ_C is related to the quality factor of the cavity $Q = E_C/\gamma_C$ where E_C is the resonant energy of the cavity. In general, the Q-factor of a cavity is determined by the energy loss per cycle versus the energy stored. With no absorption by the cavity material, the Q-factor is determined by the reflection loss at the interface between the interior and exterior of the ideal cavity [3]. Considering the

practical values of γ_C and γ_X in semiconductor microcavities and in quantum dots, γ_C is much bigger than γ_X and the criterion for strong coupling can approximated by $g > \gamma_C / 4$ [17]. Lastly, in order for strong coupling to take place, we can make the approximation,

$$\sqrt{f/V} \cdot Q > E_C / 4 . \tag{2.3}$$

In Eq. (2.3), if f is fixed because it is mainly related to the fabrication parameters of the QDs, the figure of merit for strong coupling is basically

$$F > Q / \sqrt{V} . \tag{2.4}$$

Therefore, in order to overcome the threshold for strong coupling, the figure of merit (F) is required to be as large as possible. The figure of merit can be maximized by increasing the Q-factor and decreasing the mode volume of the optical cavity. These two factors are mostly related to the design of optical microcavity.

2.1.1.2 Anti-crossing example

In this section, one experimental result [17] of the strong coupling between the optical cavity and a single QD will be discussed as an example of the CQED effects. In this experiment, the strong coupling of an individual two-level solid state system with a photon was observed as realized by a single QD in a semiconductor micropillar cavity [17]. The strong coupling manifests itself in florescent (PL) data due to anti-crossings between the QD exciton and cavity mode dispersion relations.

Figure 2.2(a) shows the SEM image of InGaAs QDs that are self-assembled with a characteristic diameter of 15-20 nm. Larger size of the QDs was obtained by reducing the indium content. Such QDs are located in the middle layer of the micropillar cavity that is shown in Figure 2.2(b). This larger size of QDs gives rise to an increase in the

excitonic oscillator strength which can increase the coupling strength. This micropillar was fabricated by a combination of electron-beam lithography (EBL) and reactive dry etching, giving the defect-free sidewalls for high Q cavities (Q = 8,800).
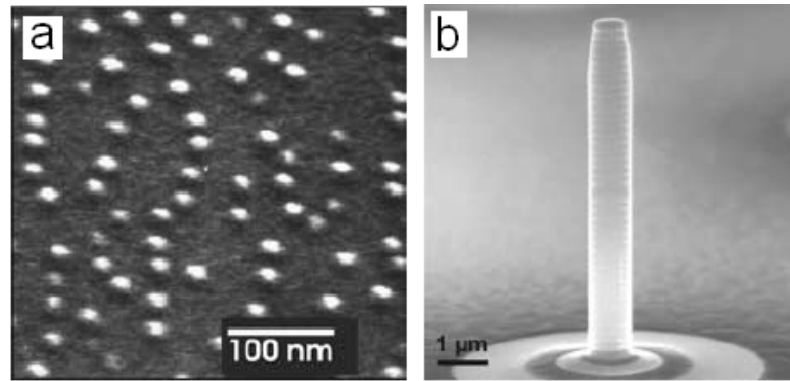
FIGURE 2.2: SEM images of QDs and a micropillar cavity.
(a) Scanning electron micrographs of InGaAs QDs. (b) Scanning electron micrograph of a pillar with a diameter of about 0.8 µm [17].

Figure 2.3 shows the anti-crossing phenomenon observed in a micropillar cavity with diameter of 1.5 μm at different temperatures between 5 and 30K. At temperatures of 5K and 30K, the emission intensity and the linewidth of the dot exciton are smaller than those of the cavity mode. It is clearly seen that the emission peak of the exciton at 5K, which has a slightly higher energy (1.32365 eV) than the cavity mode centered at about 1.32335 eV, shifted to the lower energy as the temperature is increased up to 30K. In addition, in the middle of the temperature tuning process at around 21K, the intensities and the linewidths of the two resonant peaks are quite similar. At this stage, the two peaks are mixed up with the exciton emission and the cavity mode.

These results show that the larger QD gives rise to better oscillator strength. Also, in order to observe the strong coupling, the linewidth of the cavity mode should be smaller. Therefore considering the Eq. 2.4 for the figure-of-merit, it is highly necessary to

increase the Q-factors and to decrease the modal volumes of the microcavities in order to achieve strong light-matter coupling regime.
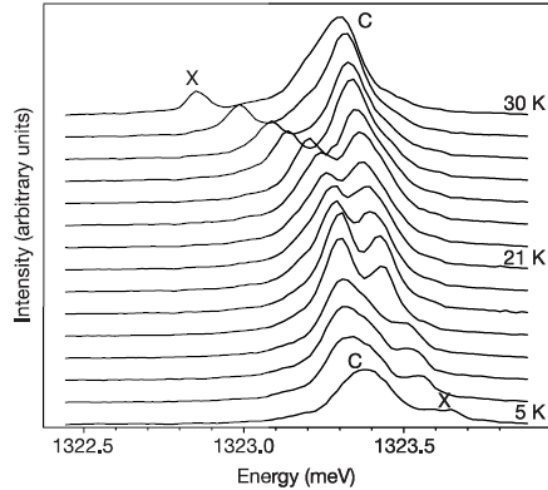
FIGURE 2.3: Temperature dependence of PL spectra.
An anti-crossing is observed owing to strong coupling between the QD exciton and the microcavity photon mode [17].

2.1.2 Microresonator cavities

In this section, three different kinds of optical microcavities [4, 17, 26] are briefly introduced which can be used for achieving the strong coupling between the optical microcavity and the QDs. These microcavities play an important role in these experiments where high Q-factor and small mode volume are necessary. There are two types of optical resonant modes in these microcavities depending on the ways of confining the light inside the cavity, which are the WGMs and the photonic dot states.

The WGMs are the 3D confined optical mode rotating in a circular shaped microcavity. The EM field propagates along the circumference of the circular geometry making the ring-like patterns that fit close to the surface of the cavity. Whereas the photonic dot states are not circularly propagating and they are confined by the structures

using a periodic modulation of the refractive index. Compared to the ring-like mode profile of WGMs, the EM fields of the photonic dot states are concentrated in the center of the cavity. However, in both cases the light traveling inside the resonator should be confined in three spatial dimensions (3D) by means of the TIR and/or the Bragg reflection mirrors. Examples of such cavities are considered in the next section.

2.1.2.1 Microdisk cavity

One of the well-known examples of the microcavities is represented by the microring or microdisk resonators [25, 26] as shown in Figure 2.4. The SEM image of a microdisk cavity which is fabricated [26] by the undercut etching is shown in Figure 2.4(a). The microdisk is elevated above the substrate layer by the supporting pole high enough so that the optical mode is not perturbed by either the substrate. The microdisk resonators support the WGMs by TIR due to the index difference with the background medium. Figure 2.4(b) shows the schematic diagram of a microdisk resonator and its EM amplitude mode profile.

The refractive index of the microdisk, n_1, is surrounded by the lower index of air, n_2, as shown on top of Figure 2.4(b). Since n_1 is bigger than n_2, the light inside the microdisk can be reflected continuously along the circular surface as shown in top view of Figure 2.4(b). An example of the amplitude mode profile of the microdisk is shown in the bottom of Figure 2.4(b) shown as a top view. It is clearly seen that the peaks of the EM field amplitude mode map locate very close to the surface of the disk. The vertical thickness of the disk is typically small enough to allow only the first order which is the fundamental mode and the number of maxima gives the angular mode number.
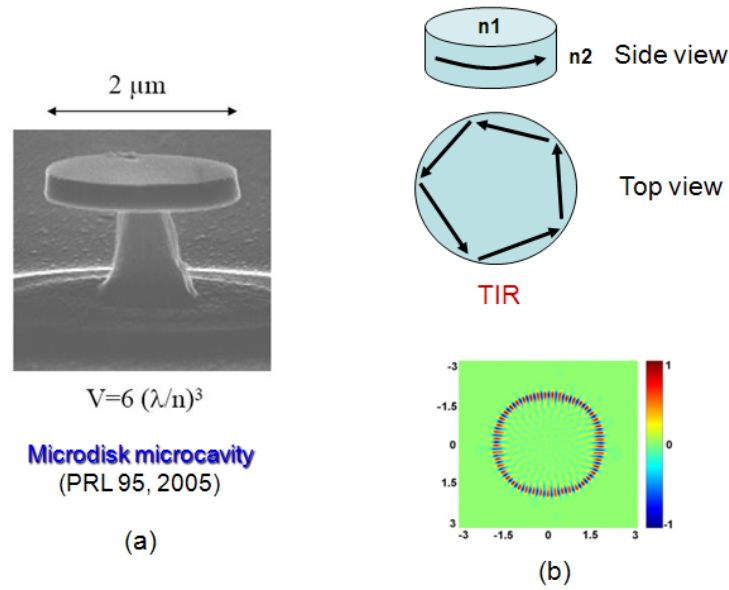
FIGURE 2.4: Microdisk cavity.
(a) SEM image of microdisk cavity [26], (b) Schematic diagram of microdisk cavity and its amplitude mode profile from FDTD calculation for radius of 1.5 μm.

2.1.2.2 Photonic crystal cavity

Other types of microcavities include the photonic crystal cavities [1-8]. The SEM image of a fabricated 2D photonic crystal cavity and computed optical field magnitude of the cavity mode [4] are shown in Figure 2.5(a) and (b), respectively. In this cavity, the in-plane confinement is obtained by fabricating a 2D photonic crystal lattice slab with three holes missing to form a defect where the mode is located [4]. These 2D periodic structures confine the EM field in lateral dimension which acts very similarly to the Bragg layers in the micropillar. The vertical confinement, achieved by TIR at the slab semiconductor-air interfaces, is imperfect, due to the fact that light with small in-plane wavevectors can leak out of the top and bottom [4].

In Fig 2.5(b) the computed field strength as a function of position shows that most of the field energy is confined in the defect region with a mode volume of about 0.04 μm^3. The Q-factor of the photonic crystal nanocavities can reach up to Q = 800,000 [132].

However, in order to have this high Q-factor and small mode volume in photonic crystal cavities, a fine-tuning of the positions of air rods at the cavity edges is necessary [3] to reduce the radiation loss due to weak vertical confinement.
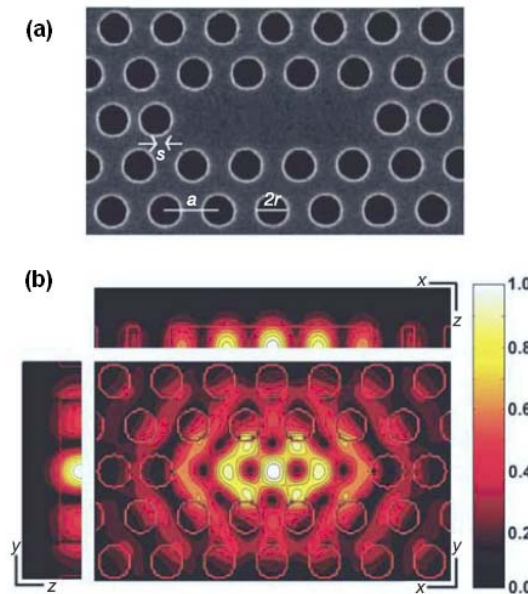
FIGURE 2.5: Photonic crystal microcavity.
    (a) SEM image of a fabricated photonic crystal cavity, (b) Computed optical field magnitude of the cavity mode [4].

2.1.2.3 Micropillar cavity

Another interesting microresonator structure is the micropillar cavity [17] that supports the photonic dot states. Usually the photonic states in such cavities are optically probed along the vertical direction. Fig 2.6(a) shows the micropillars with circular cross-section that have been processed by electron-beam lithography and reactive ion-etching in inductively coupled Ar/Cl$_2$ plasma [17]. Pillars with 2 μm diameter result in Q-factors of about 9.000 with optimized micropillar processing. Numerical calculations show the mode volumes of about 0.3 μm^3 for the 1.5 μm diameter micropillar [17].
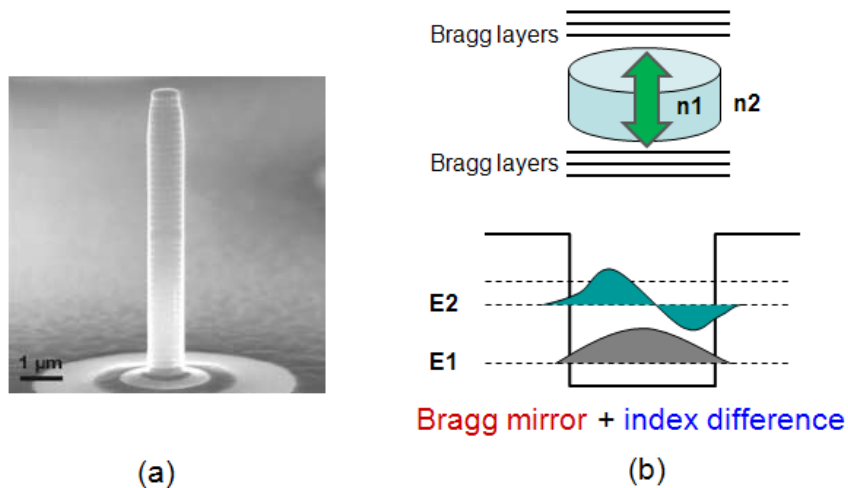
FIGURE 2.6: Micropillar cavity.
(a) SEM image of a micropillar cavity [17], (b) Schematic diagram of the cavity and its mode profiles.

The Bragg mirrors on top and bottom between the middle layer confines the light in vertical direction and creates the resonant cavity structure where the light oscillates along the axis of the pillar as shown on top of Figure 2.6(b). On the other hand, the lateral confinement is accomplished by the TIR along the lateral surface of the pillar. The lateral profile of the photonic dot states of the micropillar shown on bottom of Figure 2.6(b) indicates that most of the energy of the mode is concentrated in the center region of the cavity. Therefore, the sidewall surface roughness in the micropillar cavities doesn't contribute as much to the Q-factor as the performance of the vertical confinement by the Bragg layers.

Until recently, only photonic dot states were observed in micropillar cavities. However, the micropillar can be viewed as a microdisk that has Bragg layers on top and bottom. Thus, it is possible to suggest that this structure can support two resonant modes, photonic dot states and WGMs. The Bragg layers loosen the confinement in the vertical direction for the WGMs in micropillars compared to the microdisk cavities. In addition,

the sidewall surface roughness plays more important role in having larger Q-factors of WGMs compared to the photonic dot states in micropillar cavities. This is because most of the energy of the WGMs is located very close to the sidewall surface. Therefore, an investigation to WGMs in the mcropillar cavities is necessary in order to estimate full potential of these cavities for developing CQED applications in comparison with other resonant modes in different cavity structures.

2.2 Experimental observation of WGMs in semiconductor micropillar resonators

The study of WGMs in micropillar resonators is quite interesting due to the unusual combination of optical confinement. On one hand they are similar to microdisks [23-31] because of their circular symmetry. On the other hand the vertical confinement is due to Bragg reflection which is very different from microdisks. This work shows that due to higher Q-factors and smaller modal volumes of WGMs in pillars, they have better potential for observation of strong coupling with individual QDs according to the figure-of-merit: $Q / \sqrt{V}$. As it was mentioned earlier in section 1.1 this problem is based on the experimental results obtained in Sheffield, so below we consider the experimental configuration used in these measurements and present major experimental observations.

2.2.1 Experiment geometry

The microcavity structure used in this work consists of 27 pairs of alternating $Al_{0.8}Ga_{0.2}As/GaAs$ layers in the bottom distributed Bragg reflector and 20 repeats on top. The one-wavelength cavity contains one layer of InAs QDs of density $\sim 5 \times 10^{9}$ μm^{-2} positioned at the anti-node of the optical field which is very close to the circular surface of the structure as shown in Figure 2.7. The samples were processed into 1-10 μm diameter pillars using a combination of electron beam lithography (EBL) and inductively

coupled plasma etching at the All-UK III-V Growth and Fabrication Facilities at the University of Sheffield, U.K. The studies of photonic dot states in such micropillars have been performed [13, 121, 122] at the Low Dimensional Structures and Devices (LDSD) at the Department of Physics and Astronomy along with other groups [11, 15]. The studies of WGMs in micropillars were initiated by Dr. Vasily Astratov during his visit to the University of Sheffield in April-July 2006.

The photonic dot states are confined by the two distributed Bragg layers. The photonic dot states are measured from the vertical direction which is the resonant direction of cavity due to the reflections provided by the two Bragg reflectors. A laser light (black arrow) was focused at the top of each pillar and the spectral response (blue arrow) was obtained from the top too.

During his visit to Sheffield, Dr. Vasily Astratov suggested the possibility of the existence of the WGMs in the micropillar structures. In this case, the WGMs are confined by the dielectric interface along the circumference of the GaAs (index 3.54) layer due to the TIR between the GaAs and the air. The vertical confinement of the WGMs is accomplished by the Bragg reflection layers. Since the WGMs are propagating along the circumference of the middle layer, the spectral response from the scattering of the WGMs may be detected in the plane of the central cavity between two Bragg mirrors. Therefore the laser beam (black) was focused at the middle layer of the pillar and the WGMs (red) were detected from the same layer in the direction perpendicular to the pillar axis as shown in Figure 2.7.
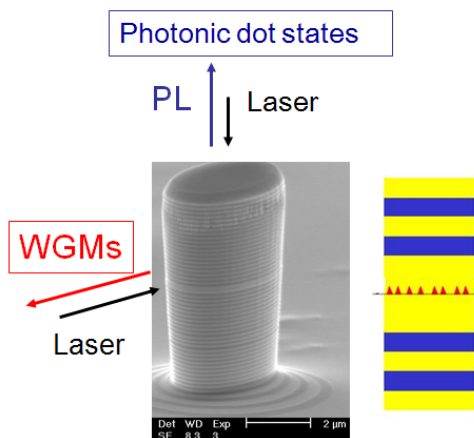
FIGURE 2.7: SEM image of a micropillar with diameter of 4 μm [11, 133, 134].
Photonic dots are measured from vertical direction and WGMs from horizontal direction. QDs lie in the middle layer (Schematic diagram on right).

In order to measure the WGMs in this plane, it was important to find a way to open an optical access to the side wall of the micropillars. This was achieved by cleaving the substrate as shown in Figure 2.8. A laser light (black arrow) was focused onto the side wall of the pillars and the photoluminescence (PL, red arrow) of the WGMs was measured from side wall in the direction perpendicular to the pillars.
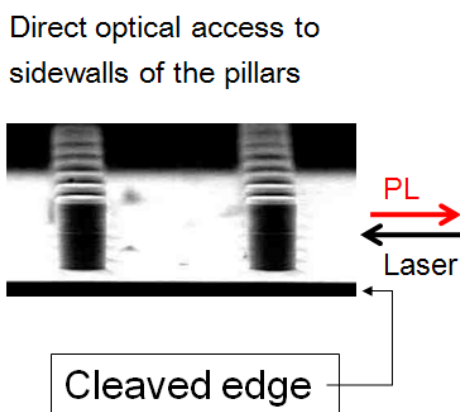
FIGURE 2.8: SEM images of circular micropillars with diameter of 5.4 μm [11].

2.2.2 Experimental Results

The photoluminescence spectra from 5.4 μm pillars are shown in Figure 2.9. The spectral response of photonic dot states were obtained with excitation and collection of PL emission perpendicular to the Bragg mirrors, as illustrated by the blue spectrum in Figure 2.9. The PL from the InAs QDs was excited through the top mirror at 633 nm in a micro-PL setup with a ~1 μm laser spot size. The experiments were performed at 10 K. Under the high power conditions (~1mW) used in their experiments they excite an inhomogeneously broadened QD emission band in the 1.2-1.4 eV range. The coupling of this emission to 3D size quantized photonic dot states gives rise to peaks in the 1.27-1.30 eV range.

To study circular cavity modes in the perpendicular direction the structure was cleaved to enable optical access to the sidewalls of the pillars as illustrated in the Figure 2.8. The distance between the pillars and the cleaved edge of structure was in the 1-5 μm range. The sample was rotated in the cryostat by 90^0 to provide the excitation and collection of light at normal to the sidewall surfaces of the pillars. In this geometry a series of nearly equidistant peaks over a broad range of energies, the characteristic fingerprint of WGMs, was observed [11, 133, 134] as illustrated by the red spectrum in Figure 2.9. The intensity of these peaks was found to be a maximum when the excitation laser was focused on the central section of the pillars, thus indicating that the WGMs are localized in the central cavity region.
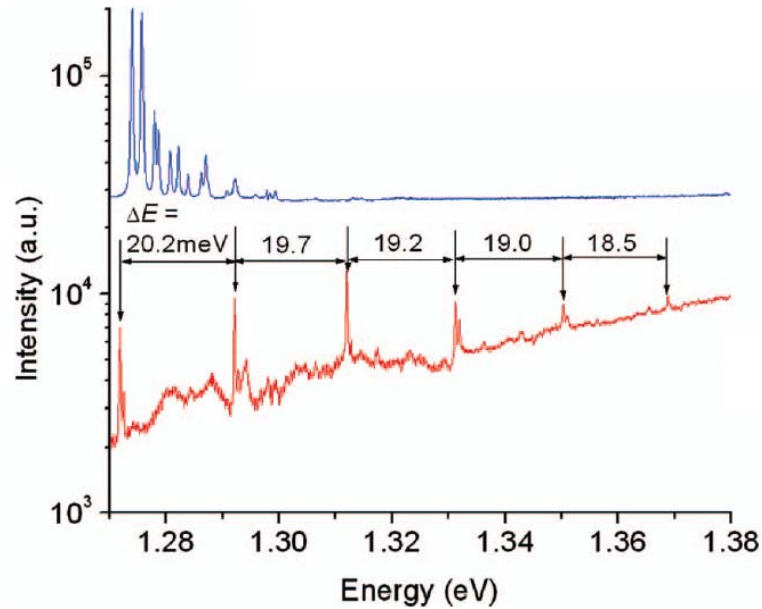
FIGURE 2.9: Emission spectra of 5.4 μm circular pillar.
The spectra were detected from the top mirror (blue), from the sidewall surface (red) with the WGM mode spacing ΔE indicated [11, 133, 134].

The separation between the peaks was found to be converging with increasing energy (typically by ~8 % in the 1.27-1.37 eV range). The separations (ΔE) measured in the low energy side of spectra (~1.28 eV) were found to be inversely proportional to the diameter of the pillars as illustrated in Figure 2.10. The Q-factors of the WGMs were found to approach 20000 for 4-5 μm pillars, well in excess of Q~10000 for the photonic dot states in the same pillar represented by the blue spectrum in Figure 2.9.

Similar WGM peaks were detected from the sidewalls of pillars with elliptical cross section for 2.6 x 1.6 μm^2 pillars. The Q-factors of the WGMs were found to be reduced in such small pillars down to Q~6000 but were still higher than that for photonic dot states (Q~4000) [15] measured from the same pillars.
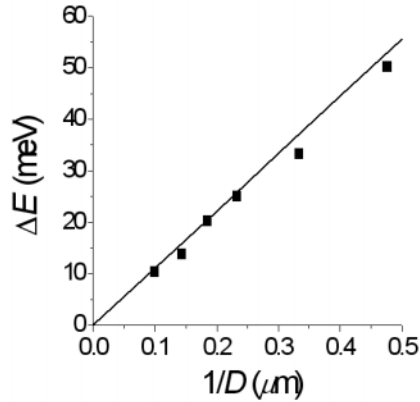
FIGURE 2.10: ΔE versus $1/D$ where D is the pillar diameter (squares).
The straight line represents a theoretical fit obtained with $n = 3.54$ [11, 133, 134].

An estimate of the separation between cylindrical WGM peaks with the same polarization can be obtained under the assumption that inside the cavity the photons follow a circle of radius R: $\Delta E \approx \hbar c_0 /(R n_{eff})$, where n_{eff} is the effective refractive index. This formula provides a good fit to the measured dependence of peak separation with pillar size using $n_{eff} = 3.54$, as illustrated by the straight line in Figure 2.10. This model, however, is a too rough approximation to provide correct WGM mode numbers and to explain more detailed effects such as convergence of the peak separations with energy.

2.3 Numerical modeling of WGMs in semiconductor micropillars

The experimental spectral peaks of WGMs in micropillar cavities show better Q-factors compared to the photonic dot states in the same structure. However, a theoretical investigation of these experimental results is necessary not only to understand the properties of the WGMs in the pillars but also to apply them properly to the CQED experiments. In the experiments, the WGMs are observed in the pillars with elliptical cross section with 2.6 x 1.6 μm^2 that have even smaller radius of curvature at the ends of the major axis. These measured Q-factors for the WGMs may be increased close to the

theoretical limit of the structure by improving the quality of the sidewall surface using different etching processes. In addition, the experimental results show the relatively strong convergence trend of the peak separations with energy for all the pillars with different sizes.

Another important goal for such theoretical modeling is connected with evaluation of the prospect of using of WGMs in micropillars for the possible CQED experiments. This analysis can be performed by studies of the photonic figure-of-merit discussed in Section 2.1.1.1. for various types of modes in different cavities. In the next section we will introduce the numerical modeling methods and the results of modeling compared with the experimental spectra. Finally, the calculated mode volumes for those cavities will be presented.

2.3.1 Simulation methods

In order to obtain a more accurate description of the WGM resonances in micropillars, numerical modeling of the EM field distribution based on 3D finite difference time domain (FDTD) simulations using the FullWAVE^{TM} software [135] was performed. There are three factors that contribute to increasing the computational time for this type of modeling. First, such 3D FDTD simulations require much longer time compared to 2D simulation due to the big increase of the calculation area. Secondly, the micropillar cavities have 27 and 20 pairs of GaAs/AlGaAs layers which form the bottom and top Bragg layers, respectively. They are used for the vertical confinement of the "photonic dot" states. The role of these mirrors for WGMs was not clear before beginning this computational work. However modeling these mirrors in 3D case was not realistically possible since they significantly increase the computational area. Finally,

spectral response of the cavity requires very long time of calculation in the time domain in order to obtain reliable spectra especially for high Q resonators.

2.3.1.1 Averaged index material for Bragg layers

The 3D calculations for micropillars are found to be so time consuming that the numerical modeling for a full experimental structure including multi layer Bragg mirrors was not realistically possible for us. One factor allowed us to simplify the structure significantly. Due to large in-plane k-vectors WGMs in the central cavity are effectively confined in the central cavity due to TIR. Under these conditions their penetration into the Bragg mirrors is due to the evanescent field. These modes are not propagating perpendicular to the mirrors, and for this reason they are not a subject for the Bragg reflectivity. The penetration depth in the mirrors corresponds to only 2-3 layers of the mirrors, which reduced the number of Bragg layers from more than 20 down to three layers for both sides.

In addition to this requirement of long calculation time, which even though reduced dramatically by reducing the number of Bragg layers, it is not easy to implement each Bragg layer in the software due to their small height with respect to the size of the grid (or mesh) used in the calculations. For example, the alternating Bragg layer consists of a pair of GaAs/AlGaAs that have thickness of 69.3 nm and 78 nm, respectively. Figure 2.11 shows the vertical index profile at x=-0.13 μm for different step sizes. In the cases of step sizes $\lambda/16$ and $\lambda/50$ for Figure 2.11(a) and (b), respectively, the index profile does not represent the index of the real structure. Only when the step size is close to $\lambda/100$ does the index profile properly represent the real structure. Therefore, the size of the unit cell, i.e., Yee cell [136] should be smaller than 1/100 times the operating wavelength

resulting in ~9 nm which is too small to implement in our current PC. The calculation volume of the 4.1 μm pillar that has two pairs of Bragg layers on both sides is 5.4 × 1.4 × 5.4 μm^3. The approximate amount of memory for a simulation is [137]

$$\text{Approximate amount of memory} = Nx\ Ny\ Nz\ [(6{\times}8){+}8] \qquad (2.5)$$

where *Nx, Ny,* and *Nz* are the array dimensions in each direction. Eq. (2.5) assumes that the six field components and permittivity are stored as double precision floating point values requiring 8 bytes of memory each. Using the maximum step size of ~9 nm and the computation area of 5.4×1.4×5.4 μm^3, the approximate amount of memory for a simulation is larger than 3 Gb. The actual required memory size should be greater than 3 Gb since it does not take into consideration storage of variables for boundary conditions and the input field. This memory size is not currently available for the lab PC.
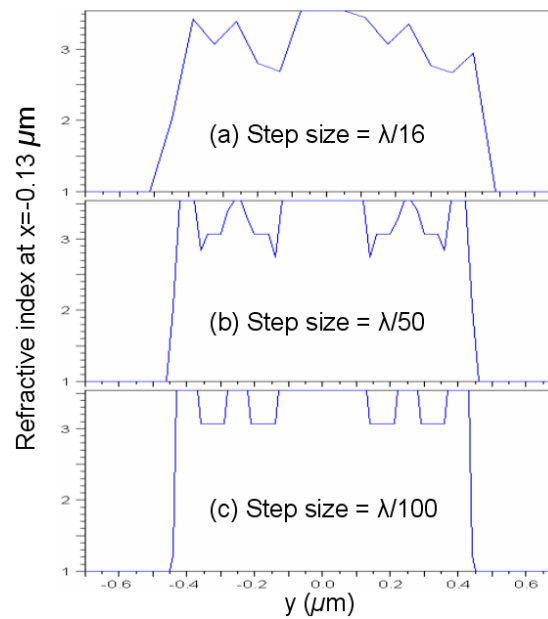
FIGURE 2.11: Vertical cut of index profile.
The index profiles are obtained at x=-0.13 μm for different step size of (a) λ/16, (b) λ/50, and (c) λ/100.

In addition, the time step should be very small with small grid size of $\lambda/100$. The stability condition relating the spatial Δt and temporal step size Δx, Δy, and Δz is [135]

$$C\Delta t = \left[\frac{1}{\Delta x^2} + \frac{1}{\Delta y^2} + \frac{1}{\Delta z^2} \right]^{-1/2} \qquad (2.6)$$

where C is the maximum velocity of the wave. Eq. (2.6) shows that the maximum time step satisfying the stability condition for the grid size of $\lambda/100$ is about 1.73×10^{-17} sec which makes the wave propagation very slow. Therefore, based on the memory size and the time step for the simulation, implementing the real quarter-wavelength thickness of Bragg layer is not practical because the calculation time required for such modeling is too expensive.

One way of overcoming this problem is to simplify the structure so that the software can take into account only essential physical properties of the structure. Therefore we approximated the multiple Bragg reflection layers with the simple averaged index material. Figure 2.12(a) shows the half cross-section image of a micropillar with radius of 2μm and ten alternating Bragg reflection layers on both sides. The index of the cavity is sufficiently large for confining the modes in vertical direction. However this confinement is much weaker than in microdisks. As a result, the evanescent field of these modes penetrates deeply into the Bragg mirrors, so that the evanescent field in 2-3 layers of the mirrors experiences their average index.

Due to the deep penetration of evanescent field in the Bragg mirrors we made an assumption [11, 133, 134] that this structure can be modeled using an effective index approximation for Bragg mirrors. Therefore we can further simplify the reduced number of the Bragg reflection layers with the single averaged index media shown in Figure

2.12(b). We modeled the GaAs cavity as a disk (index 3.54) with 0.27μm

thickness surrounded on both sides with disks of effective index 3.31 that correspond to

the Bragg reflection layers with a pair of alternating GaAs/AlGaAs layers (index 3.54 and

3.07, respectively). Figure 2.12(c) shows the reflection index profile with the vertical

dimension of the pillar. We limit the height of the averaged index layer adjacent to the

cavity to 0.4 μm.
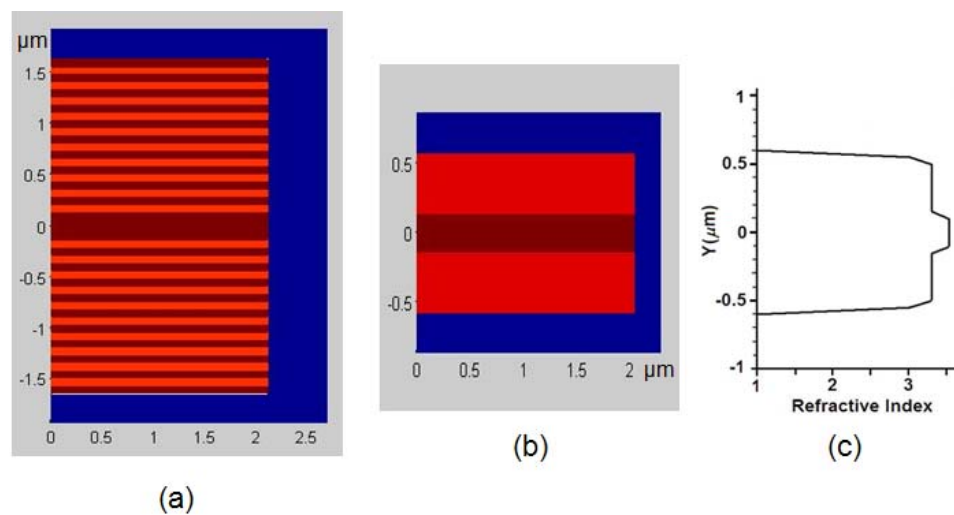
FIGURE 2.12: Averaged index approximation of Bragg layers [11].
(a) Half cross-section image of a micropillar with 10 pairs of alternating layers for top and bottom. (b) Image of simplified structure by averaged index approximation for 3 pairs of Bragg layers for both sides. (c) Refractive index profile with vertical direction.

Finally, with all the approximations above, the spatial step size was reduced to

λ/16 which results in 0.116 ns in temporal step size. The running time for this structure

usually takes about 2-3 days with the PC.

2.3.1.2 Implementation of the source and detector

In order to excite the WGMs inside the micropillars, the built-in source with

Gaussian plane wave launched a pulse with pulse duration of 3.3 fs very close to the

circumference of the cavity. Figure 2.13 shows the top view of the geometry of 5.1 μm micropillar. The dimensions and the locations of the source and the monitor are summarized in Table 2.1.
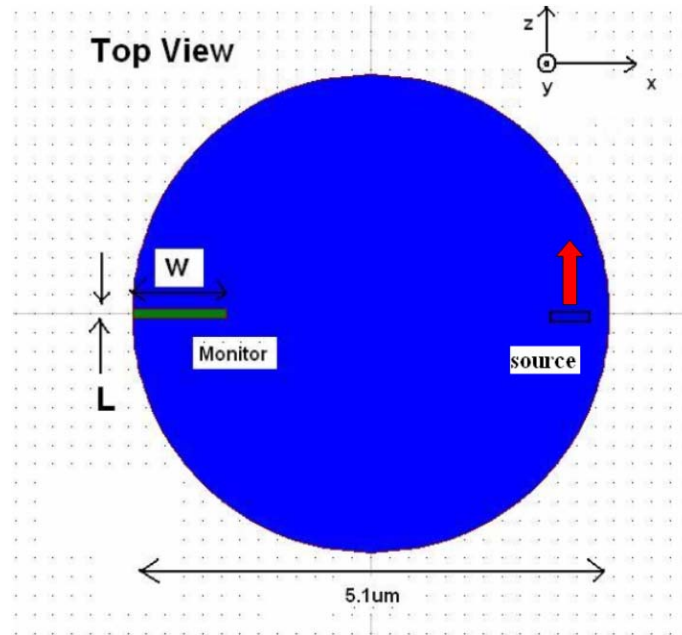
FIGURE 2.13: Source and detector dimensions and locations for 5.1 μm pillar.

Table 2.1: Simulation parameters for monitor and source

Sphere size	Monitor (μm)	Source (μm)
5.1 μm circular	Size: W=1, L=0.1, H=0.27 Position: x=-2.05, y=z=0	Size: W=0.27, H=0.27, L=0 Position: x=2.38, y=z=0
4.1 μm circular	Size: W=0.6, L=0.1, H=0.27 Position: x=-1.75, y=z=0	Size: W=0.27, L=0.27, H=0 Position: x=1.88, y=z=0
2.6x1.6 μm elliptical	Size: W=0.2, L=0.05, H=0.27 Position: x=-0.7, y=z=0	Size: W=0.27, L=0.27, H=0.27 Position: x=0.6, y=z=0

Figure 2.14(a) shows the geometry for the FDTD simulation where d is the cavity thickness of 0.27μm and R is the radius of the pillar of 2 μm. The dotted square shows the built-in source in the pillar. The red arrows show the direction of the propagation of

the launching plane wave. The size of the launching Gaussian pulse was 0.5×0.5 μm^2 in x-y plane.
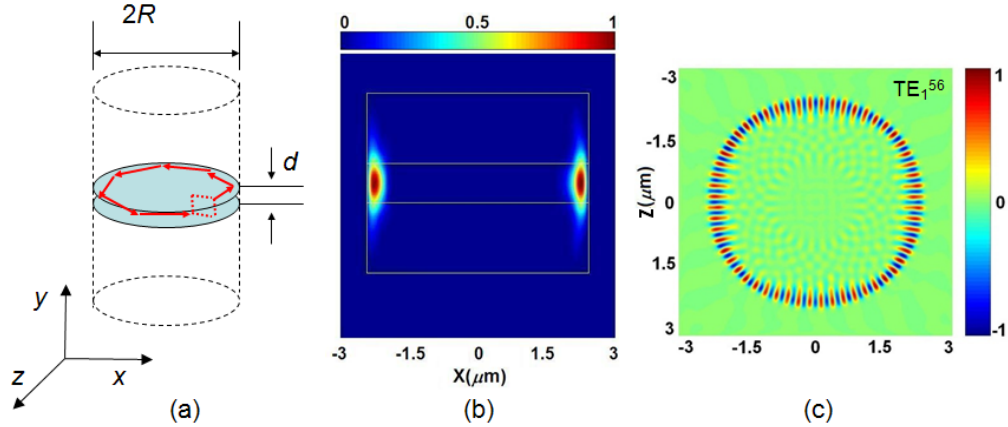
FIGURE 2.14: FDTD simulation mode profiles [11].
(a) Geometry for the FDTD simulation with launching source. (b) Amplitude mode profile in x-y plane. (c) Amplitude mode profile in x-z plane for TE_{56}^1.

The short pulses with pulse duration of 3.3 fs that is sufficient for excitation of multiple WGM peaks centered at 0.94 μm wavelength. A Transverse electric (TE) polarized source was used to generate a comb of TE_l^n WGMs with radial number n=1 and various angular l numbers. Figure 2.14(b) shows the amplitude mode profile in x-y plane of the WGMs. This amplitude profile shows that the thickness of 0.4μm of layers adjacent to the central cavity is sufficient to approximate the mode profile along the y-axis in the entire pillar. One of the resonant mode profiles in the x-z plane for TE_{56}^1 is shown in Figure 2.14(c). The spectral response from a short pulse excitation was obtained by the Frequency Monitor of the software in the FDTD output option. Once the spectral response was obtained, the excitation changed into continuous wave (CW) that had a single frequency of one of the WGM peaks.

2.3.2 Calculated WGM spectra and their comparison with the experiment

The bottom black curve in Figure 2.15 shows the spectral response of the WGMs calculated for the 5.3 μm pillar which has a slightly smaller size compared to that in the experimental structure. In order to obtain the best spectrum fit, the diameter of the micropillar was used as a fitting parameter. It shows that the calculated spectrum for the 5.3 μm pillar fits very well the experimental one for the 5.4 μm micropillar. The small difference in the size between the experimental and the calculated spectra can be explained by the fact that in real AlGaAs structure the near surface layer is always oxidized. From the SEM image, the pillar sidewall reveals the presence of a 90 nm thick oxide skin which is probably formed during the plasma-assisted etching [138]. The index of the oxide is expected to be around 1.5. In terms of modeling this means that the effective size of micropillars is expected to be less than their physical dimensions determined by SEM characterization. The use of slightly smaller sizes in modeling is reasonable for this structure. The small difference of ~100-200 nm is generally consistent with thickness of so-called "oxide skin" in AlGaAs structures [11].

It should be noted that the calculations predict a weak (2–4 %) converging trend of the WGM peak separations with energy in the range between 1.27 and 1.37 eV for 5.4 μm pillars as shown in Figure 2.16. This convergence arises from the slight increase of the effective WGM radius with l. The stronger converging trend observed in the experimental spectra (~8%) may arise from dispersion effects in the GaAs cavity combined with additional dispersion introduced by QDs absorption with increasing energy. Small convergence (0.2 meV) between the third and forth FSR compared to 0.5 meV for other peaks might come from the experimental error.
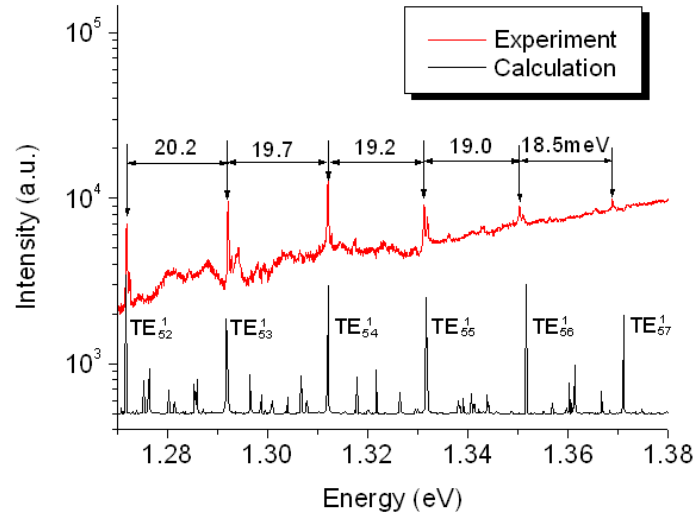
FIGURE 2.15: WGM spectra from experiment and calculation 5.4 μm circular pillar. Calculated (black) emission spectrum fits the experimental (red) results [11, 133, 134].
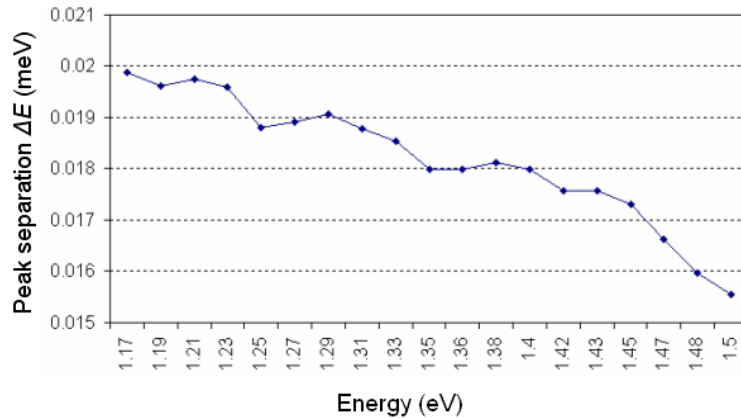
FIGURE 2.16: Convergence of the peak separation ΔE for 5.4 μm circular pillar.

Examples of such spectra calculated for 4.1 μm circular and for 2.6 × 1.6 μm elliptical pillars are presented (black) in Figure 2.17 and Figure 2.18, respectively. Figure 17(a) and Figure 2.18(a) illustrate the SEM image of the two micropillar structures with the laser excitation (black) and the PL detection (red). For the elliptical pillars, the excitation and the detection were oriented along the major axis of the ellipse.
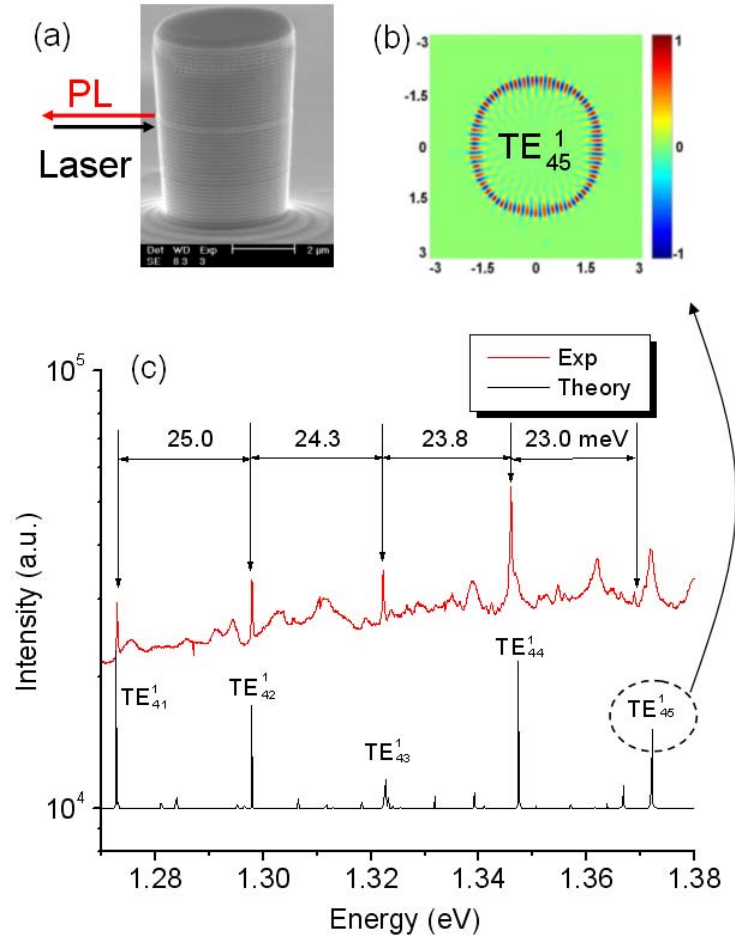
FIGURE 2.17: WGM spectra from experiment and calculation 4.3 μm circular pillar. (a) SEM image of 4.3 μm circular pillar, (b) amplitude mode profile of WGMs in x-z plane for TE_{45}^1, (c) emission spectrum of experimental sidewall PL (red) and of WGMs peaks (black) calculated for 4.1 μm pillars [11, 133, 134].

An EM amplitude map for the TE_{45}^1 WGM peak of Figure 2.17 (c) at 1.373 eV is presented in Figure 2.17 (b), and a similarly obtained map for the TE_{21}^1 peak of Figure 2.18 (c) at 1.316 eV is presented in Figure 2.18 (b). The calculated WGM peak positions for circular pillars and elliptical pillars agree well with the experimental peak positions in Figure 2.17(c) and Figure 2.18(c), respectively.
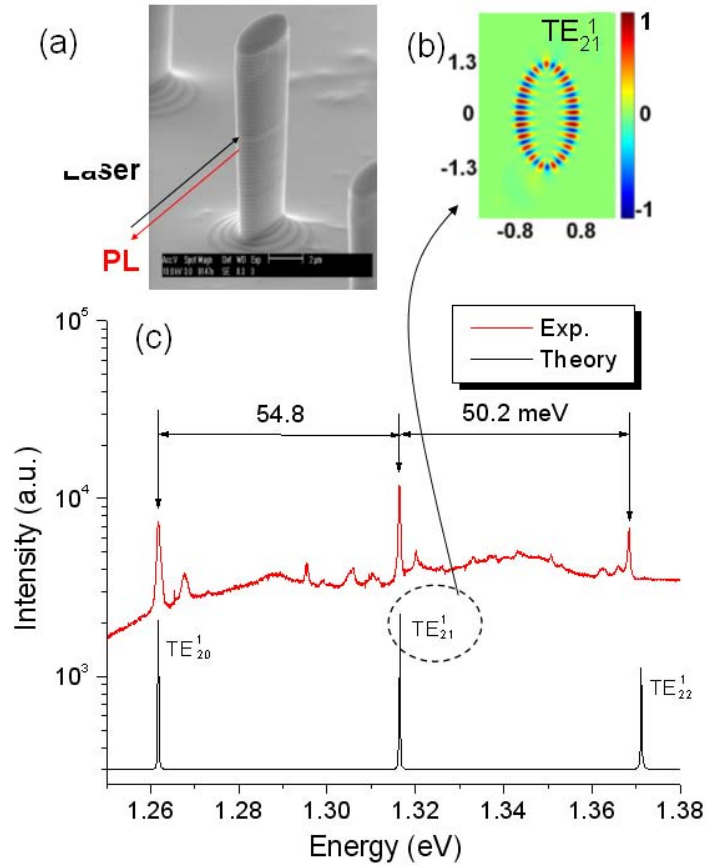
FIGURE 2.18: WGM spectra from a 2.6x1.6 μm elliptical pillar.
(a) SEM image of the structure, (b) amplitude mode profile in x-z plane for TE_{21}^1, and (c) fitting of spectra between experiment (red) and FDTD calculation (black) results. The excitation and detection were performed along the major axis [11, 133, 134].

The slightly smaller pillar diameter (4.1 μm) was employed in the simulations to give the best fits to the experimental data compared to the 4.3 μm sizes determined by SEM characterization for circular pillars in Figure 2.17. This may also arise from the presence of an oxide skin with smaller index at the sidewall surface of the AlGaAs layers as in the case of 5.4 μm pillars. It also shows that the calculations reproduced the converging trend of the WGM peak separations in the experimental spectra in the energy range between 1.27-1.37 eV reasonably well for 4.3 μm pillars.

2.3.3 Q-factor and mode volume calculation

One important parameter for the CQED experiment along with Q-factor for the optical cavity is the mode volume. The mode volume can be calculated only by the calculation of the EM field in the cavity. The cavity mode volume is calculated according to the formula [139]:

$$V = \frac{\int_{V_q} \varepsilon(\vec{r})|\vec{E}(\vec{r})|^2 d^3\vec{r}}{\max\left[\varepsilon(\vec{r})|\vec{E}(\vec{r})|^2\right]} \tag{2.5}$$

where $\varepsilon(\vec{r})$ is the dielectric constant, $|\vec{E}(\vec{r})|$ is the electric field strength, and Vq is a quantization volume encompassing the resonator and with a boundary in the radiation zone of the cavity mode under study. It turned out that the numerator of Eq. (2.5) can be calculated using an option developed by RSoft. So, we calculated the energy density in the Fullwave^{TM} RSoft which is defined as
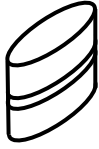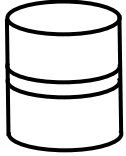
$$E_d = \int \varepsilon(r)E^2(r)d^3r. \tag{2.6}$$

The denominator of Eq. (2.5) ($\max[\varepsilon(r)E^2(r)]$) was determined from the field distribution at the end of the simulation. We analyzed field distributions in different cross-sections using RSoft in order to find this maximum. This approach works equally well for circular and elliptical pillars.

By using this method, we made Table 2.1 to summarize the mode volumes for three structures, elliptical pillar (diameter: 2.6 μm × 1.6 μm), elliptical disk (diameter: 2.6 μm × 1.6 μm), and circular pillar (diameter: 4.1 μm). In order to improve the accuracy of mode volume for circular pillar (4.1 μm) we increased the calculation time more than three times compared to the previous results and reduced the cell size of FDTD from

(1/20)λ to (1/25)λ. In addition, in order to make the spectrum of the source narrower we terminated the Gaussian pulse of the source at longer time and in more symmetric way. This reduces generation of higher frequencies that may excite higher order cavity modes. Under these improved conditions, the mode volume for circular pillar turned out to be little smaller value (V=0.26 μm^3) than the previous one (V=0.3 μm^3).

TABLE 2.2: Mode volume and Q-factors for three different structures (λ=0.94 μm)

Structures	Elliptical pillar (2.6 × 1.6 μm^2) (height: 1.07μm)	Elliptical disk (2.6 × 1.6 μm^2) (height: 0.27μm)	Circular pillar (4.1 μm) (height: 1.07μm)
Mode volume(μm^3)	0.17	0.08	0.26
Quality factor	6300		
Schematic Diagram	$n_{core} = 3.54$ $n_{clad} = 3.31$	$n_{core} = 3.54$ $n_{clad} = 1.0$	$n_{core} = 3.54$ $n_{clad} = 3.31$

The mode volume for the elliptical disk 2.6 μm × 1.6 μm was calculated to compare with the one from the paper by E. Peter et al. [26]. The elliptic disk which has similar circumference to the circular disk with diameter of 2 μm shows the mode volume of 0.08 μm^3 comparable to 0.07 μm^3 from E. Peter's paper. Considering the wavelength difference between E. Peter's paper (0.74 μm) and our case (0.94 μm), calculation results actually showed even smaller mode volume. The elliptical pillar 2.6 μm × 1.6 μm was found to have the mode volume of 0.17 μm^3 which is twice bigger than that for the elliptical disk with the same size. The difference can be explained by weaker optical

confinement in vertical direction due to smaller refractive index 3.54/3.31. For circular pillar with diameter of 4.1 μm we found mode volume of 0.26 μm^3.

By measuring the linewidth of the peaks from the calculated spectrum Q-factors of WGMs can be obtained. We could calculate the Q-factor for the elliptic pillar only with small running time due to large loss. The Q-factor is 6300 which is close to the result from the experimental observation. For the Q-factor calculation, we had to run the simulation for more than 5 days. It will take even more time to calculate the Q-factors for the elliptical disk and the circular pillar due to much smaller losses. This can be completed in the future work.

TABLE 2.3: Comparison of figure of merits for different cavities.

Cavity	Mode type	V, μm^3	Q	$Q/(V)^{1/2}$
1.5 μm Pillars [17]	Photonic dot state	0.3	8,800	16,000
4-5 μm Pillars [11]	WGM	0.3	20,000	~36,000
2 μm Microdisks [26]	WGM	0.07	500-12,000	~30,000
Nanocavities [4]	Photonic dot state	0.04	13,300	67,000

In Table 2.2 the calculated mode volume, experimental Q-factor, and the figure-of-merits of different optical resonant modes are summarized. The WGMs of 4.1 μm micropillar have the calculated mode volume of 0.3 μm^3 and the experimental Q-factor of 20,000 resulting in the figure-of-merit of about 36,000. This result shows that the figure-of-merit of WGMs of 4.1 μm pillar is even slightly bigger than the 2 μm microdisks. Recently, micropillars with Q-factors of larger than 150,000 [140] has been reported for photonic dot states which has been published after submitting our work on WGMs. On

the other hand, most recently the Sheffield's group observed WGMs with Q>60000 (A.M. Fox: private communication (2008)).

Therefore, the WGMs from the micropillar cavities can promise better performance in the CQED experiment compared to the photonic dot states from the same structure. These modes (WGMs and "photonic dot" states) aim at coupling with QDs at different locations inside the cavity, which can be used in developing fabrication techniques of cavities with strong coupling effects.

2.4 Conclusions

In conclusion, the results of experimental studies of semiconductor micropillars have shown a possibility of selective excitation of WGMs and "photonic dot" states. The results of numerical modeling of WGMs in micropillars performed in this thesis confirmed that WGMs can be excited in such cavities despite the fact that the optical confinement in the vertical direction is relatively weak. The results demonstrate the potential advantage of using WGMs for CQED experiments in GaAs/AlGaAs pillar microcavities. For strong coupling with individual QDs, $Q / \sqrt{V}$ is the figure of merit to be maximized. For 4-5 μm circular we estimate $Q / \sqrt{V} \sim 3.6 \times 10^4$ using Q=20000 and calculated modal volumes $V \sim 0.3 \ \mu$m, two times larger than that for photonic dot states in pillars with comparable or smaller sizes.

The large figure of merit achieved for the WGMs is reminiscent of the similarly high values achieved in microdisks [26, 27]. The vertical optical confinement is weaker in the pillar cavity, leading to approximately two times larger WGM modal volumes compared to microdisks of a comparable size. It should be noted, however, that in principle the Q-factors of WGMs in pillars may be higher than in microdisks due to reduced out-of-plane

scattering at the vertical interfaces of the cavity obtained by epitaxial growth as opposed to etching. To take advantage of this factor, the scattering at the sidewall surfaces of the pillars needs to be minimized, for example by additional wet etching of pillars.

In order to provide a qualitative description of WGM spectra observed in semiconductor micropillars a numerical 3D FDTD modeling was developed based on RSoft FullWave software. Considering the size of the structure and the computational resources, the number of the Bragg layers was reduced from more than 20 layers to 2-3 layers. In addition, small thickness of the Bragg layers allows to simply them with the effective index approximation.

A good agreement with experimental spectra was obtained for cylindrical and elliptical micropillars with dimensions from 2 to 5 μm. The weak convergence trend was not observed in contrast compared to the one seen in the experimental results. The difference between them may come from the material dispersion effect that was not considered in the calculation. Finally, small modal volumes of the order of 0.3 μm^3 for pillars with sizes 4-5 μm from the calculation were determined for WGMs in cylindrical and elliptical micropillars demonstrating potential advantages of these structures in CQED studies.

CHAPTER 3: COHERENT WGM COUPLING IN BI-SPHERES

3.1 Introduction

Optical resonant mode coupling in spherical microcavities has drawn considerable attention recently in order to transport optical power efficiently for the potential applications in coupled-resonator optical waveguides (CROWs) [87, 85, 114, 121, 141]. The simplest of such structures is a single photonic molecule such as a dielectric bi-sphere which has been studied experimentally [76, 77] and theoretically [73, 82, 142]. It has been shown that the spectrum of photonic molecular states is modified significantly from the normal mode spectrum of a single sphere. Interaction of the two WGMs with the same resonant frequency in an identical bi-sphere will split the frequency into two split frequency components: bonding states (Bs) and antibonding states (ABs). These split frequency components in a size-matched bi-sphere have revealed the coherently coupled photonic molecular states [73].

In the applications of photonic circuits or CROWs it is important to quantify the coupling constant(κ) between the two split frequency components based on the properties of the normal modes in a single sphere to achieve coherent optical transport. In addition, the broken degeneracy in azimuthal mode coupling has been studied [80] in bi-spheres that are located in microwells under conditions of local photoexcitation. However, this geometry leads to touching between the spheres and sidewall surfaces of the trenches with many poorly controlled points of contact between the spheres and the walls of the

microwell. This can lead to unpredictable leakage of WGMs into the substrate. In many applications, the bi-spheres should be located on top of a flat substrate that defines the boundary condition.
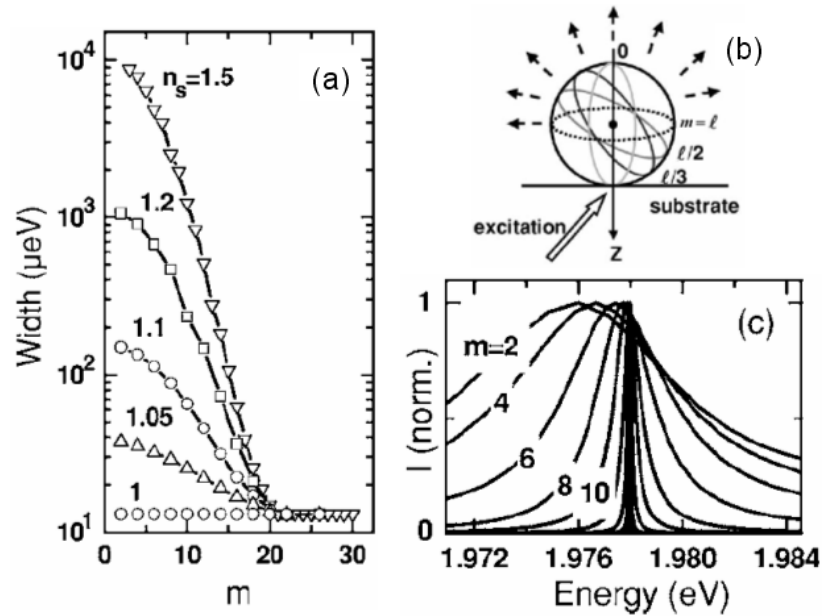
FIGURE 3.1: Modeling results of WGM of a sphere for substrate effects.
The TE_{30}^1 WGM is from a polystyrene sphere with a diameter 4.5 μm (a) Linewidth variation versus the azimuthal mode number m for different index n_s of the substrate. (b) Geometry of sphere-substrate. (c) Normalized spectrum of even m modes in the presence of the substrate [56].

This dielectric substrate broadens the linewidth of WGMs [56] which was investigated in the geometry shown in Figure 3.1(b). In this work, the scattering spectrum of a single sphere on substrate was calculated for each m mode based on the rotational symmetry along the z axis. The results of this calculation for the TE_{30}^1 WGM for polystyrene sphere with a diameter of 4.5 μm were shown in Figure 3.1. As the azimuthal mode number m gets smaller than around 20, the linewidth increases rapidly except for the sphere in free space (n_s=1) as shown in Figure 3.1(a). This strong dependence on m in

the linewidth mainly comes from the varying distance of the mode from the substrate. The EM field of WGMs is confined at a distance $r(1-m^2/l^2)^{1/2}$ on both sides of the equatorial plane and thus at a distance of $r\left[1-(1-m^2/l^2)^{1/2}\right]$ from the substrate [56]. Therefore, for smaller m the distance gets small enough to allow for significant evanescent coupling with the substrate resulting in the linewidth broadening as shown in Figure 3.1 (c).

3.1.1 Split frequency components with respect to the normal modes

The internal field distribution and the spectral features of the photonic molecular states were calculated [73] and observed [76] in many studies. Miyazaki and Jimba's paper [73] stated that in analogy to the quantum-mechanical formation of the molecular orbits, it is expected that the interaction between spheres brings about the bonding and antibonding states of the EM field. These states can be expressed as a linear combination of the Mie resonance states of each sphere. Also, Fuller [143] has observed numerically that the EM coupling between spheres causes the narrow Mie resonance to split into distinct, relatively broad peaks and dips in the forward-scattering spectrum of the bisphere.

Theoretical studies [73, 143] can take advantage of the optical symmetry of the structure in coupled spherical cavities when they are in free space. However, in most real applications the substrate plays a very important role [79] in defining the optical modes due to the interaction of the evanescent field tail outside the sphere with the substrate. In Miyazaki and Jimba's paper [73], the two spheres in free space are aligned along the z axis which is the axis of the bi-sphere as shown in Figure 3.2. Since there is no substrate that supports them, the optical symmetry can be established along the axis of the bi-

sphere. In this case, the fundamental modes ($n=1$, $l=|m|$) are circulating in the plane (x-y plane) that is perpendicular to the axis of the bi-sphere. The planes of such WGMs in two spheres are parallel to each other and have no crossing point. Therefore, the two fundamental modes in each sphere are not coupled, which results in zero splitting. On the contrary, the smallest two azimuthal order modes overlap at the interface between the two spheres. Therefore, it is expected that the coupling between the smallest azimuthal modes should be the maximum in this geometry [73].
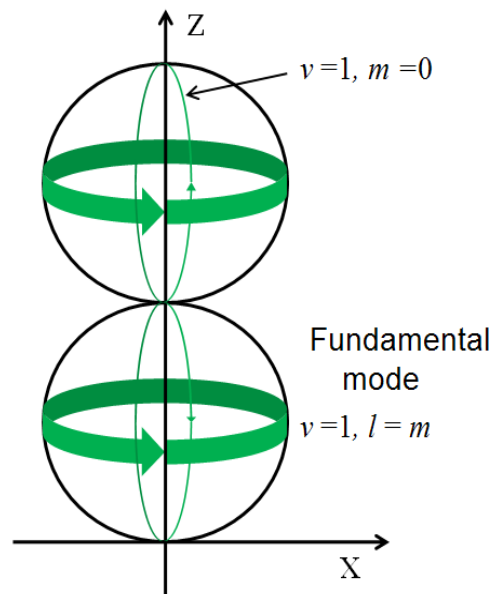
FIGURE 3.2: Bi-sphere in free space aligned along the *z* axis.
Two fundamental modes are shown in two spheres and define the plane (x-y plane) where they are circulating. This geometry is similar to Miyazaki and Jimba's paper [73].

Compared to the theoretical work above, in our experiments, the coherent bi-sphere is placed on top of the glass substrate. The substrate breaks the axial symmetry of the bi-sphere and thus defines the new boundary conditions for the system. When the two spheres are separated by a large distance, there is no interaction between them. In this

case, each sphere supports its own resonant modes with respect to the substrate as mentioned in the introduction section. The Normal axis (z axis), which is perpendicular to the substrate will define the orientation of fundamental WGMs in the equatorial plane of each sphere parallel to the substrate. Therefore, the fundamental mode that has the smallest mode volume and largest Q-factor can be defined along the circumference of the equatorial plane of each sphere. Each fundamental mode has the smallest radial number ($n = 1$) and its azimuthal mode number (m) is equal to the angular mode number (l). Depending on the propagation direction along the circumference, the azimuthal mode number m can be equal to $+l$ or $-l$ as shown in Figure 3.3.
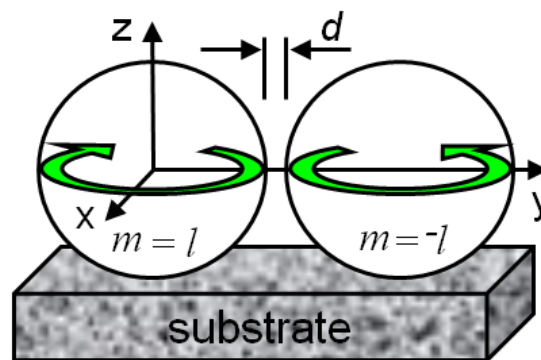
FIGURE 3.3: Schematic diagram of the fundamental modes of two separated spheres. Two spheres are separated by gap d and their fundamental modes are defined in the equatorial plane parallel to the substrate.

As the separation d between two spheres in Figure 3.3 gets smaller, the normal modes of each sphere start interacting with each other due to an overlap of their evanescent fields in the area where they are separated by the small gap d. One sphere with respect to the other will start perturbing the normal modes and vice versa. For touching or almost touching spheres the situation is similar to the formation of electronic molecular states [82]. As it was discussed previously in the introduction section such

coupling can give rise to formation of two split components [82], bonding and antibonding molecular states for each WGM eigenstate. In other words, these states can be expressed as a linear combination of the Mie resonance states of each sphere [73]. This definition is different from the case for the bi-sphere without substrate [73] where the axis of the bi-sphere acts as the optical symmetry axis in defining the modes.

3.1.2 Observation of split frequency components

The optical coupling between the optical cavities has been observed in various photonic microstructures such as planar semiconductor microcavites [144] and photonic molecules [145]. The experimental observation of the coupled states in monodispersive bispheres was achieved by T. Mukiyama et al. [76] in a bisphere. In this work, monodispersive polystyrene spheres (refractive index 1.59, sizes from 2 to 5 μm) were soaked in a solution of dye (Nile Red, concentration is about 1022 molyl, fluorescence FWHM is about 70 nm). Dye doped spheres were placed on a glass plate under a microscope. The spheres were manipulated with an optical fiber probe which was made by pulling the multimode optical fiber in a flame. By using a microscope objective lens, the individual spheres were excited with the second harmonics of a CW Q-switch Nd-YLF laser (λ = 527 nm). The dye fluorescence was collected with the same fiber probe and sent to a spectrometer with a liquid nitrogen cooled charge-coupled device (CCD) detector. Then, they measured the spectrum in parallel (Figure 3.4(A)) and perpendicular (Figure 3.3(B)) direction with respect to the tapered fiber tip as shown in Figure 3.4(a).

The fluorescence spectra of individual spheres (C) and the bisphere (A, B) in the vicinity of TE_{30}^1 and TE_{29}^1 resonances are shown in Figure 3.4 (b) and (c). For both polarizations, they observed new peaks due to an intersphere coupling, in the parallel

configuration (A), but not in the perpendicular configuration (B). The intersphere coupling is maximum for the pair of modes whose orbitals include the contact point and lay in the same plane. Therefore, the fluorescence of the coupled modes is maximum in the direction parallel to the bisphere's axis. As a result, the signal from the coupled intersphere modes is more pronounced in the parallel configuration than in the perpendicular configuration.
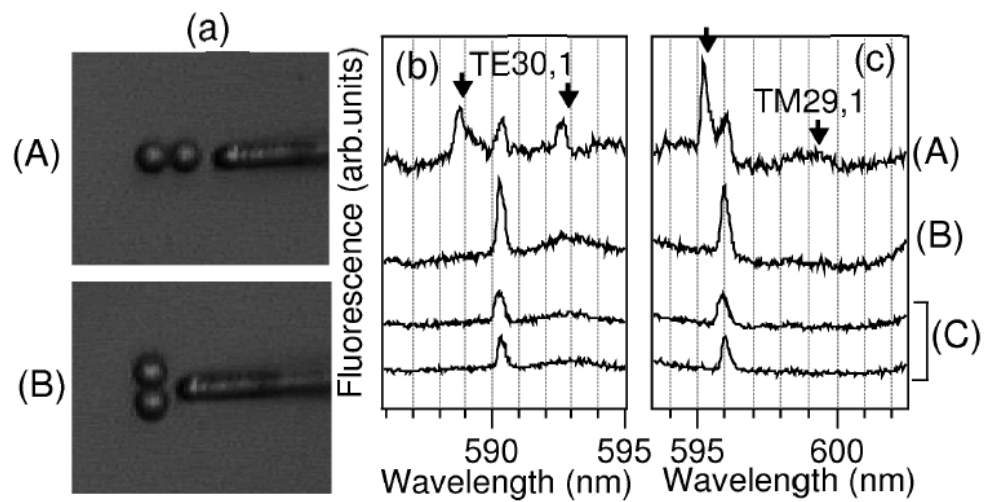
FIGURE 3.4: Optical coupling of nearly identical bisphere.
(a) Microscope images of the bisphere and the fiber probe. Two detection geometries; parallel (A) and perpendicular configuration (B). (b), (c) Spectra of resonance bisphere of TE_{30}^1 mode and TE_{29}^1 mode in parallel configuration (A) and perpendicular configuration (B). Spectra (C) show the fluorescence of individual spheres before contact. The arrows indicate the coupled modes [76].

On the other hand, smaller splitting in the coupling of the azimuthal modes with smaller numbers in bispheres has been studied for the two spheres in a microwell [82]. The experimental geometry [146] for off-axis excitation and detection of their emission spectra and microscope image of the structure are shown in Figure 3.5(a) and (b), respectively. In this work, the photon lifetime spectral distribution in two coherently

coupled spherical microcavities is studied experimentally and theoretically. The multipeak narrowband modal structure resulting from lifting the azimuthal mode degeneracy compared to the peaks of non-interacting microspheres is shown in Figure 3.6(a). Another key observation of this study is that the coupled molecular states appeared to have much higher Q-factors compared with that of single microsphere. The ratio between the photon lifetime of m modes of the photonic molecule and one of a single microsphere is shown in Figure 3.6(b).
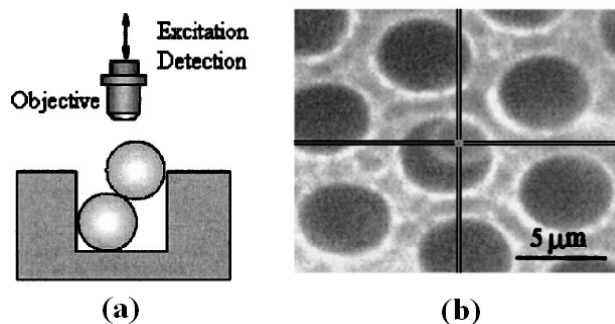
FIGURE 3.5: Bisphere in a microwell.
(a) Experimental geometry for off-axis excitation and detection of emission spectra from two microspheres in a microwell. (b) Microscope image of the structure [81]
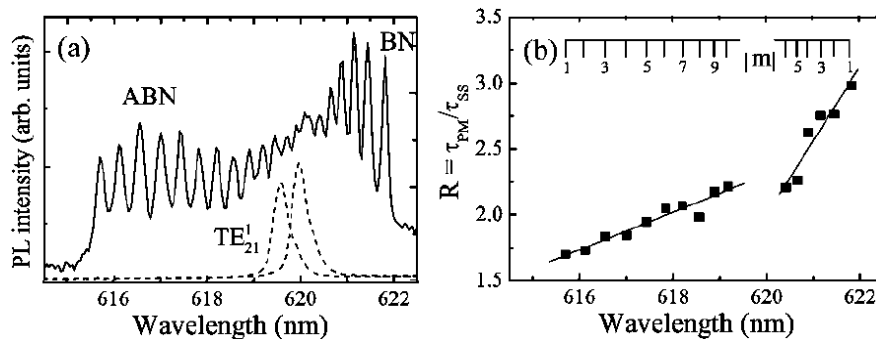
FIGURE 3.6: Multipeak narrowband spectrum from a biosphere.
(a) Emission spectra from two microspheres (solid curve) with off-axis excitation and detection and non-interacting microspheres (dashed curves). (b) Ratio between the photon lifetime of *m* modes of the bisphere and one of a single microsphere [146].

In summary, the WGM eigenstates of a sphere on substrate are determined by the interaction with substrate compared with those of a sphere in free space. The substrate also broadens the linewidths of low azimuthal modes owing to photon tunneling into the substrate. Another interesting property of the azimuthal modes in a coherently coupled bisphere is the lifting of the degeneracy for the pairs of modes with the same m numbers resulting in a multipeak narrowband modal structure. These peaks with higher Q-factor can be used as a basis for a multichannel, wavelength-tunable optical delay-line device [146]. In this work, however, the lifting of the azimuthal mode degeneracy was shown only in the spectral domain without showing the spatial profiles of the azimuthal mode coupling in a coherently coupled bisphere. The points of contacts with the walls of the microwells were not controlled in the experimental configuration of this work.

3.2 Temperature tuning of spheres

In order to obtain the coherent coupling in a bisphere, one of the critical conditions is the small size or index variation. Previous works in our group [88] demonstrated the coupling efficiencies of size-mismatched spheres. The optical coupling of the two size-mismatched spheres with sizes 3 μm (S, source sphere) and 2.4 μm (R, receiving sphere) is shown in Figure 3.7. The antibonding and the bonding photonic molecular states shown in Figure 3.7 (a) and (b), respectively, correspond to two coupled components. The calculated spectral energy densities deposited in the receiving sphere shown in Figs. 3.7 (c) - (j) demonstrate the dependency of the separation distance between the two spheres. As the inter-resonator gap d becomes smaller than 0.3 μm, the splitting between coupled states, also called normal mode splitting, starts to develop as shown in Figs. 3.7 (c) – (f).
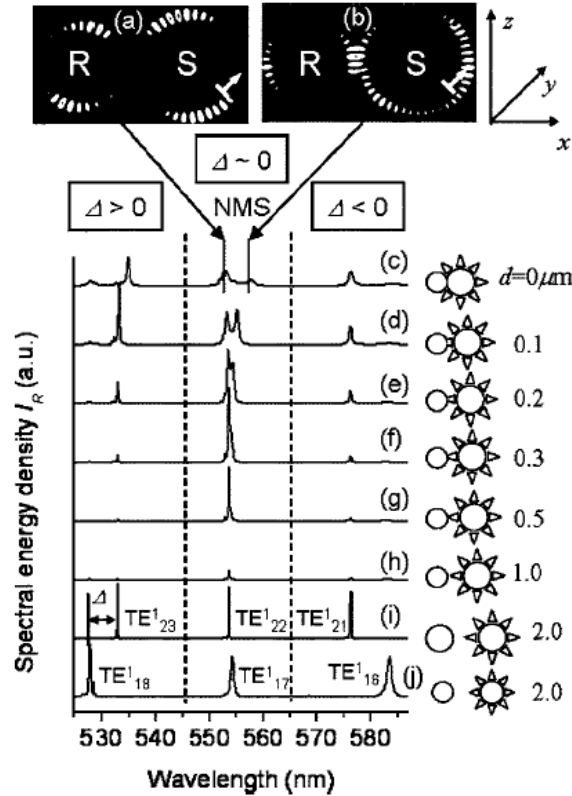
FIGURE 3.7: Optical coupling of two size-mismatched microspheres.
(a) Antibonding and (b) bonding photonic molecular states. (c)-(j) Spectral energy densities deposited in the receiving (R) sphere for different distances d between the two spheres, source (S, 3 μm) and receiving (R, 2.4 μm) spheres [88].

It is seen that the strongly detuned states ($\Delta > 0$ or $\Delta < 0$) can be coupled only at touching or nearly touching cases. However the resonant states ($\Delta \sim 0$) can be coupled at much longer distances and with much higher efficiencies. This means that only same size spheres can be coupled with maximal efficiency. Therefore, the size sorting for the coherently coupled microsphere circuits is the very important task. In this section, one of the methods to tune the WGM resonances in microspheres is introduced.

3.2.1 Temperature tuning with NiCr wire

In order to obtain an identical bi-sphere, the size or index of one of the spheres in the bi-sphere should change according to those of the other sphere. Comparing the

spectra for multiple spheres is one of the methods with which one can select very identical spheres due to high Q-factors of WGMs of the spheres. The size and the index of the sphere are two of the parameters that can shift the WGM peaks. The dependence of the position of WGM peaks on the size and index of spheres can be expressed as [147]

$$\frac{d\lambda}{\lambda_0} = \frac{dr}{r} + \frac{dn}{n_0} \tag{3.1}$$

where r is the radius of the sphere, λ_0 the resonant wavelength, and n_0 the index for large spheres ($r \gg \lambda$), regardless of the WGM polarization and the mode numbers. Eq. (3.1) enables us to measure the change of the size or the index of the sphere by monitoring the change in the resonant peaks. The diameter of the sphere can be changed by mechanical [63] or acoustic action [147] on the sphere.

Alternatively, the size and index of the spheres can be changed by changing the temperature of the cavities. In our experiments the heating effect occurs due to touching between the sphere and the substrate (NiCr wire). The thermal heating through the substrate increases the temperature of the sphere and hence changes the size or index of the sphere.

The experimental setup for the temperature heating of the microspheres is shown in Figure 3.8. The current flows through the NiCr wire (1.3 mm diameter) and the two spheres (5 and 7 μm) are attached to the surface of the wire. The optical image obtained by the imaging spectrometer shows two spheres sitting side to side at the NiCr wire as it can be observed through the wide spectrometer slit (500 μm). The two spheres are located in the center of the spectrometer slit as shown in Figure 3.8(a). For the spectral measurements the width of the spectrometer slit is reduced down to 100 μm as shown in Figure 3.8(b).
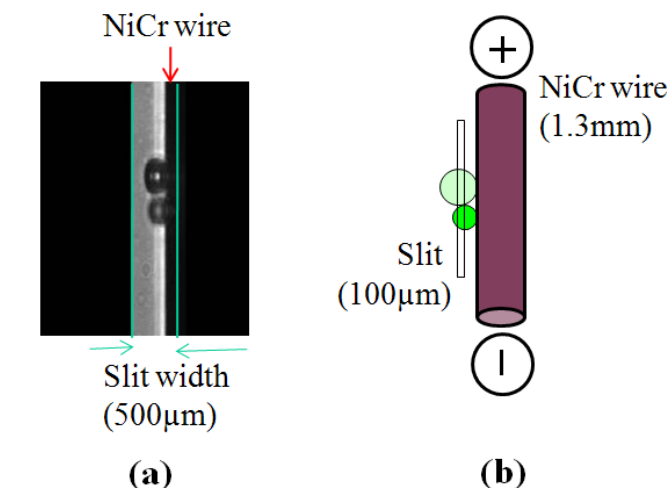
FIGURE 3.8: Temperature tuning of microspheres using a NiCr wire.
(a) Optical image through the spectrometer slit of the two spheres (5, 7μm) and the NiCr wire. (b) Schematic diagram of the temperature tuning using a NiCr wire.

The spectral images of such bi-spheres are shown in Figure 3.9. The spectral shifts of the resonant peaks as a function of applied current are illustrated in this figure. The blue and red dotted lines show the reference line for the 0 mA current applied. All the resonant peaks from 5 μm sphere show blue shift in wavelength, which means that the effective path length of WGMs decreases with the temperature, which can be explained by changes of the size or index of spheres. The graph of the dependence of the resonant peak with respect to the applied current is shown in Figure 3.10. It is seen that the heat-induced changes of the path length increase nonlinearly with the temperature. The change of the WGM wavelength is about 0.51nm for the current variation from 0 to 22.5 mA. There are other factors which are important in these experiments such as the dynamical characteristics of the current. The problem is the heating process possesses inertia typically in a millisecond range, so that it takes time for a system to keep up with

the variations of the current. Generally, the changes of the WGM resonant positions achieved in these experiments have an irreversible nature.
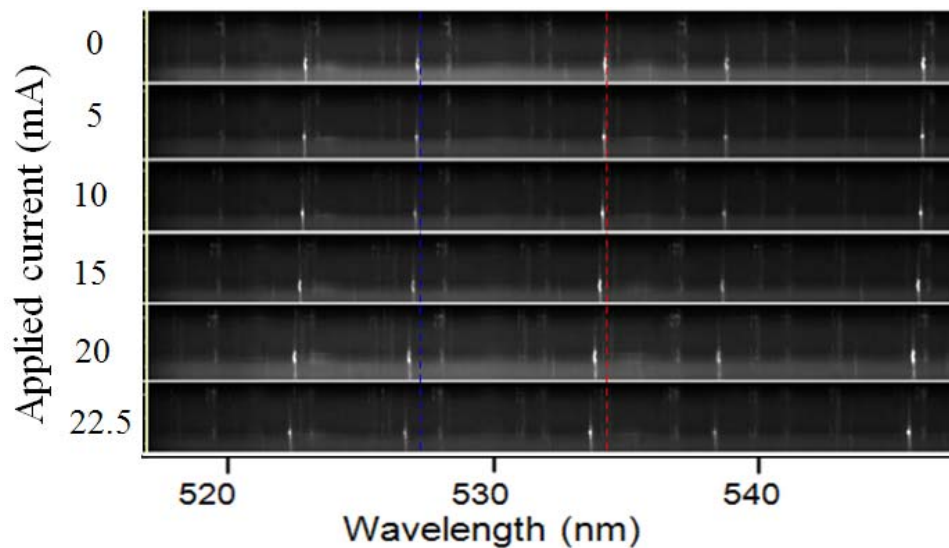
FIGURE 3.9: Resonant peaks shifted by the applied currents for 5 and 7 μm spheres.
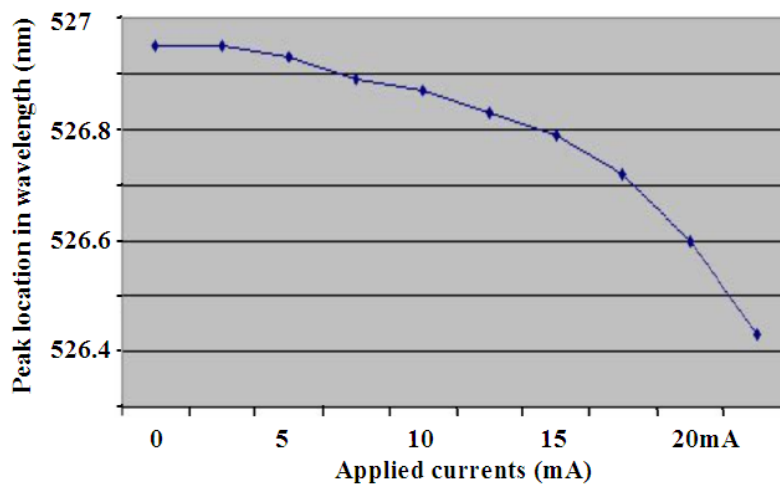
FIGURE 3.10: Wavelength shift of the peak (blue dotted line) with applied currents.

In attempt to fabricate the identical bi-sphere, two 5 μm spheres that are reasonably close in size were tuned with NiCr wire used as a local heater as shown in Figure 3.11. The two spheres were aligned perpendicular to the NiCr wire and oriented

parallel to the spectrometer slit. In this experimental configuration, one sphere was attached to the NiCr wire but the other was attached from the opposite side of the first sphere in such a way that it was not in direct contact with a heating wire. This setup was investigated in order to understand the temperature diffusion effect that may be too large to heat the only one sphere that is attached to the wire.
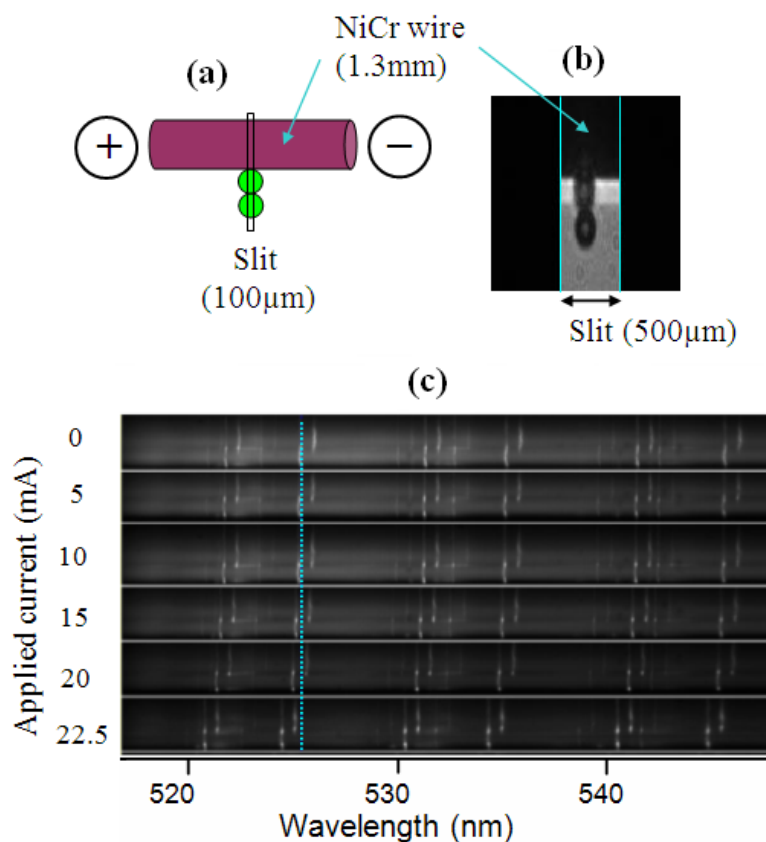
FIGURE 3.11: Temperature tuning of two 5 μm spheres by a NiCr wire.
(a) Schematic diagram for two 5 μm spheres. (b) Optical image through the slit.
(c) Spectral image for spectral shift.

The optical image of the two spheres with NiCr wire through the spectrometer slit with wide opening (500 μm) was shown in Figure 3.11(b). The spectral images of these spheres are shown in Figure 3.11(c). In this figure the peak shift is plotted against the current in a wire. The top spectral image for 0 mA shows that the two spheres have very

close sizes. The difference in wavelength is only about 0.4 nm which corresponds to the size difference of about 3.8 nm. The spectral image shows the uncoupled WGM peaks in two spheres along with their coupled split components which have much smaller intensities.

As the applied current increases, the two peaks from the two spheres shifted to the left simultaneously, meaning that the temperature diffusion is so efficient that the two spheres are heated simultaneously. It is interesting, however, that the amount of the temperature shift exceeds the WGM wavelengths difference in two spheres. This means that in principle achieving the exact resonant conditions should be feasible through the temperature tuning of just one these spheres. This can be achieved by removing thermal contact for one of these spheres. In other words, had the second sphere hanging on the first sphere been isolated from the source of temperature heating, the WGM peak positions of the first sphere could have been moved through the perfect resonance with the second sphere

3.2.2 Temperature tuning with Cr chip-scale micro heaters

In attempt to confine heating effects we reduced the sizes of heaters to microscale dimensions. This was realized in chip-scale structures with local heaters fabricated as thin metallic wires with dimensions comparable with the dimensions of the spheres, as shown in Figure 3.12. One of the five Cr stripes (3.5 μm width) is connected to the positive and negative poles of the current source in order to heat only one sphere that is sitting on the stripe. In addition, small holes for all the patterns are etched in the centers of the stripes for increased local heating effect due to reduced cross-sectional area of the metallic stripes. These holes can be used to accommodate microspheres that allow to improve the

quality of assembly microspheres on a chip. These patterns were fabricated in the cleanroom facility at the University of North Carolina at Charlotte.
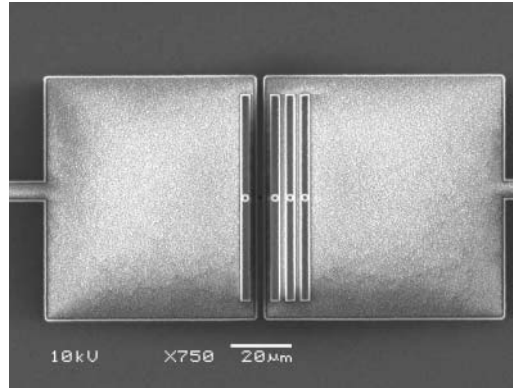
FIGURE 3.12: Micro patterns with Cr thin film using EBL.

The thin Cr film was used to fabricate these micro-heaters since the NiCr thin films were subjected to a delamination while the wet etching was performed. The main fabrication process is illustrated in Figure 3.13 with colored layers for different materials. The first step is to clean the substrate (microscope glass slide) inside the Piranha (Sulfuric Acid 96 % 1000 mL + Hydrogen peroxide 800 mL) for longer than 20 minutes. This process will remove some organic debris from the surface of the substrate. The substrate is rinsed in the cascade water flow for about 10 minutes and dried by a Nitrogen blow. NiCr or Cr is deposited with the sputter on the clean substrates to make thin film. The thin NiCr or Cr film with thickness of about 200 nm was deposited for about 60 minutes as it is shown in step (a) in Figure 3.13.
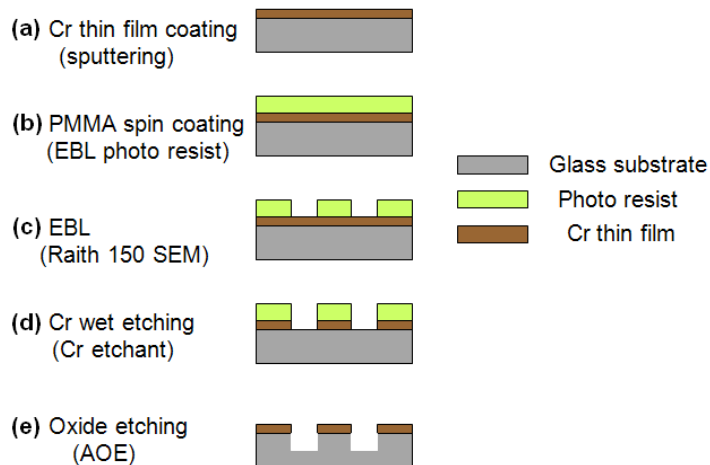
FIGURE 3.13: Fabrication process for micro patterns for local temperature heating.

Once the thin film is deposited, the PMMA (EBL photoresist) is coated by spinner after hard baking (90 degrees for about 5munites). Step (b) shows the Cr layer and PMMA layer of about 250 nm thickness. The PMMA was baked at 120 degrees for about 4 minutes. Next step is developing the PMMA using EBL and cleaning the structure with IPA (isopropyl alcohol) as shown in step (c).

The patterned PMMA layer acts as a mask to transfer the structure into the Cr layer. The structure was inserted into the Cr etchant for about 2 minutes. Since the Cr etching rate is relatively fast, attention should be paid until all the Cr is removed to make a transparent opening through the substrate as shown in step (d). The last step is to etch the oxide below the Cr layer, which is very important for better isolating the heat diffusion. This oxide etching is done using the STS AOE (Advanced Oxide Etch) tool. During this process, the PMMA layer is etched also as shown in step (e) in Figure 3.13. Then, the positive and negative poles of the current source are connected to the pads by using the conductive glue.
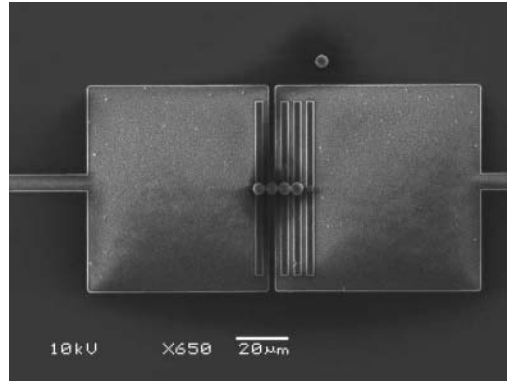
FIGURE 3.14: Four spheres on top of the patterns.

Once the micropatterns are fabricated, the spheres to be tuned are placed at top of each pattern as shown in Figure 3.14. Four microspheres are placed on top of the patterns and the last one is left on the large pad. The second sphere from the right is to be tuned by the current flow through the corresponding metallic stripe. In order to open a possibility of measuring the emission spectrum of the microspheres, the edge of the pattern is cleaved as shown in Figure 3.15. The spectral shift with applied current was observed, however, the small dimension and imperfect fabrication of the patterns limited the repeatability of the results. In addition, the pulse period dependence was not optimized for the sphere to be tuned.
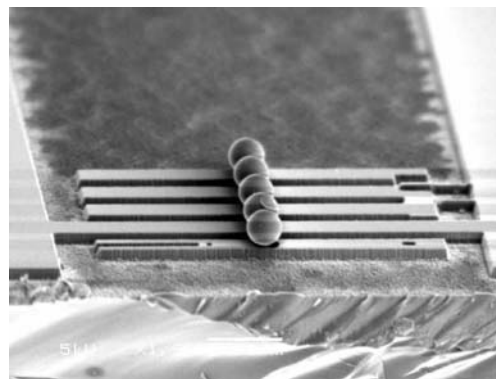
FIGURE 3.15: Five microspheres perpendicular to the cleaved edge of the substrate.
The second sphere from the bottom is to be tuned.

Thus these studies showed that in principle, the tuning of WGM resonances by using local heating effects in chip-scale structures is possible. These studies also revealed some problems of such temperature tuning effects such as spatial diffusion of heat and complicated dynamical responses of the structures to the local thermal effects. In addition the fabrication of such structures is rather challenging since it requires a combination of standard techniques of lithography and etching with the following steps of micromanipulation with microspheres. Despite these difficulties we believe that with some improvement of technology of fabrication of microheaters, this approach can be used in future for simultaneous tuning of tenths of cavities on a chip.

3.3 Normal mode splitting in the spectral images

Although the monodispersive spheres can be obtained due to the WGM temperature tuning methods described above we decided for this purpose to use an alternative approach in this thesis. This approach is based on individual inspection of tenths of spheres on the substrate in order to select more uniform spheres. Similar approach has been used in previous studies of bispheres [82] and chains [85]. In our work we improved the accuracy of selection of supermonodispersive spheres up to a theoretical limit $\delta \sim 1 / Q$, where δ - size dispersion of spheres, Q-quality factor of WGMs on the substrate. For example for 5 μm spheres we achieved $\delta \sim 0.03$ %, highest uniformity reported for microspheres up to date.

3.3.1 Experimental setup

In these experiments dye-doped polystyrene spheres with diameter of 5 μm (refractive index 1.59) are used to investigate the coherent coupling properties. A drop of dye-doped microsphere suspension was cast on the glass substrate and dried for at least

24 hours. Once the spheres dried completely, their spectra were measured using the imaging spectrometer. The pumping through a narrow band filter (450-490 nm) from the mercury lamp was provided using an inverted microscope. The pumping intensity was lower than the lasing threshold for the dye-doped microsphere. At the resonant conditions a small fraction of the broad band fluorescence emission (510 -560 nm) of the dye molecules inside the spheres is coupled into WGMs. (The fluorescent (FL) excitation (510 -560 nm) is coupled into the WGMs of the spheres.)

The fluorescence spectrum and corresponding spectral image of the source sphere with 5 μm diameter are shown in Figure 3.16. The top image shows the spectrum with the modal orders which are characteristic numbers in Mie [137] resonance of a spherical particle. The interpretation of spectral peaks can be achieved [51, 52, 86] due to comparison of the peak positions with calculated positions of Mie resonances. In our work it was achieved using the principle of scaling of the WGM wavelength with the size of the spheres on the basis of similar interpretation of the peaks performed by other groups [80, 85] for spheres with similar sizes. In our work we used the fact that the FL spectra of spheres with close sizes are qualitatively similar in terms of proportions of separations between different groups of WGM peaks with different polarizations and numbers. This allows our results to be compared with the peak positions and interpretations achieved by other groups [56, 57, 85]. In principle it should be noted that such an interpretation can also be achieved through FDTD modeling similar to that described in the previous chapter, as it was done by Kanaev et al. [88].

The left bottom image in Figure 3.16 shows the 5μm diameter sphere on a substrate. The narrow slit (50-100 μm) has the vertical orientation that is perpendicular to

the direction of the spectral image which is on the right. There are three peaks corresponding to three angular numbers l for the first and second radial order modes with transverse electric (TE) and transverse magnetic (TM) polarization in the spectral window (510 − 550 nm). The first radial mode peaks are TE_{42}^1, TE_{41}^1, and TE_{40}^1 for TE and TM_{39}^1, TM_{40}^1, and TM_{41}^1 for TM polarization. The second radial modes are TE_{35}^2, TE_{36}^2, TE_{37}^2 for TE and TM_{34}^2, TM_{35}^2, TM_{36}^2 for TM polarization. The azimuthal mode numbers are omitted due to the fact that we are not able to resolve the ultrafine structure of these modes in the spectrum presented in Figure 3.16. The spectral image shows that the vertical stripe, such for example as TE_{41}^1, manifests itself as a straight streak, which means the sphere has a very good spherical shape with a negligible eccentricity.
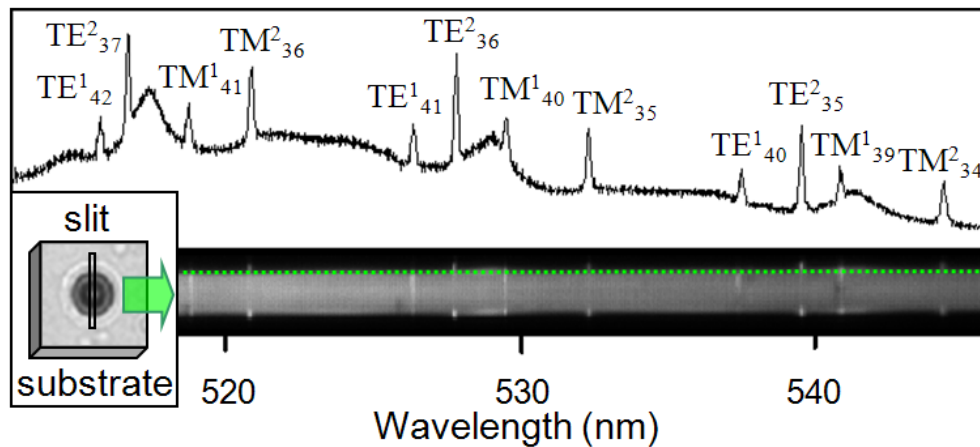
FIGURE 3.16: Spectroscopy of 5 μm dye-doped sphere.
Spectrum (top), spectral image (bottom), and measurement geometry with the narrow slit of spectrometer.

The spectral image from the spectrometer shows very narrow multiple peaks with Q-factors of about 4×10^3 of Mie resonance with a broad background emission of the FL between 510-550 nm. These narrow peaks appear due to coupling of spontaneous

emission of dye molecules into WGMs in spheres. It is possible to identify the third radial orders in the spectrum of 5 μm sphere but their linewidths are broad and overlapped with lower order peaks. Interestingly, the second radial order peaks show stronger intensity compared to the first orders. This feature has been noticed by other groups [84-86], though the reason for this behavior is not completely understood. As the wavelength increases, the free spectral range (FSR) increases.

In order to select monodispersive pairs of spheres, spectra of more than 50 dye-doped microspheres were measured and brought into a pool of similar spheres. The most identical two spheres were selected from the pool on the basis of spectroscopic characterization of the WGM peak positions, as explained later. This selection process is time consuming. The two sorted spheres were placed at the edge of a clean glass microscope slide by using the micromanipulation. A tapered fiber tip, fabricated in the clean room, was used to manipulate the spheres. The capabilities of this technique are used to assemble the first character of Korean as shown in the SEM image of Figure 3.17 (a).
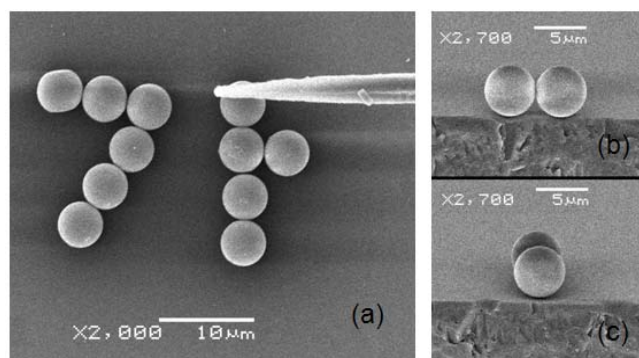
FIGURE 3.17: SEM images of microspheres manipulated by a tapered fiber.
(a) First Korean character formed by micromanipulation using the tapered fiber tip. Bi-sphere aligned parallel (b) and perpendicular (c) to the edge of the substrate.

Two identical spheres are brought into contact to form a coupled resonator as shown in the SEM images of Figure 3.17 (b) and (c). Figure 3.17 (b) shows the orientation of the bi-sphere parallel to the edge line of the substrate. This orientation is very useful for measuring the emission spectrum from the contact point between the two spheres and from the edges of the spheres where the strong scattering intensities from the coupled modes can be captured.

Another interesting geometry is the perpendicular orientation of the bi-sphere with respect to the edge line of the substrate as shown in Figure 3.17 (c). This geometry allows access to the emission along the photonic molecular axis. In order to interpret the spectral images from the same bi-sphere, all the different measurement geometries should be considered. Some resonant peaks are very close to each other and can be overlapped or superimposed, which makes their interpretation to be complicated.

3.3.2 Spectral images detected in various configurations

The schematic diagram of the two spheres on the substrate with large separation and their spectral images with mode numbers are shown in Figure 3.18 (a). The two preselected almost identical microspheres are placed on top of the substrate and the spectrometer slit is aligned parallel to the two spheres. The optical pumping of the spheres and the detection of their fluorescence was performed perpendicular to the substrate planes. The spectral image shows that all peaks aligned very well with each other in two spheres. This means that for the selected spheres the size disorder was limited at the level ~0.03 % determined by the factor of 1 / Q.

The resolution of the spectrometer is equal to the product of the linear dispersion of a given model of spectrometer and the slit width. The linear dispersion of Acton Pro

spectrometer with 1200 line/per mm grating is 1.4 nm/mm. With the slit width of 100

micron it provides a resolution of 0.14 nm.
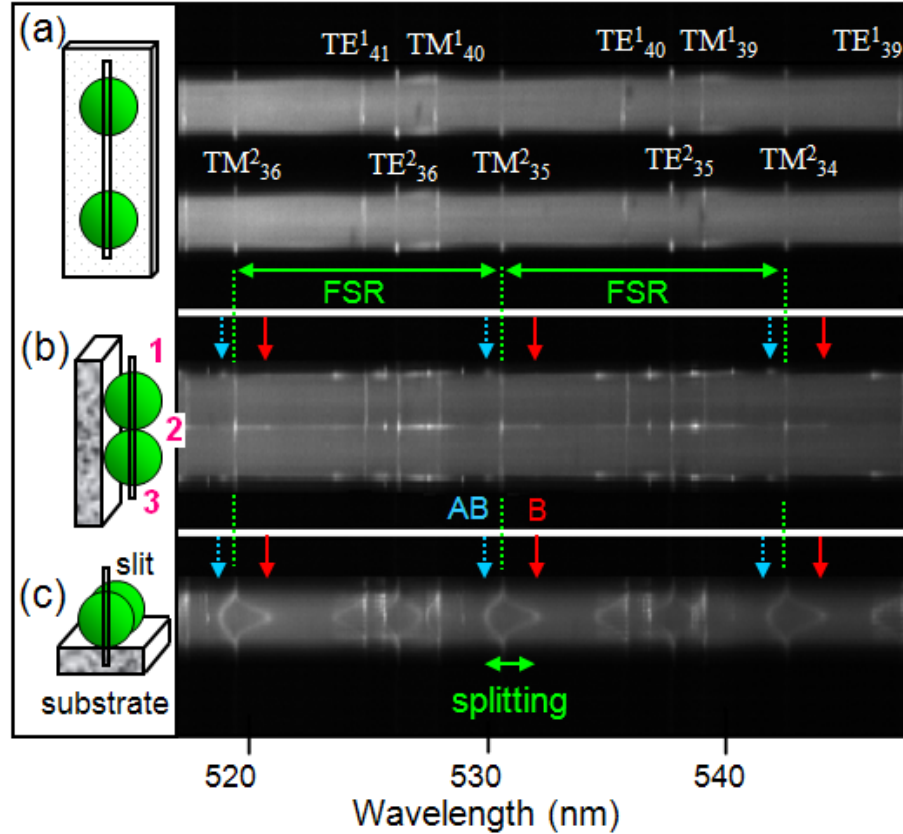
FIGURE 3.18: Spectral images from different measurement geometries.
(a) Two identical spheres with big separation and their spectral images. (b) Bi-sphere aligned along the edge of the substrate and the spectrometer slit, and its spectral image. (c) Axis of bi-sphere perpendicular to the edge line of substrate and the spectrometer slit, and its spectral image.

The second order radial order peaks also show the large intensity at the edges of

the sphere. The first order peaks show relatively uniform intensity along the cross-section

line of the sphere. For example, TE_{36}^2 and TE_{35}^2 show two large peaks that are located at

the edge of the spectral image whereas TE_{41}^1 and TM_{40}^1 show fairly uniform (even)

intensity across the spectral image. Free spectral ranges (FSR) for the second radial order

modes with TM polarization (between TM_{36}^2 and TM_{35}^2, and between TM_{35}^2 and TM_{34}^2) which are well isolated from other modes, are shown to be about 12 nm. The value of NMS can be estimated as [138]

$$\Delta\lambda_{FSR} = \frac{\lambda^2}{2\pi r}\frac{\arctan(\sqrt{n^2-1})}{\sqrt{n^2-1}} \tag{1}$$

where λ is the free space wavelength, n refractive index of sphere, and r radius of the sphere. This formula for the sphere with experimental parameters (r = 2.5 μm, λ = 530 nm, and n = 1.59) gives an estimate for FSR around 12.9 nm that is close to the experimentally observed value about 12 nm.

In order to study WGM coupling phenomena two sorted almost identical spheres are brought into contact and aligned parallel to the edge line of the substrate as shown in Figure 3.18(b). The spectrometer slit is also aligned parallel to the axis of the bi-sphere. Excitation through the narrow (less than 100 μm) spectrometer slit is captured simultaneously and dispersed perpendicular to the orientation of the slit as shown in the right of Figure 3.18(b). In this geometry the slit is mainly capturing the coupled molecular modes located in the equatorial plane. These modes correspond to coupling between fundamental modes ($n=1$, $m=l$) in individual spheres. The spectral image on the right of Figure 3.18(b) shows the mormal mode splittings (NMSs) at the three interfaces (1, 2, and 3 in the schematic image in Figure 3.18(b)). The two main observations in this image are: (i) the split components are seen only at the three interfaces, and (ii) the coupled states are dominated by these three areas, edges and center of bi-sphere, there are no coupled modes detected at other areas of the spectral images.

In order to explain these two observations, not only should the spectral and spatial distributions of WGMs be taken into consideration but also their scattering efficiencies. Since the direction of WGM scattering has a tangential direction in spheres, the spectral peaks observed at the edges of bispheres and at the touching point between the spheres have maximal contributions to the observed spectral manifestations of WGMs. The scattering efficiency reaches maximum for the collection of light perpendicular to the axis of the bi-sphere. Therefore, the three interfaces can be the best locations for observing the splitting states. In addition, the slit is located in the equatorial plane of each sphere where the two fundamental modes are coupled. Therefore, the coupling of the two fundamental modes of each sphere results in the largest splitting detected in spectral images presented in Figure 3.18(b).

The second observation in this spectral image is that only the uncoupled states of the individual sphere are detected in the sphere regions between these interfaces 1-3 in Figure 3.18(b). As mentioned earlier it can be explained by poor efficiency of scattering of low order azimuthal modes into the collection optics in our experimental set up in this configuration. In addition, these very low azimuthal modes have poor coupling efficiency due to the small mode overlap with the same order of mode in the opponent sphere. Only several azimuthal modes from the fundamental modes ($m = l$) for the given WGM eigenstate show reasonable coupling to produce resolvable split components. Therefore, the straight lines in the sphere region can be associated with low order of azimuthal modes ($m<<l$). This will be discussed in the following section.

The two split components are defined as the antibonding (AB, light blue) and bonding (B, red) states [78, 80] as shown in Figure 3.18(b). with respect to the normal

modes (dotted line, green) of the second radial order with TM polarization. These Bs and ABs are identified by the red dotted arrows and the light-blue dotted arrows, respectively, for the second radial order modes with TM polarization. For instance, the AB for TM^2_{36} is shown in light-blue dotted arrow at wavelength of 520.63 nm and B in red dotted arrow is at wavelength of 522.51 nm. The separation between B and AB split components is shown as NMS in Figure 3.18(c). For TM^2_{36} peak it is equal to 1.88 nm. The NMSs for TM^2_{35} and TM^2_{34} are 2.05 and 2.19 nm, respectively.

Therefore, the NMS for the second radial modes gets larger as the angular mode number decreases, i.e., the wavelength increases. This trend looks the same for all the other order modes and more detailed analysis will be discussed in the next section. Interestingly, in this geometry, the ABs molecular states are shown at the two outer interfaces whereas the Bs states are located in the center interface. This means that the two outer interfaces provide more scattering intensities from ABs compared to the scatterings from the Bs. However, at the central interface the B states are stronger than the AB states due the fact that the spatial distribution of B states is strongly peaked at the center of bi-sphere.

The schematic diagram in Figure 3.18 (c) shows the geometry of the measurement that reveals interesting features of the coupling properties in bi-spheres. In this measurement geometry, the axis of the bi-sphere is perpendicular to the edge line of the substrate and the slit of the spectrometer. In addition, the slit of the spectrometer is perpendicular to the substrate. The optical axis of light collection optics is aligned with the axis of bi-sphere. Therefore, the scattering intensity from the first sphere located close to the edge line of the substrate is collected along the direction of the axis of the bi-sphere.

The weakly coupled WGMs with small azimuthal numbers are not well pronounced in Figure 3.18 (c) since the slit located at the center provides poor efficiency of collection of light scattered at the right and left boundaries of the spheres. The scattered light originating from coupled azimuthal modes with large numbers is collected more efficiently in this geometry. The reasoning for this behavior is not completely understood but can be connected with the depth of focus for our experimental setup. This will be investigated in further studies.

The spectral image in Figure 3.18(c) shows that characteristic kite shape features occur near position of each uncoupled WGM peak. The second radial order modes (TM_{36}^2, TM_{35}^2, and TM_{34}^2) especially show clearly the kites in the spectral images due to the fact that they are well separated from the neighboring peaks.

The bonding (B) and antibonding (AB) states are shown in Figure 3.18 (c).These states can be associated with the horizontal vertices of kites. The corresponding states have maximal separation along spectral axis (in wavelengths) indicating that their coupling is strongest for a given set of azimuthal modes. These horizontal vertices of kites have the same spectral positions as B and AB states shown in Figure 3.18 (b). The horizontal vertices of the kites in Figure 3.18 (c) are located at the center of the spectral image of a sphere (along vertical axis). This spatial location is the place where the fundamental modes are circulating and the contact point between the two spheres is located. The splitting strength gets smaller away from the center of the spectral image of the sphere. This can be explained by the reduced spatial overlap of the lower order azimuthal modes similar to the previous results obtained for bi-spheres in microwells [80].

Another experimental configuration is shown in Figure 3.19. In this geometry, the axis of the bi-sphere is perpendicular to the edge line of the substrate. The slit is oriented parallel to the substrate as shown in the schematic images in the left part of Figure 3.19. Three dotted red circles in the spectral images on the right show the split components in the vicinity of the position of uncoupled TM_{35}^2 WGM resonance for three different locations of the slit. Three dotted green arrows correspond to the center of the image of the sphere in vertical direction. In Figure 3.19(a) the slit is located in the center of the image of sphere with the corresponding spectral image on the right. The coupled components of TM_{35}^2 WGM resonance is shown inside the circle. The triangular shape for the B states to the right of the normal mode peak is clearly seen. In contrast, the AB states seem to manifest themselves as several streaks shifted to the left from the uncoupled WGM resonance rather than as a triangular shape.
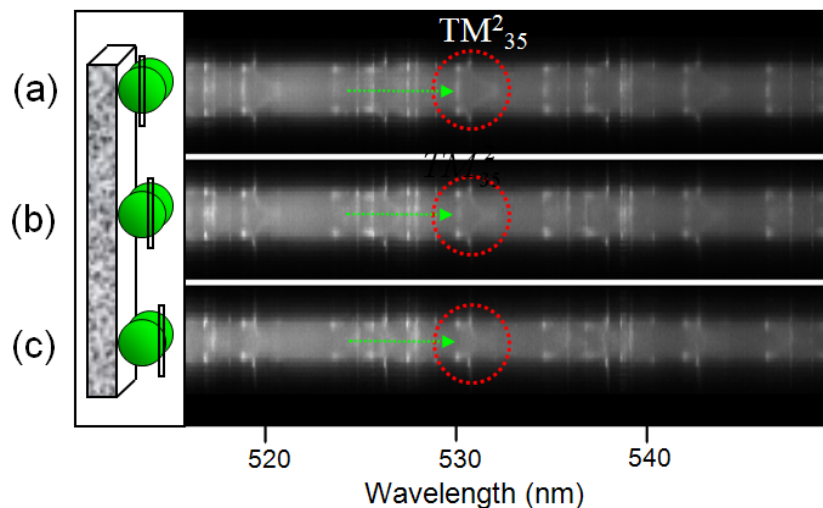
FIGURE 3.19: Spectral images by shifting the slit location.
   The slit is located with respect to the sphere on the central position (a), right (b), and right edge (c). Splitting states for different azimuthal modes for Bs in TM_{35}^2 gets smaller as the slit moves to the right of the sphere.

The explanation of the observed asymmetry in the spectral images of the coupled states in this configuration requires further studies. The reason for the asymmetry has been explained by intermodal coupling [76]. There may be another reason connected to the different type of spatial distributions for the detuned bisphere coupling in the theoretical calculation [88] which is consistant with our results. One of the factors which can be important in further studies is connected with the role of the depth of focus for our imaging optics. Typically, we adjusted the depth of focus inside the first sphere in order to obtain most clear spectral images. However in our experiments the depth of focus was not controlled precisely.

The results presented in Figure 3.19 (b) correspond to a configuration where the slit is shifted a little bit to the right from the center of the sphere as illustrated in the schematic sketch. In this case, the slit is aligned with the azimuthal modes with smaller than l numbers. These modes spread inside the spheres away from the equatorial plan. As a result they have smaller spatial overlap. Their coupled components have smaller spectral splitting. This is generally consistent with the experimental observations in Figure 3.19 (b). The peaks along the green dotted arrow become weak and the separation between the normal mode and B state gets smaller. This is because the slit captures the splitting states from the lower order azimuthal modes and their splitting strengths are smaller. The spectral trends described above become more obvious with further shifting of the position of the slit illustrated in Figure 3.19(c). From this measurement, it is seen clearly that the lower order azimuthal modes have a smaller splitting strength.

3.4 Analysis of coupling states

In order to understand the spectral image with the kite shape, the spatial mode distribution for each azimuthal mode has to be considered as shown in Figure 3.20. This is a simple schematic image which represents the distribution of field only qualitatively. The cross-sectional spatial mode distribution for the fundamental mode ($m = l$, $n=2$) and the lower order azimuthal mode ($m < l$, $n=2$) are shown schematically in Figure 3.20(a) and (b), respectively. When the two spheres are separated by long distance, the two normal modes are defined with respect to the substrate. The fundamental modes are elevated from the substrate and so the interaction with the substrate is very small. Therefore, the leakage of the fundamental modes to the substrate must be small [56] resulting in large Q-factor.
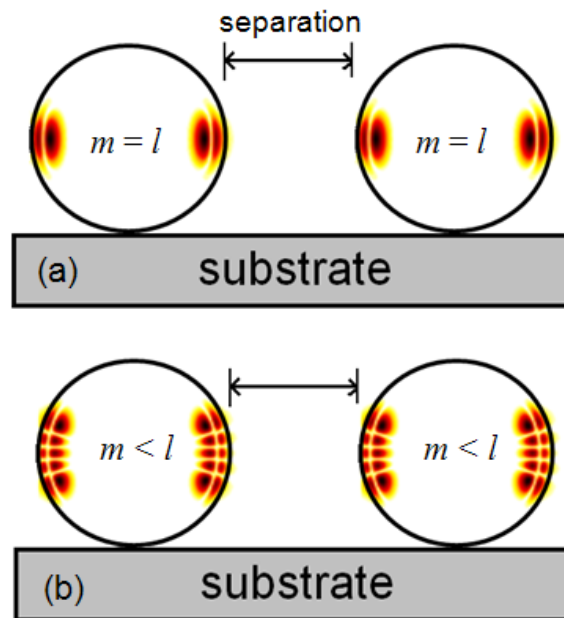
FIGURE 3.20: Two spheres with a big separation for the fundamental modes. (a) and lower order azimuthal modes (b).

On the other hand, the lower order azimuthal modes as shown in Figure 3.20(b) have smaller separation from the substrate. As the azimuthal mode number gets smaller, the largest peak of the mode moves closer to the substrate. Due to this leakage to the substrate, lower azimuthal modes have smaller Q-factors [56] compared to the fundamental mode. The exact number of azimuthal modes with sufficiently high Q-factors is difficult to estimate. On the basis of previous experimental work performed on spheres with comparable sizes [80] it can be assumed that at least about ten azimuthal modes with m numbers approaching that for the fundamental mode have sufficiently high Q-factors (Q>1000) that can couple with each other when the two spheres get in touch.

Once the two spheres are in touching position on the substrate, the evanescent field from the modes will overlap. This overlap will split the normal mode peak into B and AB states. In other words, the optical path length of one sphere will change due to touching the other sphere that has higher refractive index compared to the air. In Figure 3.21(a) and (b) two configurations are shown where the two spheres are in contact and the two pairs of normal modes of TM_{36}^2 with different azimuthal modes are overlapped at the contact point. Their coupled components are detected at the center of the spectral image (line A) resulting in the maximal splitting along the horizontal diagonal of the kites shown in Figs. 3.21(c) and (e). This splitting is indicated as normal mode splitting (NMS) in Figure 3.18(c).

On the other hand, the azimuthal modes with $|m|<l$ have the maxima of intensity some distance from the equatorial plane, as shown in Figure 3.21(b). Their coupled components are detectable at the positions B and C indicated in Figs. 3.21(e). They are characterized with smaller splitting compared to that in the position A, as seen in Figure

3.21(d). The least coupled WGMs have positions approaching the vertical corners of the kites near the edges of the spectral image. The kites appear as continuous lines because of the limited resolution of our spectrometer (~0.1 nm). In fact, they are expected to be formed by a finite number of coupled pairs of azimuthal modes. Similar effects have been observed using off-axis excitation [80] in bispheres confined in microwells. The observed kites thus allow the unambiguous connection of NMS to corresponding WGM eigenstates identifiable by the positions of the kites' vertical corners.
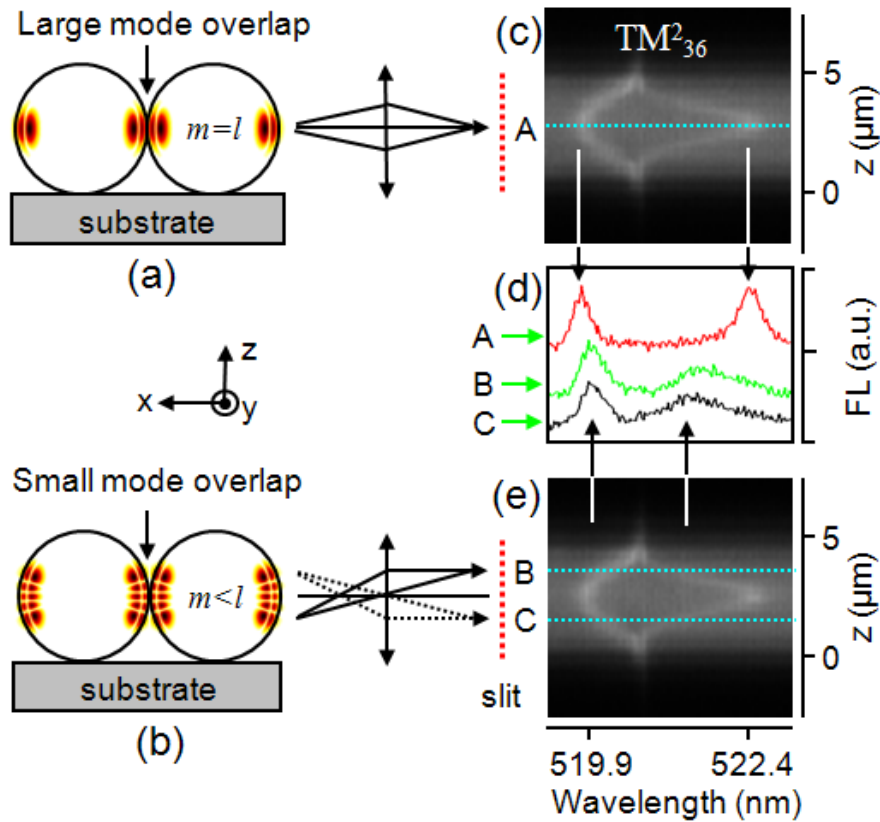
FIGURE 3.21: Kite shape ($\lozenge$) from coupling between the two normal modes (TM^2_{36}). Schematic image of the fundamental mode (a) and lower order azimuthal mode (b) in the bisphere. (c) and (e) Spectral images with splitting states from the fundamental mode (dotted line A) and the lower order azimuthal modes (two dotted line B, C). (d) Spectra from the dotted line A, B, and C. The central column illustrates the corresponding imaging points between the sphere and the spectral image.

3.5 Splitting strength dependence on optical parameters

We measured and analyzed the spectral response of the bi-spheres with different sizes in order to quantify the splitting with respect to the optical mode numbers (l, n, and polarization) as shown in Figure 3.22. In spite of the difficulties with interpretation of coupled components due to the overlap of multiple peaks originating from different WGMs, we were able to measure the splitting from the bi-spheres with sizes from 2.9 up to 6 μm by considering all the detection configurations comparatively as illustrated in the previous section. Since the emission band of the green dye doped spheres spans the range of wavelengths from 510 to 550 nm with the same refractive index (n = 1.59) for all the spheres, the angular quantum numbers and the radial order numbers vary for different sphere sizes. The second order radial modes were analyzed for spheres with sizes from 4 μm. The third radial modes can be measured for 6 μm spheres but their coupling strengths are comparable to the detection limit due to small separation and broad line width. The characteristic kite shapes in spectral images are shown to be very useful in relating the coupled states to their uncoupled eigenstates, which are WGMs in well separated spheres.
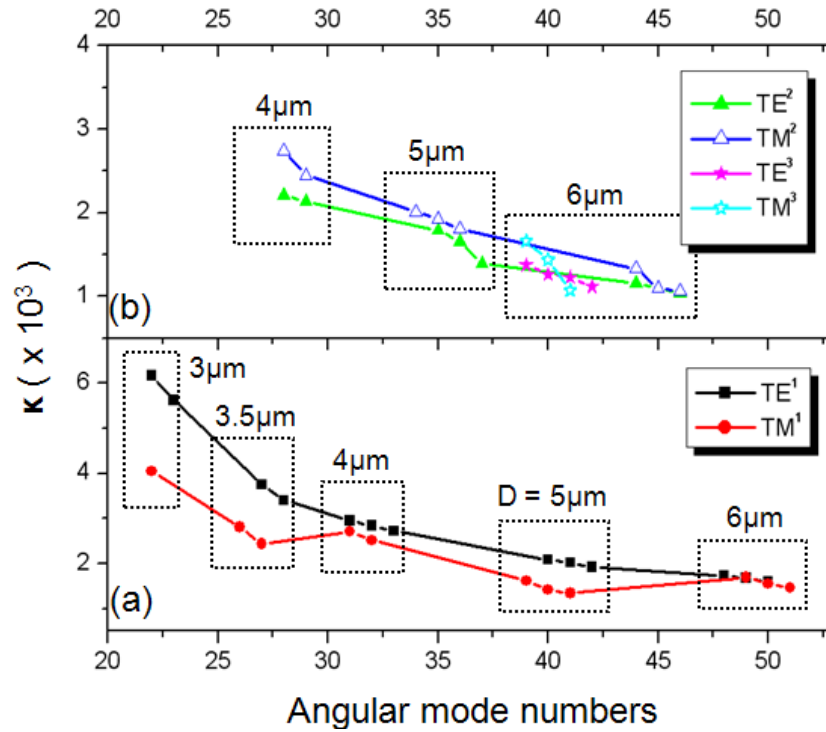
FIGURE 3.22: Coupling parameters as a function of the angular mode numbers.
(a) First radial order dependency with TE (square dot) and TM (circular dot). (b) Second (triangle) and third (star) radial order dependency with TE (hollow) and TM (filled).

The coupling parameter [76] was defined as half of the normalized splitting in wavelengths in the vicinity of the uncoupled resonant wavelength between the AB and B states. In most cases, the two split components are not symmetric with respect to the normal modes, so the coupling parameters can be considered as an average splitting strength. These two splitting states are from the coupling between the two fundamental modes that make the largest spatial mode overlap resulting in the maximum splitting

The most apparent result from Figure 3.22 is the dependence of the coupling parameters on the angular mode numbers or sphere diameter regardless of the polarization and the radial order number. This can be explained by considering the fact that the smaller the sphere size or the angular mode number, the more evanescent electric

fields outside spheres, which results in bigger coupling parameters due to larger mode overlap [76].

Another observation is that TE polarization shows larger coupling parameters than TM polarization for the first radial order numbers as shown in Figure 3.22(a). However, for the second radial order numbers TM polarization shows bigger coupling parameters and they are comparable for the third radial order numbers as shown in Figure 3.22(b). The dependence of coupling parameters on the second radial order numbers in Figure 3.22(b) shows quite similar results as in Figure 3.22(a) for the first radial order numbers.

3.6 Conclusions

In conclusion, we have investigated the NMS and various coupling effects by means of the spatial and spectral distribution of the coupling of bi-spheres. We selected supermonodispersive bi-spheres by monitoring the spectrum of individual sphere. We observed characteristic and peculiar kites in spectral images of such bi-spheres. It is shown that such kites simplify the interpretation of dense spectral images of coupled cavities. This peculiar kite's shape reveals that coupling between the respective azimuthal modes gets smaller with a decrease of azimuthal number. We have quantified the dependence of the coupling parameters on three mode numbers (l, n) by measuring the maximum splitting from the coupling between the fundamental modes ($l=m$, $n=1$). Coupling parameters are inversely related to the angular mode numbers and similar splittings are observed for different radial mode numbers. TE modes with first radial order show larger splittings whereas TM modes show larger splittings for second radial orders.

It maybe be possible to perform a massively parallel sorting of spheres with similar size resolutions which has been theoretically predicted [19] for microspheres based on using size-selective radiative pressure. Such supermonodispersive microsphere resonator circuits (MRCs) allow the control of tight binding photonic dispersions that can be used in many devices such as slow light structures, filters, arrayed resonator LEDs, sensors and microspectrometers.

CHAPTER 4: NIMS IN DETUNED MICROSPHERE CHAINS

4.1 Introduction

4.1.1 Optical transport in size-detuned microsphere chain

Recently optical transport in size-detuned microsphere chain has been studied due to WGMs coupling [87, 89] and NIMs [90]. The microsphere chains arranged as a linear chain provide optical transport due to two different mechanisms: (i) tight binding between WGMs, (ii) coupling occurring as a result of focusing produced by cavities operating as a series of periodically coupled microlenses [95]. Each sphere in the chain produces the photonic nanojet that has elongated shape and subwavelength lateral size. In a chain of spheres, such photonic nanojets result in periodic modes called NIMs [90].

The strong coupling [76] between WGMs have been observed experimentally [76] in systems of supermonodispersive cavities selected using spectroscopic characterization. On the other hand, in size-detuned bispheres and in the chains of disordered cavities, WGM-related optical coupling was observed [87, 88] by use of evanescently coupled dye-doped spherical cavities pumped above the lasing threshold for WGM peaks [87]. Figure 4.1 shows the scattering spectra obtained from undoped 9 μm spheres (1-5) coupled to a source of light (dye-doped 10 μm sphere S). The scattering peaks originate from the WGMs resonances in the S sphere [87]. In this case, the ratio of signals measured for a peak at $\lambda = 546.6$ nm from the fifth and first undoped spheres corresponds to average attenuation of 3.7 dB per sphere [87]. The size dependence of the

transport efficiency is illustrated in Figure 4.2 for different chains with sphere sizes varying in 3-20 μm range. It is seen that the attenuation per sphere is ~3-4 dB and independent of the size of the spheres. This value of attenuation can be attributed to the fact that the exact WGM coupling conditions are improbable in the chains when ~1 % size variations occur [87].
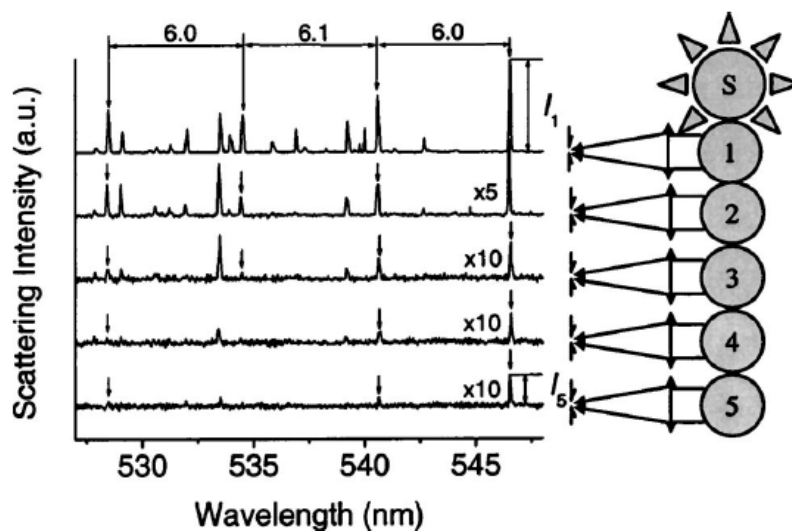
FIGURE 4.1: Spectra from undoped spheres coupled to a dye-doped sphere.
Five 9 μm spheres (1-5) are coupled to a source of light (dye-doped 10 μm sphere S) [87].

In this work [87], the S sphere possesses not only the evanescent fields but also radiative and scattering modes. Therefore, a possible mechanism of such optical transport can be connected with the formation of localized photonic nanojets at the shadow-side of each sphere illuminated by a plane wave [95]. In this mechanism the chain of spheres operates as a series of nonevanescently coupled microlenses for such modes [95]. The properties of NIMs in this size-detuned microsphere chains are different from the coupling of WGMs due to the radiative nature of photonic nanojets studied previously in single spheres under conditions of plane wave illumination [93, 94]. The existence of

NIMs in size-detuned microsphere chain has been demonstrated for the first time in dye-doped microsphere chains [90]. These results [90] were presented in Chapter 1 in Figure 1.13. They showed that the losses are maximal in the vicinity to the source of light and gradually reduce along the chain down to ~0.5 dB per sphere.
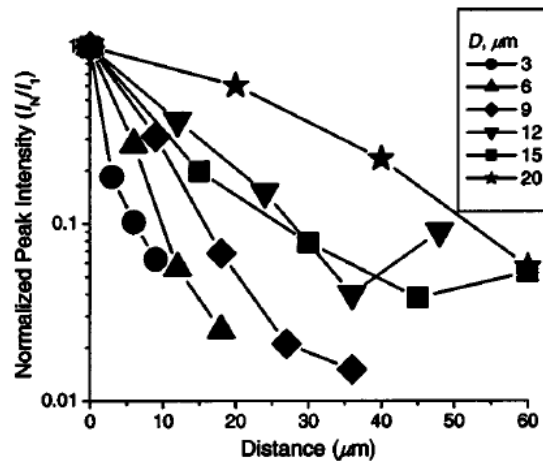
FIGURE 4.2: Dependency of the intensity of scattering peaks from different spheres. The intensities for different spheres (N=1, 2, 3, …) along the chain are normalized on the intensity of the same peak in the first undoped sphere $[I_N(\lambda)/I_1(\lambda)]$ as a function of the distance between the centers of these spheres [87].

Some questions still remained open after all these studies. It was shown that the level of losses is decreased along the chains. However the level of these losses has not been studied in very long chains of cavities.

The geometrical properties of NIMs such as their periodicity also require additional study.

Transmission measurements have been performed [90] without spectral resolution for the transport of NIMs. This has been done using scattering techniques. Although NIMs are not strong resonant modes, it is interesting to study their transmission

properties with the spectral resolution. It is also important to perform such measurements by using more direct measurements of the transmitted light.

In theory [95], the photonic nanojets are created by plane wave illumination. However in experiments [87, 89] it is possible to use evanescently coupled sources of light with WGMs such as dye-doped microspheres. In such cases one can expect a complicated interplay between different mechanisms of light transport to occur along the chains. These studies also require sufficiently long chains which have not been available previously.

This chapter presents the results of such studies in extremely long (up to about 100 spheres) chains. The results were achieved by using a combination of microscopy, spectroscopy, self-assembly and micromanipulation techniques.

4.2 Spectroscopic measurement of losses of NIMs

4.2.1 Fabrication of a microsphere chain

It is critical to fabricate a very straight microsphere chain for this experiment. Two different kinds of microspheres, undoped with diameter of 4.1 μm and dye-doped (red, green, and blue) microspheres are shown in Figure 4.3(a) and (b), respectively as examples. In this experiment, chains of monodispersive (~1 % size dispersion) undoped polystyrene spheres (Duke Scientific Corp.,) with refractive index n = 1.59 and mean diameter 5.0 μm were fabricated on glass substrates by using the self-assembly technique [148].

When a liquid drop with particles evaporates, the boundary between air and the liquid is pinned, that is, immobilized on surface defects. Then, the capillary flow pushes the particles to the boundary so that the particles can form certain shape as the

evaporation proceeds. Under certain conditions straight lines can be formed. The three conditions are: (1) evaporation occurs between partially wetting surfaces such as microscope slides, (2) the presence of pinning points, and (3) the presence of foaming surfactants [148].
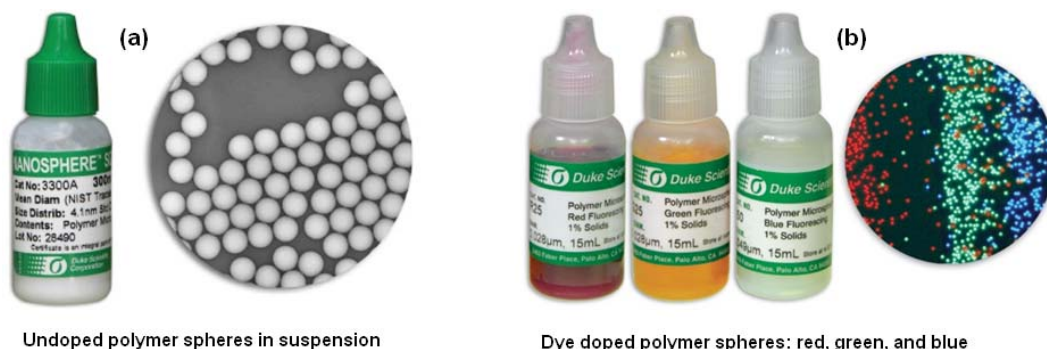
FIGURE 4.3: Images of undoped and dye-doped microspheres.
(a) Undoped polymer spheres in suspension with diameter of 4.1 μm, (b) dye doped polymer spheres for red, green, and blue fluorescence.

In order to fabricate chains of spheres we used the self-assembly method developed previously for manipulating submicron spheres [148]. In this experiment, a drop of sphere suspension was deposited on the glass substrate and then another glass substrate was overlaid so that the sphere suspension became sandwiched between the two substrates as shown on top of Figure 4.4. It is observed that the liquid film shrinks down inside the two glasses due to the surface tension as it dries. The microspheres in the liquid were forced to move along the surface of the liquid and form a chain inside narrow liquid channel. By "pinning point" we mean an area on the substrate where the evaporating liquid tends to stay or aggregate. Such a point can be formed by a large cluster of touching spheres, by a single sphere of larger size, or by a defect on the substrate. The straight channels are typically formed as a result of stretching of microfluidic flows from

the areas with large deposits of microspheres to such pinning points, as illustrated on the bottom of Figure 4.4.
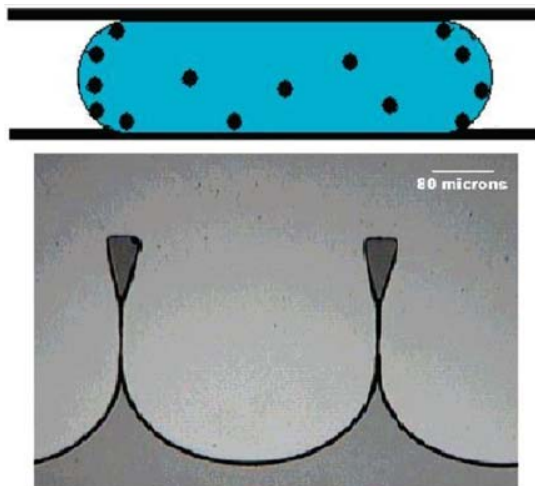
FIGURE 4.4: Fabrication of chains by self-assembly method.
Liquid suspension with microspheres sandwiched between the two substrate glasses (top) and two sphere chains start forming toward the pinning points (bottom) [148].

About 24 hours are required for the liquid to dry completely. After the liquid is dried completely, the two glass substrates are separated carefully. Usually the self-assembled microsphere chains are formed on both surfaces of the two substrates. Each glass substrate has to be examined in the microscope to find a straight long chain as shown in Figure 4.5(top). Once a chain is identified, a dye-doped sphere in Figure 4.3(b) is attached to the one end of the chain as a source of light as shown in Figure 4.5(bottom). Spheres are manipulated by a tapered fiber tip attached to the hydro-micromanipulator.
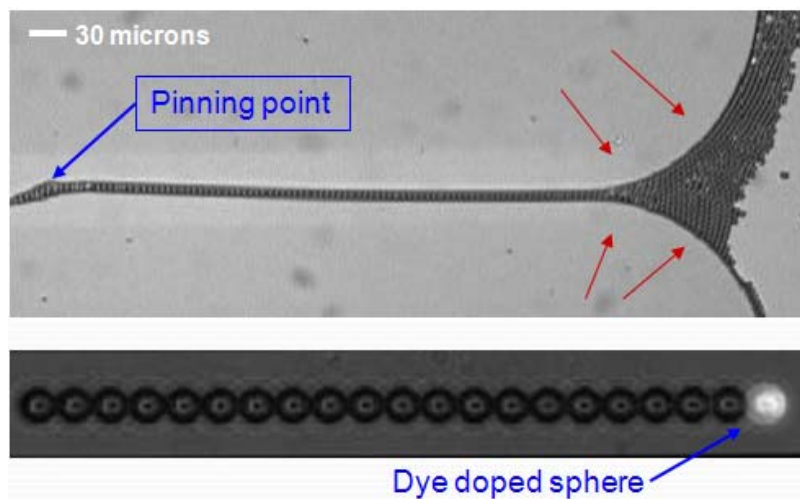
FIGURE 4.5: Optical images of a long straight chain.
A straight chain is assembled from a pinning point (top) and a source sphere is attached to a chain (bottom).

An example of a microsphere chain obtained by self-assembly is illustrated in Figure 4.6. These spheres are coated with gold in order to reduce the charging effect produced by the electron beam in the course of SEM characterization (JEOL Scanning Electron Microscope). The thin gold film with thickness around 150 nm was deposited before the SEM image was taken. There are three parts in this figure: the upper sphere cluster, middle sphere cluster and a straight chain on the bottom. The upper sphere cluster shows the curved edge lines formed as the liquid with spheres dry in the process of the self-assembly. The cluster of spheres in the middle region was broken by the micromanipulation. About 40 spheres are formed a straight chain which is shown in the bottom of Figure 4.6. Also the edge line of the microsphere slide close to the end of the chain is shown. The chains formed by the self-assembly method are fairly straight as seen in Figure 4.6 and all spheres are in touching position as shown in Figure 4.7. This SEM image is taken without the gold coating and therefore the edge of the spheres is slightly smeared out due to the charging effect of SEM.
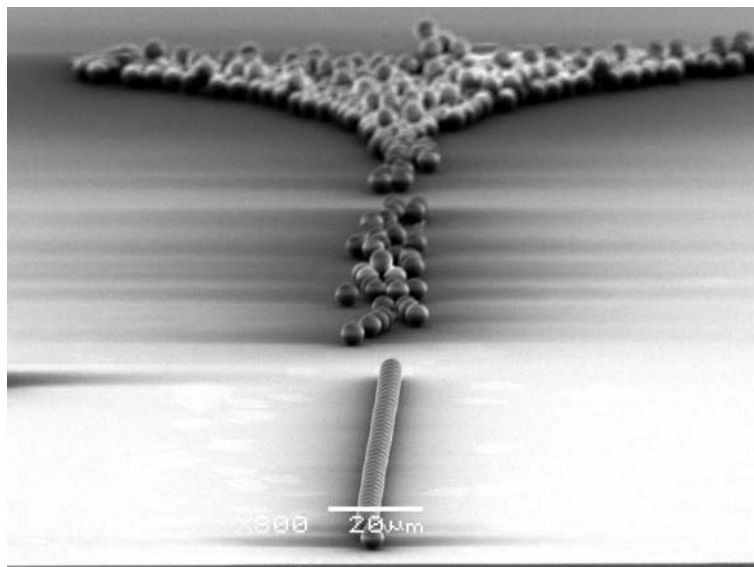
FIGURE 4.6: SEM image of microsphere chain with residual clusters of spheres. Upper part of the image shows the curved edge lines formed by the process of drying of the liquid with spheres.
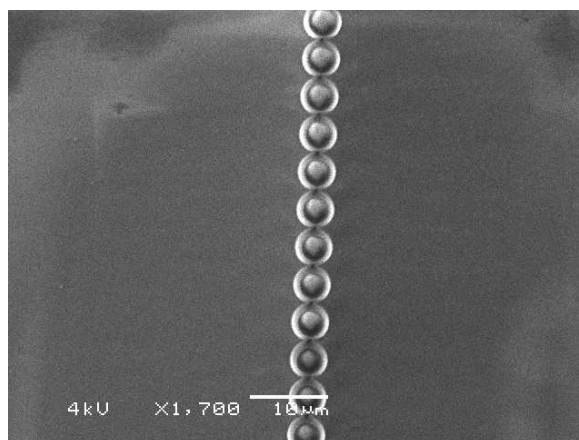
FIGURE 4.7: SEM image of straight microsphere chain without gold coating. They form a straight chain without gaps between the spheres.

In the process of sample preparation we used size-mismatched spheres with about 1-3% variation of sizes. Studies of coupling between size-mismatched spheres are important for developing applications since in commercially available systems of ultrahigh-Q resonators the size variations of the cavities are inevitable. In this work such

coupling phenomena were experimentally studied using one of the spheres as a local source of light and measuring the scattering spectra of EM energy from a chain of passive spheres. In addition, the transmission spectra were measured to investigate the transmission losses for very long chain. The numerical calculation was performed to understand the experimental observations.

4.2.2 Experimental setup

The experimental setup is shown in Figure 4.8 with inverted IX-71 Olympus microscope directly coupled to the imaging spectrometer (Princeton Instruments, Acton Pro 550) through the side entrance slit of the spectrometer.

The image was obtained by the liquid nitrogen cooled CCD camera connected to the spectrometer. In the imaging mode the image of the chain is obtained using the white light illumination aligned with the slit with large width of about 500 μm. Once the chain is aligned well with the slit, the slit width was reduced to 50 or 100 μm allowing the detecting of spectrally and spatially resolved distribution of scattering intensity along the chain. A dye-doped microsphere (Green Fluorescent) with 5.0 μm diameter was used as a source of light. It was attached to one end of the chains using a tapered fiber, as illustrated above the microscope objective in Figure 4.6.

The excitation of the source (green colored sphere) was provided by a Mercury lamp through a band pass filter at the absorption band (460-500 nm) of green FL dye of the source sphere with the intensity well below the threshold for lasing WGMs. Another band pass filter with a transmission window of 500-570 nm between the entrance slit and the objective blocks the pumping band and transmits only FL emission band of microspheres. The source sphere emits very narrow WGMs superimposed at the top of

the broad spectral background determined by the emission band (500-570 nm) of the dye

molecules embedded in the polystyrene microspheres.
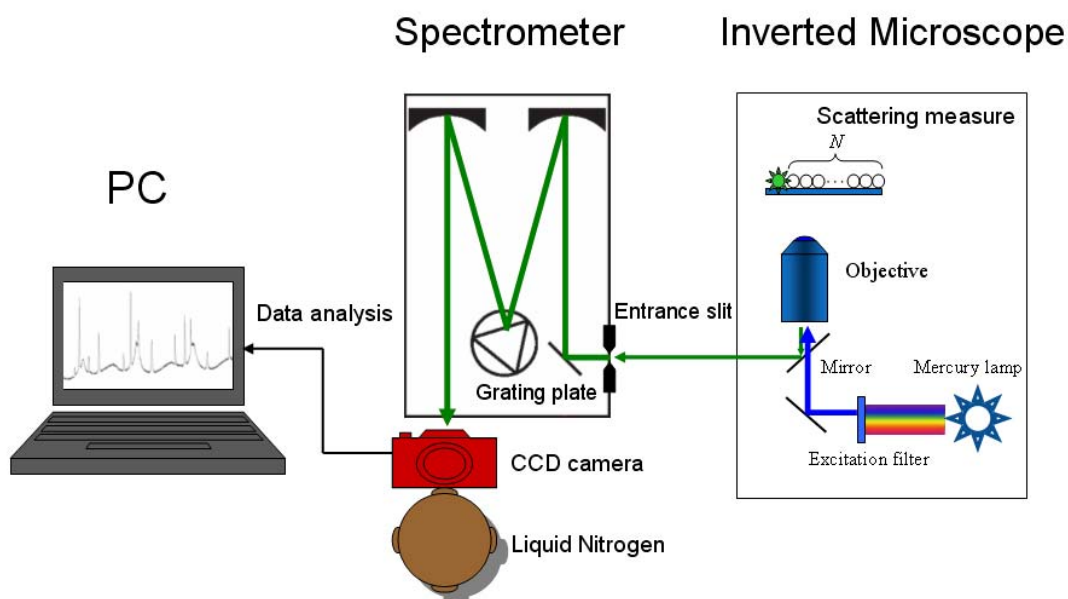
FIGURE 4.8: Experimental setup for scattering measurement.
Inverted microscope is optically coupled to the spectrometer with two gratings (600lines per mm and 1200lines per mm) and a mirror installed at the rotating turret inside the spectrometer. Liquid nitrogen cooled CCD camera with readout dimensions of 2048×512 pixels is used for capturing images or spectral images.

It is important to stress that in this experiment the WGM eigenstates in the source

sphere and the undoped spheres in the chain are all detuned due to random ~1%

variations of the spheres' sizes. The bi-spheres with a similar size disorder show reduced

WGM-based coupling efficiency [88] due to the mismatch in resonant peaks. The sharp

resonant peaks in the source sphere can be perturbed by the neighbor spheres if they have

the WGM peaks which are sufficiently close in energy. However the coupling is expected

to be much more efficient [88] under resonant or close to resonant conditions. If the

eigenstates are strongly detuned the coupling is still possible but with greatly reduced efficiency [88].

4.3 Optical transport measurements

4.3.1 Scattering measurement

In order to investigate optical coupling and transport through chains of size detuned dielectric microspheres, the scattering intensity was measured in two different geometries. One of them has the source sphere separated from the chain of passive spheres. In this case illustrated in Figure 4.9(a) the evanescent coupling is prohibited by large separation of the source sphere from the chain. The source is emitting EM waves with spherical wavefronts, however, because of the significant separation of the source, the waves incident at the end sphere in the chain can be approximated as quasi plane waves. This structure is a very good candidate for the observation of the NIMs in disordered chains of dielectric microspheres.

In the second structure, shown in Figure 4.10(a), the source sphere is attached to the sphere chain formed by undoped spheres. The source sphere in this structure can provide not only the illumination with radiative modes but also an evanescent coupling due to WGMs excited in the source sphere. In this structure, it is possible to observe the resonant optical coupling by means of the quasi-WGMs with perturbed shape predicted [88] by the numerical modeling for size-mismatched bi-spheres.

Figure 4.9 (a) shows the optical image of the first experimental configuration with a separated source which appears in the image as a white sphere due to FL emission. The 16 undoped spheres formed a very straight chain acting as an optical waveguide. It is clearly seen that the source sphere is separated by a 12 μm gap which is larger than two-

sphere distance. This is a sufficiently long separation to avoid evanescent coupling of WGMs from the source sphere into the chain. Usually a separation of about 1-2 microns is sufficient [88] to suppress the mechanisms of evanescent coupling.
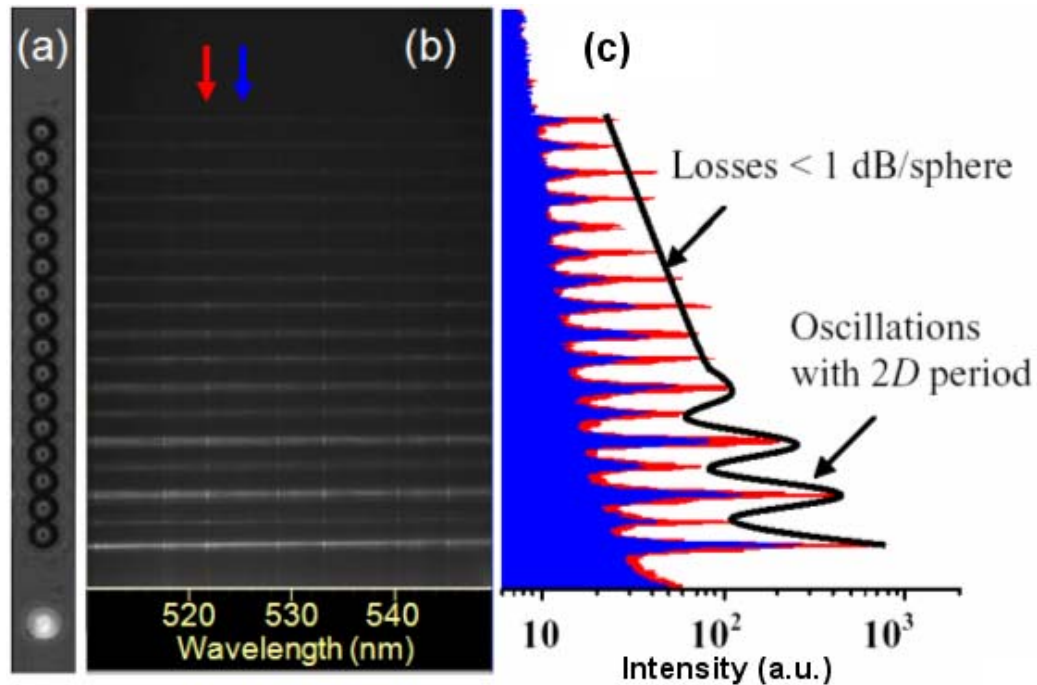
FIGURE 4.9: Spectral response of a chain excited by a separated doped sphere.
(a) A chain of 5 μm spheres and a doped sphere imaged through the slit of the spectrometer, (b) spectrally and spatially resolved distribution of scattering intensity, (c) scattering intensity distribution measured at the 521.5 nm which is the replication of TM^2_{36} WGM peak (red) of the source and at 525.0 nm (blue).

The spectrally and spatially resolved distribution of scattering intensity along the chain is shown in Figure 4.9(b). In this spectral image, the source spectral image is excluded because the scattering intensity of the source is too big compared to the one of the passive sphere chain. The white horizontal stripes in Figure 4.9(b) represent the spectra of scattered light originating from the areas located close to the contact points of spheres. These horizontal stripes with a series of peaks are found to be very similar to the

spectrum of the source sphere with WGMs that were shown in Figure 3.16. The fact that these peaks appear due to WGMs in the source sphere does not play a significant part in the interpretation of the propagation effects in the chain. This is because the WGM peaks can only reach the chain through the scattering effects in the source sphere, so that they propagate in space in the same way as the waves from the fluorescence background region.

It is seen in Figure 4.9(b) that in a few interfaces closer to the source the horizontal stripes show an alternating pattern of larger and smaller intensities along the propagation direction. The horizontal stripes with stronger intensity distributions occur at the odd interfaces starting from the illuminated surface of the first sphere in the chain. This alternation of the intensity distribution can be attributed to the spatial distribution of NIMs in such chains. This will be discussed in more detail in the following section.

The scattering intensity distributions measured at two different wavelengths indicated by the two arrows, the red one at 521.5 nm which is corresponds to the TM_{36}^{2} WGM peak of the source and the blue one at 525.0 nm, are shown in Figure 4.9(c). An additional black line connecting the peaks of spectrum displays the alternating peaks of the scattering intensities in the first few spheres with a period equal to the size of two spheres (10 μm). Both scattering intensity distributions (red and blue) show very similar patterns of peaks with alternating intensity which will be explained in the following section with the numerical simulation results. This means that the propagation of the waves with the wavelengths corresponding to WGMs in the source sphere is very similar to the propagation of the waves emitted as a fluorescent background. In addition, beyond the first decade of spheres the alternating peaks is gradually damped resulting in the small

attenuation (<1dB per sphere) and wavelength independent losses. This is indicative of the formation of NIMs as modes having the smallest propagation losses [90] in disordered systems.

In order to extract light attenuation parameters from the experimental result in Figure 4.9(c), a semi-empirical model based on using an exponent fitting function

$$I = I_0 10^{(-10\beta N)} \tag{4.8}$$

was employed, where I_0 and I are the initial and final intensities, and β is the attenuation levels per individual sphere (in dB), N is the propagation distance expressed in number of spheres [90].

The pattern of the scattering intensities in the first few spheres is different from the previous work [90]. This difference can be related to using much more "plane wave-like" incident beam in the present work compared to the previous experiments [90] where the source of light was created by the local photoexcitation of several dye-doped spheres in such chains. However, after passing through several spheres the attenuation of the scattering intensity peaks observed in this work is similar to that observed in the previous work [90]. The attenuation law is represented by the exponential attenuation with losses < 1 dB/sphere.

In order to achieve an evanescent coupling with the local source, the source sphere is attached to one end of the chain. Figure 4.10(a) shows the image of a chain with a source sphere that is brought into contact with the chain. The source sphere has a broad band FL emission spectrum with the narrow peaks superimposed at the top of this background due to coupling of a fraction of emission to WGMs. After the image of the chain was taken, the slit width was reduced to 50-100 μm allowing the detection of the

spectrally and spatially resolved distribution of scattering intensity along the chain shown

in Figure 4.10(b).
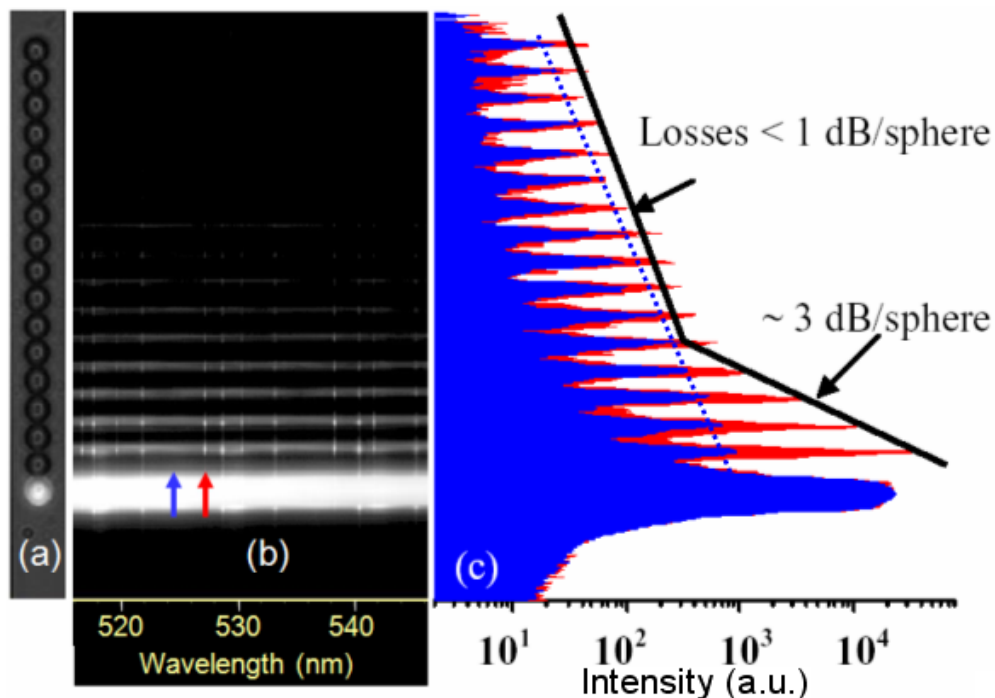
FIGURE 4.10: Spectral response of a chain excited by a doped sphere in contact.
   (a) A chain of 5 μm spheres imaged through the slit of the spectrometer, (b)
   spectrally and spatially resolved distribution of scattering intensity, (c) scattering
   intensity distribution measured at the 527.3 nm which is the TE_{42}^{1} WGM peak
   (red) and at 524.0 nm (blue).

The white horizontal stripes in Figure 4.10(b) represent the spectra of scattered

light originated from the areas located close to the contact points of spheres. The

scattered light has broad spectral composition determined by the emission band (500-570

nm) of the source sphere. A series of WGMs generated in the source sphere is seen due to

bright vertical streaks superimposed on the stripes. The image brightness of the scattering

intensity from the source was adjusted by the square root transfer function [149] to have

better contrast of the spectrum from the spheres located at longer distance from the source.

In order to do the comparative studies of propagation losses in resonant and nonresonant cases, the intensity distribution at two different wavelengths were plotted in Figure 4.10(c). The resonant mode propagation represented in Figure 4.10(c) by the area filled with red was obtained along the chain at 527.3 nm. The red arrow in Figure 4.10(b) corresponds to TE_{42}^1 WGM resonance. The area filled with blue in Figure 4.10(c) illustrates the nonresonant mode propagation at 524.0 nm.

The comparison of the intensity maxima distributions in Figure 4.10(c) reveals striking differences in attenuation of WGMs and nonresonant modes in such chains. It is seen that WGMs are very effectively coupled from the source to the first undoped sphere in the chain. This can be explained by the excitation of WGMs in the equatorial plane of spheres that provides good spatial overlap between the modes in the adjacent spheres. The propagation to the next few spheres in the chain is accompanied with significant attenuation of ~3 dB per sphere. Such substantial attenuation at the frequency of WGM in the source sphere can be explained by the size-mismatch of the spheres leading to detuning of their eigenstates that in its turn leads to scattering losses [88]. After passing through several spheres the attenuation drops to less than 1 dB per sphere level indicating the possibility of mode conversion in the chain. It is also seen that in the case of nonresonant excitation at 524.0 nm the attenuation is close to 1 dB per sphere (blue dotted line) for all spheres including the ones closest to the source sphere.

The interpretation of these results is based on the existence of two mechanisms of coupling between the size-mismatched spheres with detuned eigenstates. In the case of

excitation resonant with WGM at 527.3 nm in the source sphere we provide conditions for excitation of "forced oscillations" in series of detuned cavities due to strong evanescent field created in the source sphere. These "forced oscillations" are represented by quasi-WGMs with perturbed shape predicted [88] in previous work by the numerical modeling. The efficiency of such coupling mechanism is typically limited by 20-30 % in reasonable agreement with ~3 dB/sphere attenuation observed in this work. Similar losses were observed in experiments [87] with excitation above the threshold for lasing WGMs. The size-mismatched spheres with their gap controlled have shown [89] very similar values of efficiency of coupling.

In the case of excitation away from WGM resonance in the source sphere (524.0 nm) the coupling is provided due to radiative modes emitted by the source sphere. The chain of cavities operates as a series of radiatively coupled microlenses. In the latter case each sphere produces a focused spot termed "photonic nanojet" [93] with elongated shape and subwavelength lateral size. This mechanism leads to formation of quasi-periodic NIMs due to geometrical lens effect of each microsphere. In this case we prove that NIMs can be excited in chains of cavities under nonresonant conditions.

4.3.2 Transmission measurement

The optical transport in a size-disordered chain is more directly measured by collecting the transmitted light through the chain which is 90 degree rotated in the microscope setup compared to the scattering measurement geometries. These transmission intensity measurements for the extremely long (88 spheres) chains are preferable due to the fact that they represent attenuation properties of the chains more directly compared to the scattering measurements. The experimental setup and the image

of the chain with a doped source sphere are shown in Figure 4.11(a). In contrast to the scattering intensity measurement, the microscope objective collects the light from the end sphere in the chain.

The photoexcitation is provided at the end of the chain through the same objective. The source sphere located at the other end of the chain was photoexcited by the pump beam with the spectrum corresponding to the absorption band (460-500 nm) of green FL dye of the source sphere. It should be noticed that there is a propagation loss for the pump beam that was transmitted through the chain. When the dye FL source was excited by the pump beam, the FL emission at 500 - 570 nm experiences similar losses as the pump beam on a way back from FL microspheres to the collection optics focused at the end sphere in the chains. Thus, this structure behaves as a double pass optical waveguide system. The losses take place for each direction of propagation. For the pump beam the losses occur for a single pass from the first illuminated sphere up to the dye-doped source sphere. This means that the pumping is effectively stronger for shorter chains. For the FL emission propagating in a backward direction the losses occur all the way from the source sphere down to the end sphere in the chain imaged at the slit of the spectrometer.
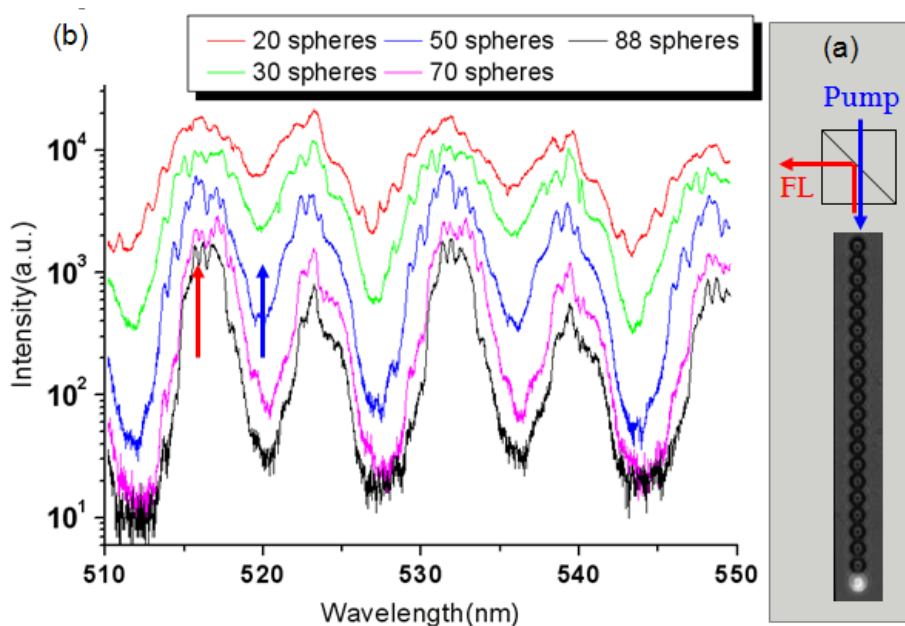
FIGURE 4.11: Spectral transport of a long chain.
(a) experimental setup and the image of the chain with source sphere, (b) spectral band structure for different number of spheres.

In order to investigate the propagation losses by the direct measurement of transmission, a small number of spheres close to the source sphere were removed by the tapered fiber stick controlled by the hydraulic micromanipulators. After that, the same source sphere was reattached to the end sphere in the chain to measure the transmission intensity for the shorter chain. Different spectra in Figure 4.11(b) were obtained from the shorter chains that were illuminated by the same excited FL source. Since we used the same spheres for the shorter chains, the source of light has identical spectral properties for chains with various lengths.

The main observation in Figure 4.11(b) is that the transmission spectrum shows the periodical modulation in the broadband spectral responses with the same period for different lengths of the chain. The interference fringes over the broad spectral range begin to appear for the chains with a length about 20 spheres. This chain produced the smallest

modulation magnitude among the spectral lines in Fig 4.11(b). Chains with larger lengths caused more distinct modulation, and the modulation magnitude became larger in spite the fact that the total power is reduced. The peaks (pass bands) and the valleys (stop bands) have different attenuation as a function of the number of spheres.

The spacing $\Delta\lambda$ between maxima of transmission is inversely proportional [150] to the separation of the cavity from the equation:

$$\Delta\lambda = \lambda^2 / 2nd .$$ (4.9)

The period of the fringes is approximately 8.5 nm which is quite small for the cavities with cavity separation of 5 μm. The period of fringes of 8.5 nm corresponds to the cavity width of 10.4 μm from Eq. (4.9), which is close to the size of the double sphere cavity. This means that the chain with 5 μm spheres possess 2D periodicity of spatial distributions of NIMs. This requires more theoretical studies that will be discussed in the subsequent section

In order to perform comparative studies of propagation losses, we plotted the intensity curves for the stop bands and the pass bands with respect to the number of spheres in the chain. Two arrows of red (pass band) and blue (stop band) shown in Figure 4.11(b) indicate the wavelengths at 516 and 520 nm, respectively, in which the propagation intensities were taken for the plot presented in Figure 4.12. The propagation intensity curves (solid lines) and their linear fits (dotted line) for the two wavelengths (516 and 520 nm) were plotted in Figure 4.12 as a function of the number of spheres. An estimate of the attenuation per sphere (β) was obtained by employing a semiempirical exponential fitting function (Eq. 4.8), $I = I_0 10^{(-10\beta 2N)}$, where the length of the chain was assumed to be 2N due to the double pass geometry of our experiments. This function

provides a good fit to the experimental data with $\beta = 0.08$ dB per sphere in the pass band (red) and $\beta = 0.17$ dB per sphere in the stop band (blue) of Fabry-Perot fringes, as shown by the straight lines in Figure 4.12. In spite of the fact that the pass bands have smaller propagation losses compared to the stop bands, the propagation losses for the two bands covering the broad spectral range are fairly small, that is, less than 0.2 dB/sphere.
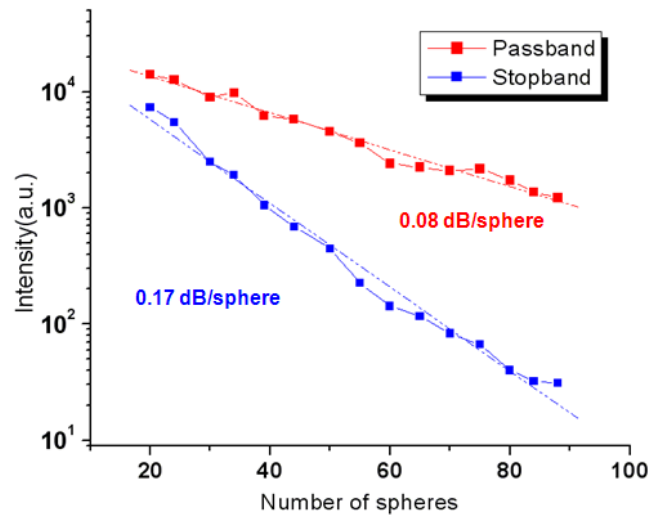
FIGURE 4.12: Transport curves of the passband (red) and the stopband (blue).

This level of attenuation is much smaller than that observed previously [90] in shorter chains with the length limited by approximately 20 spheres. In this work [90] the losses were also observed to gradually reduce along the chain, but the smallest values of attenuation were observed to be about 0.5 dB/sphere. The fact that in this work we observed smaller losses can be explained by using much longer chains (up to 100 cavities). We show that in such long chains the losses continue to decay in the course of propagation along the chain. This surprising result means that the propagation mechanism

in the region located deeply inside the chain, where the NIMs are dominant, is very efficient.

Another observation from the transmission measurement is that the loss of 0.08dB/sphere is much smaller than the losses of less than 1dB/sphere of NIMs propagation in shorter chains shown in Figure 4.9 and 4.10. This big difference is related to the illumination methods to the microsphere chains. A dye doped microsphere is a spherical source whose size is very similar to the sizes of the spheres in the chain. This dye doped microsphere source is very different from the plane wave illumination from a laser source. Due to this poor illumination from a spherical source, the losses in spheres close to the source are larger than the losses in spheres in much longer chains where the NIMs are dominant. This also requires more theoretical considerations with numerical simulations that will be described in the following section.

4.4 Numerical calculation

The numerical three-dimensional FDTD modeling [135] of the EM wave propagation was performed to understand how the photonic nanojets behave in a chain. In this work, the chain contains five identical 5 μm spheres with n = 1.59. A continuous plane wave with λ = 530.0 nm was incident from the left along the axis of the chain as shown in Figure 4.13(a). This modeling was performed with very limited spatial resolution of $\lambda/8$ since we did not pursue the task of obtaining high resolution field distributions, but rather wanted to estimate the spatial period of these distributions. The run time (stop time) was 500 cT which is long enough for the EM wave to propagate the whole chain one time. The calculation area was 6.1 $\times$ 6.1 $\times$ 25.1 μm in x, y, and z dimension which requires the estimated memory size (966.2 MB). This factor limited the

resolution of the calculation. In spite of this limited resolution, this modeling gives a good insight into the properties of the photonic nanojets in a chain.

The EM amplitude map in the equatorial plane of spheres demonstrates 2*D* periodicity of the photonic nanojets. This 2D periodicity can be explained by small reflections (~5%) of the photonic nanojets in the spheres' contact areas in every two spheres along the axis of the chain. This small reflection leads to the formation of Fabry-Perot fringes with separation between the two maxima, $\Delta\lambda = \lambda^2 / 2dn$, where *d* is the length of the cavities. This formula provides a good fit to the experimental transmission data in Figure 4.11 (b) using *d* = 10.4 *μ*m that well agrees with the 2*D* periodicity of nanojets.
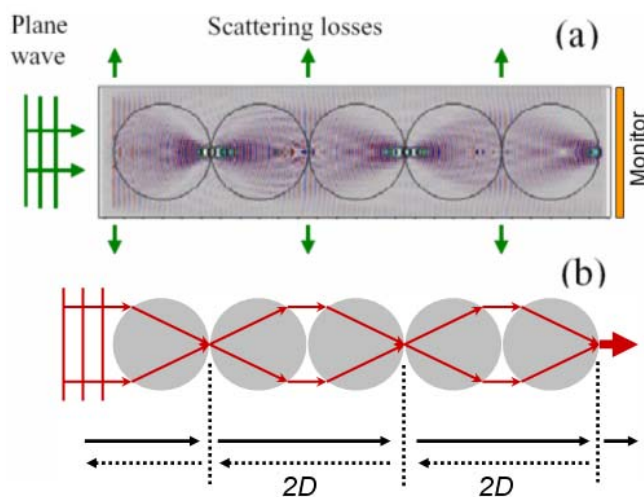
FIGURE 4.13: Theoretical model of light propagation in a microsphere chain.
(a) Calculated EM amplitude distribution with plane wave incident at λ = 530.0 nm. (b) Geometrical optics model of periodically coupled lenses with 2*D* period.

The scattering losses along the chain are localized in the areas between the nanojets where the beam is expanded, as shown in Figure 4.13 (a). These locations are found to coincide with the positions of the dominating scattering peaks with the 2*D* period in Figure 4.9 (c) detected in the first few spheres illuminated by the separated

source sphere. The fact that beyond the first decade of spheres the alternating peaks of scattering intensity with the 2D period are found to be damped in Figure 4.9 (c) can be explained by the gradual excitation of a second fundamental NIM shifted by D. In real physical chains of spheres such NIMs shifted by half a period can be coupled due to disorder-induced scattering.

A schematic diagram of the geometrical optics model, shown in Figure 4.13(b), shows that the first sphere focuses light to a spot located close to the contact point with the second sphere. The second sphere expands the beam so it propagates as a collimated beam from the second to third sphere. Because the expanded beam between the second and third sphere makes large incident angle to the third sphere, some fraction of the beam intensity is reflected by the third sphere out of axis of the chain. This introduces the propagation losses for NIMs. The third sphere focuses the light again, and the process repeats along the chain with the periodicity equal to the size of two spheres.

In order to investigate the spot size at the output sphere, the distribution of the electromagnetic field was calculated in the vicinity of the end sphere in the chain as shown in Figure 4.14. The large size of the computational grid prevents performing precise measurements of the last photonic nanojet. However the presence of such nanojet in close vicinity to the surface of the end sphere is clearly seen in Figure 4.14.
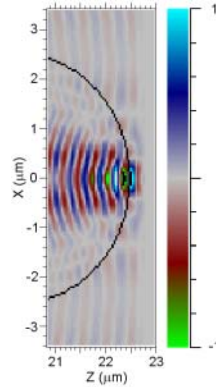
FIGURE 4.14: Magnified field distribution at the output sphere.

In order to investigate the interference fringe patterns in the transmission spectra, the spectral response of the chain excited from the left by a plane wave with broadband pulse with ramp/pulse time of 5 cT (0.17 ns) was calculated. A built-in time monitor whose size is $5 \times 5 \times 0$ in x, y, and z dimension in 3D FDTD modeling [135] is located close to the surface of the end sphere to measure the temporal response through the chain, as shown in Figure 4.13(a).

The Fourier transform of the temporal response obtained from the time monitor was performed by using a built-in option in RSoft to generate the spectrum that is shown in Figure 4.15. For the wavelength range between 510 and 550 nm, the same as the experimental result, the calculated spectrum consists of 5 fringes which is the same number of fringes as in Figure 4.11(b). The numerical simulation for the chain with only 5 identical spheres generated a similar spectral power distribution to the experimental result. This preliminary calculation result compares only the number of the fringes due to the limited capability of calculation resources. Further investigation on a chain with comparable number of spheres is required in future work.
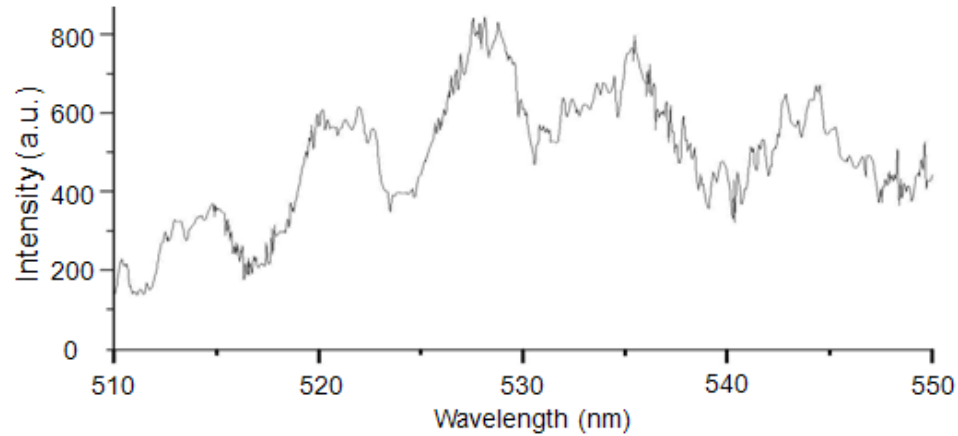
FIGURE 4.15: Spectral response of the local monitor at the end microsphere. The built-in source excited a broadband pulse with ramp/pulse time of 5 cT (0.17 ns).

A good agreement with the experiment can be explained by taking into account that the geometrical model in Figure 4.13 (b) correctly represents the period of the actual field distribution in Figure 4.13 (a). As mentioned before, the microsphere chain is composed of the multiple building blocks of a Fabry-Perot cavity. The cavity interfaces can be identified with the touching points between the spheres where we have photonic nanojets. Due to the small reflections in the forward and backward directions in these areas, the propagation along the axis of the chain can be associated with the light passing through a sequence of coupled Fabry-Perot filters. Since the separation between nanojets is equal to two spheres the effective thickness of Fabry-Perot filters is equal to the size of two spheres.

4.5 Conclusions

In this Chapter, we experimentally investigated the two different mechanisms of light transport in chains of spheres, transport due to coupling between WGMs and the NIMs coupling, for the size detuned chains of coupled spherical cavities. The coupling

between WGMs is shown to have a reduced efficiency due to size-disorder of constituting spheres. The attenuation for such coupling has a typical magnitude of ~3dB/sphere in the first few spheres adjacent to the source of light. The mechanism of the WGM-based coupling can be associated with excitation of quasi-WGMs with perturbed shape which have been described [88] in previous numerical studies of coupling between size-mismatched spheres. This result was found to be consistent with previous experimental studies [90] of propagation losses in such disordered chains as well as with the modeling results performed for size-mismatched bispheres [88].

As the optical field propagates beyond the region in which the quasi-WGMs are dominant, which is typically only few spheres long, the coupling and the propagation phenomena are ruled by the NIMs which are quite robust to the size disorder. This happens due to small propagation losses for NIMs compared to WGM-based coupling. This interesting interplay between NIMs and WGM-based propagation was observed for the first time in this work.

Previous measurements of attenuation of NIMs showed [90] that the maximal scattering losses occurred in the first few spheres adjacent to the source of light. After that the attenuation has been shown to drop to ~0.5 dB/sphere. This has been demonstrated for relatively short chains with total number of spheres below 20. In this work we showed that beyond the first 20 spheres the attenuation continue to decrease reaching an extremely small values such as 0.08dB/sphere in the pass bands and 0.017 dB/sphere in the stop bands. We associate this level of loss with the inevitable out-of-axis scattering of light at the interfaces of the spheres between the photonic nanojets. Such

scattering takes place even for perfectly periodic structures formed by identical spheres, and for this reason it can be associated with fundamental scattering losses for NIMs.

The geometrical model of the infinite/infinite conjugate system allows a simple understanding of the spatial periodicity of photonic nanojets based on the assumption that the focusing length of polystyrene microspherical lenses is close to the radius of the spheres. More rigorous understanding of NIM properties was developed due to numerical 3D FDTD modeling of the propagation effects. The results of this numerical modeling were found to be in a good agreement with the experimental measurements.

This small propagation loss of NIMs can be used in transporting the optical power in a straight microsphere chain with small spot size at the output. The mode conversion in size disorder chain can convert multimodal input beams into a photonic nanojet at the end of the chain. This small spot size can be useful in the medical area and sensor area.

CHAPTER 5: SUMMARY AND FUTURE DIRECTIONS

In this thesis, we investigate spatial and spectral mode profiles and their optical transport properties in single and multiple coupled cavities. In the first part of the thesis some advantages of whispering gallery modes (WGMs) along the circumference of the micropillars are illustrated and compared to photonic dot states located in the middle of the pillars. We observed high quality (Q up to 20 000) WGMs with small mode volumes V ~0.3 μm^3 in 4-5 μm Al(Ga)As/GaAs micropillars. We showed that WGMs provide at least two times larger values of the figure of merit $Q/\sqrt{V}$ for strong coupling applications compared to photonic dot states in pillars with comparable size. Soon after publishing our results, much higher Q-factors ($>10^5$) have been observed for photonics dot states [140]. However, the results on WGMs in micropillars have also been improved (Q>60000) [Private communication, A.M. Fox 2008]. The future direction of this research is connected with studies on the effects of strong coupling between microcavity modes and individual quantum dots in such micropillars.

The second, and major, direction of this thesis is the spectroscopic characterization of the optical transport and coupling in bi-spheres and sphere chains. For the size-matched bispheres, normal mode splitting (NMS) of resonant optical modes is investigated experimentally in fluorescence from dye-doped polymer bi-spheres with diameters from 2.9 to 10μm. Various orientation of the spectrometer slit with respect to the axis of bi-sphere reveals the mode splitting as a function of sphere size, polarization,

and all three mode numbers (*l, m, n*). In these studies we selected bi-spheres on a substrate as the simplest building block of more complicates systems. Our results show that the coupling between the fundamental modes in such systems is sufficiently strong, so that these structures can be created with small propagation losses and controllable dispersions for photons. Our techniques of size-sorting of microspheres provided extremely high uniformity of spheres ~0.03%. Developing this technology in the future will require developing more efficient techniques of sorting supermonodispersive spheres such as methods [151] based on using radiative pressure effects or using microfludic control of spheres with spectroscopic monitering.

In the size detuned sphere chains, non-resonant coupling by photonic nanojets provides good optical transport mechanism due to periodical focusing of light in such chains. In the transmission spectra of long (>20 spheres) chains we observed Fabry-Pérot fringes with propagation losses of only 0.08dB per sphere in the maxima of transmission peaks. Due to mechanical robustness, tight focusing of the beam, high optical throughput, and broad spectral transmission properties, such chains can be used in a variety of biomedical applications such as optical microprobes with subwavelength spatial resolution. In addition, the mode conversion process in size detuned systems can be very useful in sensor applications. Some properties of these modes still require further studies, such as the robustness of these modes to the size and positional disorder of the microspheres. Another interesting problem is connected with the influence of the external medium such as a liquid or a biological tissue on the quality of focusing of such microprobes. These properties will be investigated in future work.

REFERENCES

[1]   O. Painter, R. K. Lee, A. Scherer, A. Yariv, J. D. O'Brien, P. D. Dapkus, and I. Kim, 1999, Two-Dimensional Photonic Band-Gap Defect Mode Laser, Science, Vol. 284, 1819.

[2]   David M. Pustal, Ahmed Sharkawy, Shouyuan Shi, and Dennis W. Prather,Tunable Photonic crystal microcavities, Applied Optics, Vol. 41, No. 26, 5574.

[3]   Y. Akahane, T. Asano, B. -S. Song, and S. Noda, 2003, High-Q photonic nanocavity in a tow-dimensional photonic crystal, Nature, Vol. 425, 944.

[4]   T. Yoshie, A. Scherer, J. Hendrickson, G. Khitrova, H. M. Gibbs, G. Rupper, C. Ell, O. B. Shchekin, and D. G. Deppe, 2004, Vacuum Rabi splitting with a single quantum dot in a photonic crystal nanocavity, Nature, Vol. 432, 200.

[5]   K. Hennessy, A. Badolato, M. Winger, D. Gerace, M. Atatüre, S. Gulde, S. Fält, E. L. Hu, and A. Imamoğlu, 2007, Quantum nature of a strongly-coupled single quantum dot-cavity system, Nature, Vol. 445, 896.

[6]   J. Vučković, M. Lončar, H. Mabuchi, and A. Scherer, 2001, Design of   photonic crystal microcavities for cavity QED, Physical Review E. Vol. 65, 016608.

[7]   S. Frédérick, D. Dalacu, J. Lapointe, P. J. Poole, G. C. Aers, and R. L. Williams, 2006, Experimental demonstration of high quality factor, x-dipole modes in InAs/InP quantum dot photonic crystal microcavity membranes, Applied Physics Letters, 89, 091115.

[8]   Edo Waks and Jelena Vuckovic, 2005, Coupled mode theory for photonic crystal-waveguide interaction, Optics Express, Vol. 13, No. 13, 5064.

[9]   C. Weisbuch, M. Nishioka, A. Ishikawa, and Y. Arakawa, 1992, Observation of the Coupled Excition-Photon Mode Splitting in a Semiconductor Quantum Microcavity, Physical Review Letters, Vol. 69, No. 23, 33 14.

[10]   V. Savona, F. Tassone, C. Piermarocchi, A. Quattropani, and P. Schwendimann, 1996, theory of polariton photoluminescence in arbitrary semiconductor microcavity structures, Physical Review B, Vol. 53, No. 19, 13 051

[11]   V. N. Astratov, S. Yang, S. Lam, B. D. Jones, D. Sanvitto, D. M. Whittaker, A. M. Fox, M. S. Skolnick, A. Tahraoui, P. W. Fry, and M. Hopkinson, 2007, Whispering gallery resonances in semiconductor micropillars, Applied Physics Letters, Vol. 91, 07115.

[12] J. M. Gérard, D. Barrier, J. Y. Marzin, R. Kuszelewichz, L. Manin, E. Costard, V. ThierryMieg, and T. Rivera, 1996, Quantum boxes as active probes for photonic microstructures: The pillar microcavity case, Applied Physics Letters, Vol. 69, 449.

[13] L. C. Andreani and G. Panzarini, 1999, Strong-coupling regime for quantum boxes in pillar microcavities: Theory, Physical Review B, Vol. 60, No. 19, 13267.

[14] J. P. Reithmaier, M. Röhner, H. Zull, F. Schäfer, A. Forchel, P. A. Knipp, and T. L. Reinecke, 1997, Size Dependence of Confined Optical Modes in Photonic Quantum dots, Physical Review Letters, Vol. 78, No. 2, 378.

[15] D. M. Whittaker, P. S. S. Guimaraes, D. Sanvitto, H. Vinck, S. Lam, A. Daraei, J. A. Timpson, A. M. Fox, M. S. Skolnick, Y.-L. D. Ho, J. G. Rarity, M. Hopkinson, and A. Tahraoui, 2007, High Q modes in elliptical microcavity pillars, Applied Physics Letters, Vol. 90, 161105.

[16] D. Sanvitto, A. Daraei, A. Tahraoui, M. Hopkinson, P. W. Fry, D. M. Whittaker, and M. S. Skolnick, 2005, Observation of ultrahigh quality factor in a semiconductor microcavity, Applied Physics Letters, Vol. 86, 191109.

[17] J. P. Reithmaier, G. Sęk, A. Löffler, C. Hofmann, S. Kuhn, S. Reitzenstein, L. V. Keldysh, V. D. Kulakovskii, T. L. Reinecke, and A. Forchel, 2004, Strong coupling in a single quantum dot-semiconductor microcavity system, Nature, Vol. 432, 197.

[18] S. Reitzenstein, A. Bazhenov, A. Gorbunov, C. Hofmann, S. Münch, A. Löffler, M. Kamp, J. P. Reithmaier, V. D. Kulakovskii, and A. Forchel, 2006, Lasing in high-Q quantum-dot micropillar cavities, Applied Physics Letters, Vol. 89, 051107.

[19] S. Reitzenstein, C. Hofmann, A. Gorbunov, M. Strauß, S. H. Kwon, C. Schneider, A. Löffler, S. Höfling, M. Kamp, and A. Forchel, 2007, AlAs/GaAs Micropillar cavities with quality factors exceeding 150,000, Applied Physics Letters, Vol. 90, 251109.

[20] G. Lecamp, J. P. Hugonin, P. Lalanne, R. Braive, S. Varoutsis, S. Laurent, A. Lemaître, I. Sagnes, G. Patriarche, I. Robert-Philip, and I. Abram, 2007, Submicron-diameter semiconductor pillar microcavities with very high quality factors, Applied Physics Letters, Vol. 90, 091120.

[21] N. Gregersen, T. R. Neilsen, B. Tromborg, and J. Mørk, 2007, Quality factors of nonideal micro pillars, Applied physics Letters, Vol. 91, 011116.

[22]   D. Bajoni, E. Peter, P. Senellart, J. L. Smirr, I. Sagnes, A. Lemaître, and J. Bloch, 2007, Polariton parametric luminescence in a single micropillar, Applied Physics Letters, Vol. 90, 051107.

[23]   S. L. McCall, A. F. J. Levi, R. E. Slusher, S. J. Pearton, and R. A. Logan, 1992, Whispering-gallery mode microdisk lasers, Applied Physics Letters, Vol. 60, 289.

[24]   M. K. Chin, D. Y. Chu, and S. -T. Ho, 1994, Estimation of the spontaneous emission factor for microdisk lasers via the approximation of whispering gallery modes, J. Appl. Phys. 75(7), 3302

[25]   B. Gayral, J. M. Gérard, A. Lemaître, C. Dupuis, L. Manin, and J. L. Pelouard, 1999, High-Q wet-etched GaAs microdisks containing InAs quantum boxes, Applied Physics Letters, Vol. 75, 1908.

[26]   E. Peter, P. Senellart, D. Martrou, A. Lemaître, J. Hours, J. M. Gérard, and J. Bloch, 2005, Exciton-photon strong-coupling regime for a single quantum dot embedded in a microcavity, Physics Review Letters, Vol. 95 (6), 067401.

[27]   M. Borselli, T. J. Johnson, and O. Painter, 2005, Beyond the Rayleigh scattering limit in high-Q silicon microdisks: theory and experiment, Optics Express, Vol. 13, No. 5, 1515.

[28]   K. Srinivasan, M. Borselli, and O. Painter, A. Stintz, and S. Krishna, 2006, Cavity Q, mode volume, and lasing threshold in small diameter AlGaAs microdisks with embedded quantum dots, Optics Express, Vol. 14, No. 3, 1094.

[29]   P. E. Barclay, K. Srinivasan, and O. Painter, 2006, Integration of fiber-coupled high-Q SiN_x microdisks with atom chips, Applied Physics Letters, Vol. 89, 131108.

[30]   Mark Oxborrow, 2007, Traceable 2D finite-element simulation of the whispering-gallery modes of axisymmetric electromagnetic resonators, Quantum Physics, preprint arXiv:quant-ph/0611099.

[31]   E. Peter, J. Bloch, D. Martrou, A. lemaître, J. Hours, G. Patriarche, A. Cavanna, J. M. Gérard, S. Laurent, I. Robert-Philip, P. Senellart, 2006, Cavity QED with a single QD inside an Optical Microcavity, Phys. Stat. Sol. (b), Vol. 243, No. 15, 3879.

[32]   B. E. Little, S. T. Chu, H, A. Haus, J. Foresi, and J.-P. Laine, 1997, Microring resonator channel dropping filters, Journal of Lightwave Technology. Vol. 15, 998.

[33]   B. Liu, A. Shakouri, and J. E. Bowers, 2001, Passive microring-resonator-coupled lasers, Applied Physics Letters, Vol. 79, No. 22, 3561.

[34] L. Martinez, and M. Lipson, 2006, High confinement suspended micro-ring resonators in silicon-on-insulator, Optics Express, Vol. 14, No. 13, 6259.

[35] C.-S. Ma, Y. -Z. Xu, X. Yan, Z.-K. Qin, and X.-Y. Wang, 2005, Effect of ring spacing on spectral response of parallel-cascaded microring resonator arrays, Optical and Quantum Electronics, Vol. 37, 561.

[36] L. Zhou and A. W. Poon, 2006, Electrically reconfigurable silicon microring resonator-based filter with waveguide-coupled feedback, Optics Express, Vol. 15, No. 15, 9194.

[37] B. Miao, P. Yao, J. Murakowski, D. W. Parther, 2005, Fabrication of silicon microring resonators with narrow coupling gaps, J. Microlith., Microfab., Microsyst., Vol. 4, 023013.

[38] T. Barwicz, M. A. Popović, P. T. Rakich, M. R. Watts, H. A. Haus, E. P. Ippen, and H. I. Smith, 2004, Microring-resonator-based add-drop filters in SiN: fabrication and analysis, Optics Express, Vol. 12, No. 7, 1437.

[39] I. M. White, J. D. Suter, H. Oveys, X. Fan, 2007, Universal coupling between metal-clad waveguides and optical ring resonators, Optics Express, Vol. 15, No. 2, 646.

[40] D. K. Armani, T. M. Kippenberg, S. M. Spillane, and K. J. Vahala, 2003, Ultra-high-Q toroid microcavity on a chip, Nature, Vol. 421, 925.

[41] T. R. O'meara, 1962, The Optimum Design of the Toroidal Resonator, IRE Transactions on Component Parts, 115.

[42] T. Aoki, B. Dayan, E. Wilcut, W. P. Bowen, A. S. Parkins, T. J. Kippenberg, K. J. Vahala, and H. J. Kimble, 2006, Observation of strong coupling between one atom and a monolithic microresonator, Nature, Vol. 443, 671.

[43] C. G. B. Garrett, W. Kaiser, and W. L. Bond, 1961, Stimulated Emission into Optical Whispering Modes of Spheres, Physical Review, Vol. 124, No. 6, 1807.

[44] K. Kieu and M. Mansuripur, 2007, Fiber laser using a microsphere resonator as a feedback element, Optics Letters, Vol. 32, No. 3, 244.

[45] V. S. Ilchenko, M. L. Gorodetsky, and S. P. Vyatchanin, 1993, Coupling and tunability of optical whispering-gallery modes: a basis for coordinate meter, Optics Communications, Vol. 107, 41.

[46] L.Collot, V.Lefèvre-Seguin, M.Brune, J.M.Raimond and S.Haroche, 1993, Very high Q whispering gallery mode resonances observed on fused silica microspheres, Euro. Phys. Lett, Vol. 23, 327.

[47]   M. L. Gorodetsky, A. A. Savchenkov, and V. S. Ilchenko, 1996, Ultimate Q of optical microsphere resonators, Optics Letters, Vol. 21, No. 7, 453.

[48]   D. W. Vernooy, V. S. Ilchenko, H. Mabuchi, E. W. Streed, and H. J. Kimble, 1998, High-Q measurements of fused-silica microspheres in the near infrared, Optics Letters, Vol. 23, No. 4, 247.

[49]   Valerie Lefevre-Seguin, 1999, Whispering-gallery mode lasers with doped silica microspheres, Optical materials, Vol. 11, 153.

[50]   H. Mabuchi and H. J. Kimble, 1994, Atom galleries for whispering atoms: binding atoms in stable orbits around an optical resonator, Optics Letters, Vol. 19, 749.

[51]   F. Treussart, J. Hare, L. Collot, V. Lef `evre, D. S.Weiss, V. Sandoghdar, J. M. Raimond, and S. Haroche, 1994, Splitting of high-Q Mie modes induced by light backscattering in silica microspheres, Optics Letters, Vol. 19, 1651.

[52]   A. B. Matsko and V. S. Ilchenko, 2006, Optical Resonators With Whispering-Gallery Modes − Part I: Basics, IEEE Journal of Selected Topics in Quantum Electronics, Vol. 12, No. 1, 3.

[53]   V. S. Ilchenko and A. B. Matsko, 2006, Optical Resonators with Whispering-Gallery Modes − Part II: Applications, IEEE Journal of Selected Topics in Quantum Electronics, Vol. 12, No. 1, 15.

[54]   S. Götzinger, S. Demmerer, O. Benson, and V. Sandoghdar, 2001, Mapping and manipulating whispering gallery modes of microsphere resonator with a near-field probe, Journal of Microscopy, Vol. 202, 117.

[55]   G. Griffel, S. Arnold, D. Taskent, and A. Serpengüzel, J. Connolly, and N. Morris, 1996, Morphology-dependent resonances of a microsphere-optical fiber system, Optics Letters, Vol. 21, No. 10, 695.

[56]   N. L. Thomas, U. Woggon, W. Langbein, and M. V. Artemyev, 2006, Effect of a dielectric substrate on whispering-gallery-mode sensors, J. Opt. Soc. Am. B, Vol. 23, No. 11, 2361.

[57]   B. Möller, M. V. Artemyev, and U. Woggen, 2002, Mode identification in spherical microcavities doped with quantum dots, Applied Physics Letters, Vol. 80, No. 18, 3253.

[58]   B. Möller, U. Woggon, M. V. Artemyev, and R. Wannemacher, 2003, Mode control by nanoengineering light emitters in spherical microcavities, Applied Physics Letters, Vol. 83, No. 13, 2686.

[59] M. V. Artemyev, U. Woggon, R. Wannemacher, H. Jachinski, and W. Langbein, 2001, Light trapped in a Photonic Dot: Microspheres Act as a Cavity for Quantum Dot Emission, Nano Letters, Vol. 1, No. 6, 309.

[60] J. C. Knight, N. Dubreuil, V. Sandoghdar, J. Hare, V. Lefèvre-Seguin, J. M. Raimond, and S. Haroche, 1995, Mapping whispering-gallery-modes in microspheres with a near-field probe, Optics Letters, Vol. 20, No. 14, 1515.

[61] M. Fujii, M. Haraguchi, T. Okamoto, and M. Fukui, 2005, Characteristics of Whispering Gallery Modes in a Single Spheroid: Dependence on the Direction of Incident Light, Journal of the Korean Physical Society, Vol. 47, S38.

[62] Y.-S. Park, A. K. Cook, and H. Wang, 2006, Cavity QED with Diamond Nanocrystals and Silica Microspheres, Nano Letters, Vol. 6, No. 9, 2075.

[63] J. P. Rezac and A. T. Rosenberger, 2001, Locking a microsphere whispering-gallery mode to a laser, Optics Express, Vol. 8, No. 11, 605.

[64] Y. Panitchob, G. S. Murugan, M. N. Zervas, P. Horak, S. Berneschi, S. Pelli, G. N. Conti, and J. S. Wilkinson, 2008, Whispering gallery mode spectra of channel waveguide coupled microspheres, Optics Express, Vol. 16, No. 15, 11066.

[65] Y. P. Rakovich, L. Yang, E. M. McCabe, J. F. Donegan, T. Perova, A. Moore, N. Gaponik, and A. Rogach, 2003, Whispering gallery mode emission from a composite system of CdTe nanocrystals and a spherical microcavity, Semiconductor Science and Technology, Vol. 18, 914.

[66] C. Arnaud, M. Boustimi, and P. Féron, 2004, Wavelength shifts in Erbium doped glass microspherical Whispering Gallery Mode lasers, International Workshop on Photonics and Applications, Hanoi, Vietnam, 209.

[67] R. Symes, R. M. Sayer and J. P. Reid, 2004, Cavity enhanced droplet spectroscopy: Principle, perspectives and prospects, Phys. Chem. Chem. Phys., Vol. 6, 474.

[68] C. G. B. Garrett, W. Kaiser, and W. L. Bond, 1961, Stimulated Emission into Optical Whispering Modes of Spheres, Physical Review, Vol. 124, No. 6, 1807.

[69] K.R. Hiremath and V.N. Astratov, 2008, Perturbations of Whispering Gallery Modes by Nanoparticles Embedded in Microcavities, Optics Express, Vol. 16, 5421.

[70] T. Wilk, S. C. Webster, A. Kuhn, G. Rempe, 2007, Single-Atom Single-Photon Quantum Interface, Science, Vol. 317, 488.

[71] Jeremy L. O'Brien, 2007, Optical Quantum Computing, Science, Vol. 318, 1567.

[72] D. L. Moehring, P. Maunz, S. Olmschenk, K. C. Younge, D. N. Matsukevich, L.-M. Duan, and C. Monroe, 2007, Entanglement of single-atom quantum bits at a distance, Nature, Vol. 449, 68.

[73] H. Miyazaki and Y. Jimba, 2000, Ab initio tight-binding description of morphology-dependent resonance in a bisphere, Physical Review B. Vol. 62, No. 12, 7976.

[74] N. W. Ashcroft and N. D. Mermin, 1976, Solid State Physics, Holt-Saunders International Editions, Philadelphia.

[75] C. M. Goringe, D. R. Bowler, and E. Hernández, 1997, Tight binding modeling of materials, Reports on Progress in Physics, Vol. 60, 1447.

[76] T. Mukaiyama, K. Takeda, H. Miyazaki, Y. Jimba, and M. Kuwata-Gonokami, 1999, Tight-Binding Photonic Molecule Modes of Resonant Bispheres, Physical Review Letters, Vol. 82, No. 23, 4623.

[77] Y. Hara, T. Mukaiyama, K. Takeda, and M. Kuwata-Gonokami, 2003, Photonic molecule lasing, Optics Letters, Vol. 28, No. 24, 2437.

[78] Y. Hara, T. Mukaiyama, K. Takeda, and M. Kuwata-Gonokami, 2005, Heavy Photon States in Photonic Chains of Resonantly Coupled Cavities with Supermonodispersive Microspheres, Physics Review Letters, Vol. 94, 203905.

[79] K. Totsuka, N. Kobayashi, and M. Tomita, 2007, Slow Light in Coupled-Resonator-Induced Transparency, Physics Review Letters, Vol. 98, 213904.

[80] Y. P. Rakovich, J. F. Donegan, M. Gerlach, A. L. Bradley, T. M. Connolly, J. J. Boland, N. Gaponik, and A. Rogach, 2004, Fine structure of coupled optical modes in photonic molecules, Physical Review A, Vol. 70, 051801(R)

[81] Y. P. Rakovich, M. Geriach, A. L. Bradley, J. F. Donegan, T. M. Connolly, J. J. Boland, M. A. Przyjalgowski, A. Ryder, N. Gaponik, A. L. Rogach, 2004, Confined optical modes in small photonic molecules with semiconductor nanocrystals, Journal of Applied Physics, Vol. 96, No. 11, 6761.

[82] Y. P. Rakovich, J. J. Boland, and J. F. Donegan, 2005, Tunable Photon lifetime in photonic molecules: a concept for delaying an optical signal, Optics Letters, Vol. 20, No. 20, 2775.

[83] J. F. Donegan, Y. P. Rakovich, M. Gerlach, T. Connolly, J. J. Boland, N. Gaponik, and A. L. Rogach, 2005, Photonic Molecules: A new Concept for Wavelength Tunable Optical Delay, ICTON 2005, Vol. 2, 116.

[84]   B. M. Möller, U. Woggon, M. V. Artemyev, and R. Wannemacher, 2004, Photonic molecules doped with semiconductor nanocrystals, Physical Review B, Vol. 70, 115323.

[85]   B. M. Möller and U. Woggon, 2005, Coupled-resonator optical waveguides doped with nanocrystals, Optics Letters, Vol. 30, No. 16, 2116.

[86]   B. M. Möller, U. Woggon, and M. V. Artemyev, 2006, Photons in coupled microsphere resonators, J. Opt. A: Pure Appl. Opt. Vol. 8, S113.

[87]   V. N. Astratov, J. P. Franchak, and S.P. Ashili, 2004, Optical Coupling and Transport Phenomena in Chains of Spherical Dielectric Microresonators with Size Disorder, Applied Physics Letters, Vol. 85, 5508.

[88]   A.V. Kanaev, V.N. Astratov, and W. Cai, 2006, Optical Coupling at a Distance Between Detuned Spherical Cavities, Applied Physics Letters, Vol. 88, 111111.

[89]   S.P. Ashili, V.N. Astratov, and E.C.H. Sykes, 2006, The Effects of Inter-Cavity Separation on Optical Coupling in Dielectric Bispheres, Optics Express, Vol. 14, 9460.

[90]   A.M. Kapitonov and V.N. Astratov, 2007, Observation of Nanojet-Induced Modes with Small Propagation Losses in Chains of Coupled Spherical Cavities, Optics Letters, Vol. 32, 409.

[91]   V.N. Astratov and S.P. Ashili, 2007, Percolation of Light through Whispering Gallery Modes in 3D Lattices of Coupled Microspheres, Optics Express, Vol. 15, 17351.

[92]   S. Yang and V. N. Astratov, 2008, Photonic Nanojet-Induced Modes in Chains of Size-Disordered Microspheres with an Attenuation of Only 0.08 dB per Sphere, Applied Physics Letters, Vol. 92, 261111.

[93]   Z. Chen, A. Taflove, and V. Backman, 2004, Photonic nanojet enhancement of backscattering of light by nanoparticles: a potential novel visible-light ultramicroscopy technique, Optics Express, Vol. 12, No. 7, 1214.

[94]   X. Li, Z. Chen, A. Taflove, and V. Backman, 2005, Optical analysis of nanoparticles via enhanced backscattering facilitated by 3-D photonic nanojets, Optics Express, Vol. 13, No. 2, 526.

[95]   Z. Chen, A. Taflove, and V. Backman, 2006, Highly efficient optical coupling and transport phenomena in chains of dielectric microspheres, Optics Letters, Vol. 31, No. 3, 389.

[96]   Z. Chen, A. Taflove, X. Li, and V. Backman, 2006, Superenhanced backscattering of light by nanoparticles, Optics Letters, Vol. 31, No. 2, 196.

[97]   A. Heifetz, J. J. Simpson, S. -C. Kong, A. Taflove, and V. Backman, 2007, Subdiffraction optical resolution of a gold nanosphere located within the nanojet of a Mie-resonant dielectric microsphere, Optics Express, Vol. 15, No. 25, 17334.

[98]   A. Daraei, A. Tahraoui, D. Sanvitto, J. A. Timpson, P. W. Fry, M. Hopkinson, P. S. S. Guimaraes, H. Vinck, D. M. Whittaker, M. S. Skolnick, and A. M. Fox, 2006, Control of polarized single quantum dot emission in high quality factor microcavity pillars, Applied Physics Letters, Vol. 88, 051113.

[99]   J. A. Timpson, S. Lam, D. Sanvitto, D. M. Whittaker, H. Vinck, A. Daraei, P. S. S. Guimaraes, M. S. Skolnick, A. M. Fox, C. Hu, Y-L. D. Ho, R. Gibson, J. G. Rarity, A. Tahraoui, M. Hopkinson, P. W. Fry, S. Pellegrini, K. J. Gordon, R. E. Warburton, G. S. Buller, 2007, Single photon sources based upon single quantum dots in semiconductor microcavity pillars, Journal of Modern Optics, Vol. 54, 453.

[100] S. Yang and V. N. Astratov, 2009, Spectroscopy of coherently coupled whispering gallery modes in supermonodispersive bispheres assembled on a substrate, Optics Letters, submitted on March 22, 2009.

[101] E. N. Ivanov, D. G. Blair, and V. I, Kalinichev, 1993, Approximate Approach to the Design of Shilded Dielectric Disk Resonators with Wispering-Gallery Modes, IEEE Transactions on Microwave Theory and Techniques, Vol. 41, No. 4, 632.

[102] Wladyslaw Zakovichz, 2005, Whispering-gallery-mode resonances: A new way to accelerate charged particles, Physics Review Letters, Vol. 95, 114801.

[103] R. K. Chang and A. J. Campillo, 1996, Optical process in Microcavities, ISBN-10: 9810223447.

[104] J. Donegan, R. A. Moore, Y. Rakovich, Y. Gun'ko, and T. S. Perova, 2007, Whispering-gallery modes in photonic tubes, SPIE Newsroom, Lasers & sources, 10.1117/2.120071.0585.

[105] M. K. Hin, A. Y. Chu, and S. -T. Ho, 1994, Estimation of the spontaneous emission factor for microdisk lasers via the approximation of whispering gallery modes, Journal of Applied Physics, Vol. 75(7), 3302.

[105] B. Möller, U. Woggon, M. V. Artemyev, and R. Wannemacher, 2003, Mode control by nanoengineering light emitters in spherical microcavities, Applied Physics Letters, Vol. 83, No. 13, 2696.

[106] S. Shiller and R. L. Byer, 1991, High-resolution spectroscopy of whispering gallery modes in large dielectric spheres, Optics Letters, Vol. 16, 130.

[107] V. S. Ilchenko, A. A. Savchenkov, A. B. Matsko, and L. Maleki, 2003, Dispersion compensation in whispering-gallery modes, J. Opt. Soc. Amer. A. Vol. 20, 157.

[108] Eugene Hecht, Optics, 3rd Edition, Addison Wesley, 1998.

[109] http://www.mrl.columbia.edu/ntm/level2/ch02/html/l2c02s07.html.

[110] S. -C. Kong, A. V. Sahakian, A. Heifetz, A. Taflove, and V. Backman, 2008, Robust detection of deeply subwavelength pits in simulated optical data-storage disks using photonic jets, Applied Physics Letters, Vol. 92, 211102.

[111] S. -C. Kong, A. Sahakian, A. Taflove, and V. Backman, 2008, Photonic nanojet-enabled optical data storage, Optics Express, Vol. 16, No. 18, 13713.

[112] C. E. Finlayson, P. J. Sazio, R. Sanchez-Martin, M. Bradley, T. A. Kelf, and J. J. Baumberg, 2006, Whispering gallery mode emission at telecommunications-window wavelengths using PbSe nanocrystals attached to photonic beads, Semiconductor Science and Technology, Vol. 21, L21.

[113] Z. P. Cai, H. Y, Xu, G. M. Stéphan, P. Féron, M. Mortier, 2004, Red-shift in Er:ZBLALiP whispering gallery mode laser, Optics communications, Vol. 229, 311.

[114] L. Maleki, A. B. Matsko, A. A. Savchenkov, and V. S. Ilchenko, 2004, Tunable delay line with interacting whispering-gallery-mode resonators, Optics Letters, Vol. 29, No. 6, 626.

[115] C. -Y. Chao, W. Fung, and L. J. Guo, 2006, Polymer Microring Resonators for biochemical sensing Applications, IEEE Journal of Selected Topics in Quantum electronics, Vol. 12, No. 1, 134.

[116] J. L. Nadeau, V. S. Ilchenko, D. Kossakovski, G. H. Bearman, and L. Maleki, 2002, High-Q whispering-gallery mode sensor in liquids, Proc. SPIE, Vol. 4629, 172.

[117] R. W. Boyd and J. E. Heebner, 2001, Sensitive disk resonator photonic biosensor, Applied Optics, Vol. 40, No. 31, 5742.

[118] I. Teraoka and S. Arnold, 2006, Enhancing the sensitivity of a whispering-gallery mode microsphere sensor by a high-refractive-index surface layer, J. Opt. Soc. Am. B, Vol. 23, No. 7, 1434.

[119] B. E. Little, S. T. Chu, H. A. Haus, J. S. Foresi, and J. -P. Laine, 1997, Microring resonator channel dropping filter, J. Lightwave Technol. Vol. 15, 998.

[120] B. E. Little, J. Foresi, H. A. Haus, E. P. Ippen, W. Greene, and S. T. Chu, 1998, Ultra-compact Si–SiO2 microring resonator channel dropping filter, IEEE Photon. Technol. Lett., Vol. 10, 549.

[121] A. Yariv, Y. Xu, R. K. Lee, and A. Scherer, 1999, Coupled-resonator optical waveguide: a proposal and analysis, Optics Letters, Vol. 24, No. 11, 711.

[122] Y. -Z. Huang, Y. -D. Yang, 2008, Mode Coupling and Vertical Radiation Loss for Whispering-Gallery Modes in 3-D Microcavities, J. of Lightwave Technol., Vol. 26, No. 11, 1411.

[123] M. Fujita, R. Ushigome, T. Baba, A. Matsutani, F. Koyama, and K. Iga, 2001, GaInAsP Microcylinder (Microdisk) Injection Laser with AlInAs(O_x) Claddings, Jpn. J. Appl. Phys., Vol. 40, 5338.

[124] P. Ferrand, J. Wenger, A. Devilez, M. Pianta, B. Stout, N. Bonod, E. Popov, and H. Rigneault, 2008, Direct imaging of photonic nanojets, Optics Express Vol. 16, 6930.

[125] T. Mitsui, Y. Wakayama, T. Onedera, Y. Takaya, and H. Oikawa, 2008, Light propagation within colloidal crystal wire fabricated by a dewetting process, Nano Letters, Vol. 8, 853.

[126] T. Mitsui, Y. Wakayama, T. Onodera, Y. Takaya, and H. Oikawa, 2008, Observation of light propagation across a 90^0 corner in chains of microspheres on a patterned substrate, Optics Letters, Vol. 33, 1189.

[127] J. Vučković, M. Pelton, A. Scherer, and Y. Yamamoto, 2002, Optimization of three-dimensional micropost microcavities for cavity quantum electrodynamics, Physical Review A. Vol. 66, 023808.

[128] L.-M. Duan, and H. J. Kimble, 2004, Scalable Photonic Quantum Computation through Cavity-Assisted Interactions, Physical Review Letters, Vol. 92, No. 12, 127902-1.

[129] Y.-F. Xiao, X.-M. Lin, J. Gao, Y. Yang, Z.-F. Han, and G.-C. Guo, 2004, Realizing quantum controlled phase flip through cavity QED, Physical Review A. Vol. 70, 042314.

[130] K. Iga, F. Koyama, and K. Kinoshita, 1988, Surface emitting semiconductor lasers, IEEE J. Quantum Electron, Vol. 24, 1845.

[131] J. L. Jewell, A. Scherer, S. L. McCall, Y. H. Lee, S. Walker, J. P. Harbison, and L. T. Florez, 1989, Low-threshold electrically pumped vertical-cavity surface-emitting microlasers, Electron. Lett., Vol. 25, 1123.

[132] E. Kuramochi, M. Notomi, S. Mitsugi, A. Shinya, and T. Tanabe, 2006, Ultrahigh-Q photonic crystal nanocavities realized by the local width modulation of a line defect, Applied Physics Letters, Vol. 88, 041112.

[133] V.N. Astratov, S. Yang, S. Lam, B.D. Jones, D. Sanvitto, D.M. Whittaker, A.M. Fox, and M.S. Skolnick, A. Tahraoui, P.W. Fry, and M. Hopkinson, 2007, High-Quality-Factor WG modes in Semiconductor Microcavity Pillars with Circular and Elliptical Cross Section, IEEE Proc. of Int. Conf. on Transparent Opt. Networks – ICTON07, Special Section on Microresonators and Photonic Molecules: Trapping, Harnessing and Releasing Light, Vol. 4, 170-172, Rome, Italy, July 1-5.

[134] V.N. Astratov, S. Yang, S. Lam, D. Sanvitto, A. Tahraoui, D.M. Whittaker, A.M. Fox, and M.S. Skolnick, 2007, Observation of Whispering Gallery Resonances in circular and Elliptical Semiconductor Pillar Microcavities, Proc. of Progress in Electromagnetics Research Symposium, Beijing, China, March 26-30.

[135] *FullWave*TM, Rsoft Design Group Inc., U.R.L.:www.rsoftdesign.com.

[136] K. Yee, 1966, Numerical solutions of initial boundary value problems involving Maxwell's equations in isotropic media, IEEE Transactions on Antennas and Propagation, Vol. AP-14, 302-307.

[137] http://www.martinos.org/~adunn/papers/dissertation/node37.html.

[138] Y. -R. Nowicki-Bringuier, J. Claudon, C. B̈ockler, S. Reitzenstein, M. Kamp, A. Morand, A. Forchel, and J. M. G´erard, 2007, High Q whispering gallery modes in GaAs/AlAs pillar microcavities, Optics Express, Vol. 15, No. 25, 17291.

[139] K. Srinivasan, M. Borselli, O. Painter, A. Stintz, and S. Krishna, 2006, Cavity Q, mode volume, and lasing threshold in small diameter AlGaAs microdisks with embedded quantum dots, Optics Express, Vol. 14, No. 3, 1096.

[140] S. Reitzenstein, C. Hofmann, A. Gorbunov, M. Strauß, S. H. Kwon, C. Schneider, A. Löffler, S. Höfling, M. Kamp, and A. Forchel, 2007, AlAs/GaAs micropillar cavities with quality factors exceeding 150,000, Applied Physics Letters, Vol. 90, 2521109.

[141] N. Stefanou and A. Modinos, 1998, Impurity bands in photonics insulators, Physics Review B, Vol. 57, 12127.

[142] L. I. Deych, C. Schmidt, A. Chipouline, T. Pertsch, and A. Tünnermann, 2008, Optical coupling of fundamental whispering-gallery modes in bispheres, Physics Review A, Vol. 77, 051801.

[143] Kirk A. Fuller, 1991, Optical resonances and two-sphere systems, Applied Optics, Vol. 30, No. 33, 4716.

[144] A. Armitage, M. S. Skolnick, A. V. Kavokin, D. M. Whittaker, V. N. Astratov, G. A. Gehring, J. S. Roberts, 1998, Polariton-induced optical asymmetry in semiconductor microcavities, Physics Review B, Vol. 58, Issues 23, 15367.

[145] M. Bayer, T. Gutbrod, J. P. Reithmaier, A. Forchel, T. L. Reinecke, P. A. Knipp, A. A. Dremin, and V. D. Kulakovskii, 1998, Optical modes in photonic molecules, Physics Review Letters, Vol. 81, Issues 12, 2582.

[146] J. F. Donegan, Y. P. Rakovich, M. Gerlach, T. Connolly, J. J. Boland, N. Gaponik, and A. L. Rogach, 2005, Photonic molecules: a new concept for wavelength tunable optical delay, Proceedings of 2005 7th International Conference, Vol. 2, Issue 3, 7116.

[147] I. M. White, N. M. Hanumegowda, H. Oveys, and X. Fan, 2005, Tuning whispering gallery modes in optical microspheres with chemical etching, Optics Express, Vol. 13, No. 26, 10754.

[148] S. Vyawahare, K. M. Craig, and A. Scherer, 2006, Patterning Lines by Capillary Flows, Nano Letters, Vol. 6, No. 2, 271.

[149] Roper Scientific, WinSpec/32 for windows.

[150] Frank L. Pedrotti, S. J. Leno S. Pedrotti, Introduction to optics, 2nd edition, Prentice Hall (1993)

[151] J. Ng, and C. T. Chan, 2008, Size-selective optical forces for microspheres using evanescent wave excitation of whispering gallery modes, Applied Physics Letters, Vol. 92, 251109.

[152] D. A. Fletcher, K. E. Goodson, and G. S. Kino, 2001, Focusing in microlenses close to a wavelength in diameter, Optics Letters, Vol. 26, 399.